Modelling and experimental investigation of eddy current distribution for angular defect characterisation

Ilham Mukriz Zainal Abidin

A thesis submitted for the degree of Doctor of Philosophy

School of Electrical, Electronic and Computer Engineering
Newcastle University

May 2010

Contents

List of figures

List of tables

Acknowledgement

I would like to express my gratitude to a number of people who have helped me during the past years of PhD study. Firstly, special thanks to Prof. Gui Yun Tian, for supervising the work, and providing regular help and guidance on the project. To my mentor, Dr. Ab Razak Hamzah, whose encouragement and advice has provided me guidance in the research field.

I would like to thank my colleagues, Dr John Wilson, Dr. Yong Li, and Mr. Anthony Simm and all in the Sensor Technology Research Group at Newcastle University, who have provided valuable discussion and advice.

Special appreciation to Malaysian Nuclear Agency for giving me the opportunity to undertake the research project which have matured and equipped me for years to come.

My deepest thanks go to my parents, for always supporting and encouraging me during my education. It is to them that I dedicate this thesis.

Lastly, I offer my regards and blessing to all those who supported me in any respect during the completion of the study.

Summary

Current industrial requirements for nondestructive testing demand defect quantification rather than simple defect detection. This is not a simple task as defects in components, such as cracks, rarely have a simple geometrical shape. Therefore, the influence of defect shape and orientation and its effect on the inspection results needs to be addressed to avoid misinterpretation of the response signals and for a quantitative characterisation of defects. Finite element method (FEM) numerical simulations for eddy current non-destructive evaluation (ECNDE) can provide information on how the induced eddy current interacts with defects and the effect of defect shape and geometry towards the results. Through the analysis of the simulation results, links can be established between the measurements and information relating to the defect, such as 3-D shape, size and location, which facilitates not only forward problem but also inverse modelling involving experimental system specification and configuration; and pattern recognition for 3-D defect information.

This work provides a study of the characterisation of angular defects through the technique of visualisation and mapping of magnetic field distribution for pulsed eddy current (PEC) and temperature distribution for PEC thermography. 3-D FEM simulations are utilised to provide the guidelines for experimental designs and specifications; understanding of the underlying physics surrounding a particular defect; and means for features extraction from the acquired responses. Through the study, defect Quantitative Non-destructive Evaluation (QNDE) has been established using the features extracted from the mapping by taking into consideration the angular characteristic of defect in the inspection results. Experimental investigations are then performed to verify the simulation results and the feasibility of the proposed techniques and extracted features to be used in acquiring information about the angular defect.

The work concludes that the technique of mapping the resultant distribution from the interaction of eddy currents and defects has provided the vital information needed for defect characterisation. Features extracted from the mapping via numerical investigations have provided the means for the QNDE of angular defects. The work shows that the technique and features introduced has provided an alternative way for defect characterisation and QNDE, which also can be extended its application to other industrial components and research field.

Abbreviations

ACFM : Alternating current field measurement
AE : Acoustic emission
EC : Eddy current
ECNDE: Eddy current non-destructive evaluation
EFG : Element free galerkin
EMAT: Electromagnetic acoustic transducer
ENDE : Electromagnetic NDE
ET : Eddy current testing
FBEM : Finite boundary element method
FDM : Finite difference method
FEM : Finite element method
IR : Infrared
LT : Lock-in thermography
MAE : Magnetic acoustic emission
MBE : Magnetic barkhausen noise
MEMS: Micro-electromechanical system
MFL : Magnetic flux leakage
MPI : Magnetic particle inspection
NDE : Nondestructive evaluation
PDE : Partial differential equation
PEC : Pulsed eddy current
PIG : Pipeline inspection gauge
PMFL : Pulsed magnetic flux leakage
PMR : Pulsed magnetic reluctance
QNDE : Quantitative nondestructive evaluation
RCF : Rolling contact fatigue

RT	:	Radiography technique
SL	:	Slope
SPH	:	Smoothed particle hydrodynamics
$T_{\max}$	:	Maximum temperature amplitude
TBC	:	Thermal barrier coating
TMS	:	Transcranial magnetic stimulation
UT	:	Ultrasonic technique
VI	:	Visual inspection

Chapter 1

Introduction

1.1 Research background

Amongst all of the available methods of non-destructive evaluation (NDE), electromagnetic NDE methods are often the most suitable for the inspection of metallic structures or components, in engineering applications within the petrochemical, aerospace, nuclear, transportation and energy industries. A number of techniques have been developed, including eddy current (EC), pulsed eddy current (PEC), magnetic flux leakage (MFL) and ground penetrating radar (GPR), which are based on electromagnetism and the interaction of electromagnetic fields with conductive specimens under inspection. Electromagnetic non-destructive evaluation (ENDE) techniques are sensitive to various magnetic, structural and stress properties of conductive materials. These lead to diverse applications of ENDE, such as defect detection, proximity measurement, thickness measurement, conductivity measurement, material sorting and they can even provide information about material properties.

To meet the current requirements of industry, one of the recent trends of NDE is to provide quantitative as well as qualitative assessments of materials. This quantitative assessment is known as quantitative non-destructive evaluation (QNDE). Quantification of the size and length of the defect inside the investigated sample has to be addressed as accurately as possible for component lifetime prediction and the overall assessment of the structure. However, since realistic defects tend to have complex geometries (e.g. a crack grows at an angle to the surface), the influence of defect angular characteristics on the inspection results posed a major problem for such quantification. Much attention has been given to developing techniques and inspection systems which could give the best possible inspection sensitivity and efficiency for QNDE of defects, but little attention has been given to the study of how the defect shape and orientation affected the inspection results. The study of how angular defects interact with eddy currents would assist the task of achieving more accurate quantification of defects. Together with the help of numerical simulations and experimental investigation, misinterpretation of the inspection results due to the geometrical influence of defects could be minimised and this would benefit the related industries and the NDE research communities by providing better explanations of the results from QNDE assessment of defects.

QNDE of defects is vital when inspecting critical components and assemblies. Therefore, all aspects of the defect geometries that influence the inspection outputs need to be taken into consideration in doing the quantitative assessment. Numerical studies have helped in the research of eddy current techniques for defect characterisation, by predicting the results with high accuracy, at a level comparable with experimental results [1, 2]. It also provides an understanding of the underlying phenomena regarding eddy current interaction with defects through the analysis of the results. 3-D numerical modelling is particularly valuable since the interaction between applied fields and induced currents with complicated sample and defect geometries cannot be described by closed-form equations of analytical modelling, nor can they be approximated by 2-D geometries [3, 4]. In addition, some situations of test geometries that are difficult, expensive or impossible to simulate experimentally have made numerical modelling the only practical way to provide defect characterisation parameters in eddy current testing [1].

This work provides a study of the characterisation of angular types of defect, using visualisation techniques and mapping of the resulting distribution from the interaction of eddy currents and defects. 3-D Finite Element Method (FEM) numerical simulations are performed in order to:

a) provide the means for feature extraction from the acquired distribution responses for QNDE of the investigated defect

b) help in understanding the underlying phenomena surrounding a particular defect, and

c) provide guidelines for experimental designs and specifications.

Through the work, geometrical information of defects can be obtained by taking into consideration the angular characteristics of the defects before measurements of length/depth are made. Using the features extracted from the distribution mapping by numerical simulations, geometrical information regarding the angle of the defects which predominantly affect the results can be obtained, and consequently the length/depth of the defect inside the investigated sample can be quantified.

The research fulfils: (1) 3D FEM for NDE forward problems involving ECNDE and integrative technique i.e. PEC and PEC thermography, through which the resulting responses distribution from the interaction of eddy currents and defects are visualised and mapped for defect characterisation; (2) Investigation of the angular characteristic of defects and their influence on the inspection results for a QNDE approach, to avoid misinterpretation and false evaluation of the responses signal; (3) Extraction of features to determine and quantify the angle of defects from the mapped distribution for QNDE of defects; (4) Experimental investigation to verify the results from the numerical simulation and the feasibility of the techniques and extracted features; and provide the link between theoretical and experimental study in NDT&E for better understanding and explanation of physical phenomena arising from practical, experimental results.

1.2 Aims and Objectives

1.2.1 Research aims

The aim of the research is apparent to provide QNDE of defects by taking into consideration the defect shape and orientation using visualisation and mapping techniques of the resultant distribution responses of eddy current and defect interaction. Angular defects are to be investigated through numerical simulation studies, conducted prior to the experiments, to provide predicted responses from defects using techniques related to ECNDE. Based on these numerical studies, features are to be identified and extracted from the mapping with the intention of quantifying the angle of a given defect and subsequently its length/depth inside the sample. Based on the predicted responses, a suitable ECNDE technique to perform the visualisation and mapping task is to be proposed and realised. These features and the proposed technique are then implemented on real defects via experimental study, to verify its effectiveness for QNDE of defects within in-service samples. This will provide the link between theoretical and experimental study in achieving better QNDE of defects.

This research project has been funded by the Government of Malaysia as a three and half year's studentship funding in the area of state-of-the-art eddy current NDE. Through this studentship, it is expected that this work will contribute to in-depth knowledge and expertise in the field of NDT & E, which will benefit the country and related industries. The work covered in the research project also form parts of projects supported by EPSRC for ‘Bridging the gap of theoretical and experimental eddy current NDT’ (EP/E010485) and ‘Pulsed eddy current stimulated thermography NDE’ (EP/F023324). International research networking has also been established in the form of collaboration work in studying PEC technique capabilities for defect characterisation with Dr Catalin Mandache from the National Research Council of Canada, funded by the Royal Society of UK.

1.2.2 Research objectives

The objectives of the research are summarised as follows:

- To undertake a comprehensive literature survey on defect detection and characterisation using NDE techniques.

- To conduct 3-D FEM numerical simulations concerning the visualisation and mapping of the resulting distribution responses from eddy current and angular defects interaction for the QNDE of defects.

- To use features acquired from this simulation work when acquiring quantitative measurements of angular defects from the mapped resultant distribution in providing QNDE of defects.

- To demonstrate QNDE for defect quantification by taking into considerations the angular characteristic of defects in the inspection results, to avoid misinterpretation of the inspection signal.

- To gain an understanding of the underlying phenomena of eddy current interaction with defects that leads to the resultant distribution responses, thus providing better explanations of the inspection results.
- To verify the simulation results, the feasibility of the technique and extracted features when performing the mapping task and QNDE of angular defects via experimental investigation.

1.3 Achievements

The main achievements of the research are as follows:

- A thorough review of NDT&E techniques for defect detection and characterisation has been undertaken and the potential for an integrated technique based on EM and thermal phenomena has been assessed and reported.
- 3-D FEM simulations investigations on angular defects performed prior to the experiments have provided the expected response from defects using the PEC and PEC thermography technique. It has been found that the simulations can provide :

  a) an understanding of the underlying phenomena which gives the resultant eddy current distribution from defect interaction

  b) the means for feature extraction from the acquired distribution responses for future QNDE of the investigated defect

  c) guidelines for experimental designs and specification which can be used to assess the practicality of the proposed techniques through the analysis of the simulation results.

  The simulations can thus provide the basis for further work in the field of NDE for defect detection and characterisation.

- The technique of visualisation and mapping of eddy current distribution from defect interaction has been assessed. It has been found that geometrical information of angular defects can be obtained through the features indentified from the mapping. While PEC has limitations for practical implementation, PEC thermography has been successful in providing an alternative way of mapping the eddy current distribution via the IR camera. It has been shown that quantitative information of angular defects can be obtained through the features extracted from the temperature distribution by PEC thermography. The proposed technique can thus provide a fast and effective solution for defect detection and characterisation over a relatively wide area.

- The extracted features for PEC thermography acquired from the simulation studies have shown its capacity to provide geometrical information of angular defects such as their angle, length and depth. The slope, SL feature from the temperature distribution can be used to obtain the angle information and the maximum amplitude feature, $T_{\max}$ can be used to obtain the length and depth information of the angular defects. The temperature profiles from the temperature mapping of the angular defects were examined and by using the aforementioned features, quantitative information of angular defects was obtained. Experimental verification has shown that the extracted features can be used for QNDE of angular defects. These features can be used in real QNDE inspections of critical components and assemblies, which usually have complex geometries.
- Publication of papers in journals (NDT&E International and Insight) and presentation of work to conferences (BINDT and WCNDT), as listed in the list of publication section of this thesis.

1.4 Thesis layout

Chapter 1 gives an outline of the research background, the aims and objectives of the project, and the main achievements of the research.

Chapter 2 begins with reviews on NDE in general and a brief description of the most common NDE techniques used in industry for defect detection and characterisation. A section on the state-of-the-art in eddy current NDE then discusses the recent trends in ECNDE for defect characterisation. Following the discussion, an overview is given on the direction and capabilities of the approach employed in the current research, in providing solutions to improve defect capabilities and QNDE related to ECNDE. The summary of the literature review is provided at the end of the chapter, with a discussion on problems identified to be the focus of this study.

Chapter 3 presents the theoretical background of ECNDE, which starts with a brief introduction to Maxwell's equations, followed by a general overview of the governing equations for EM and thermal phenomena in ECNDE. Highlights of FEM numerical simulation in solving complicated problems are discussed, along with its advantages over analytical methods with respect to defects having complicated shapes. Furthermore, the research methodology for the thesis is presented in this chapter, which outlines the simulation and modelling approach taken in solving the forward problems and its application towards experimental designs for comprehensive defect assessment.

Chapter 4 details the defect characterisation investigation via the PEC technique, which involves numerical and experimental studies. Firstly, the pulse width variation of the PEC technique is described, along with the strength and limitations of the PEC technique. The study starts with different pulse widths and frequency components in PEC as a method of defect depth discrimination with direct applications in multilayered structures. The investigation of PEC testing for angular defects is then performed through the mapping of magnetic field distributions implemented via time-stepping 3-D FEM, with features from the mapping extracted for angular defects' characterisation. A discussion of the limitations of the implementation of the PEC technique for defect characterisation based on the study undertaken is presented at the end of the chapter.

Chapter 5 presents the numerical and experimental studies applied to understand PEC thermography on simple types of defects; a slot and a notch, which includes eddy current distribution and heating propagation to aid in the development of feature extraction and a pattern recognition technique for the quantitative analysis of eddy current thermography images and defect characterisation. 3-D multiphysics FEM is employed to simulate the eddy current distribution and the resultant temperature behaviour, in order to fully understand the heating mechanism surrounding a particular defect. Using the numerical investigations as guidelines, experimental designs were constructed and a comparative study was performed for verification.

Chapter 6 focuses on the capabilities of PEC thermography in obtaining quantitative information for angular defect characterisation through the analysis of the surface thermal distribution. The investigation is implemented by simulating the transient thermal distribution for angular defects, via 3-D multiphysics FEM, with experimental work undertaken for verification. The influence of the defect geometries and orientation on the thermographic distribution, and the parameters which affect the temperature distribution, were analysed and presented through extracted features acquired from the 3-D simulation results for the QNDE of the angular defects.

Chapter 7 presents experimental investigations of angular defects in rail heads via the PEC thermography technique. The effectiveness of PEC thermography when mapping multiple defects simultaneously is tested on real defects in industrial components to conclude the investigation of eddy current distribution for angular defect characterisation through the visualisation and mapping technique.

Chapter 8 summarises the research work so far, with conclusions of the findings. An outline of the scientific contributions to NDT&E is given, followed by some suggestions on future work based on the current investigation.

1.5 Chapter summary

This chapter presents an introduction to the research work which has been conducted on the characterisation of angular defects using visualisation and mapping techniques for defect QNDE. The recent demands and current needs in industry for QNDE are given as the background to ongoing study, which is followed by the aims and objectives of this research. The contributions of the current work are presented. Following that, the layout of this thesis and all chapter contents are summarised.

Chapter 2

Literature Survey

This chapter comprises a literature survey of state-of-the-art ECNDE for defect characterisation and QNDE. The chapter is divided into two main sections. The first section covers a brief description of the most common NDE techniques used in industry, together with details of typical applications, advantages and limitations of the techniques. The second section will focus on a review of state-of-the-art ECNDE for defect detection and characterisation. Reviews and discussions of current research and industrial problems, covering modelling approaches in ECNDE, eddy current imaging and integrative NDE techniques are provided, and ways to improve techniques and provide alternative solutions for defect detection and characterisation are discussed. The problems that need to be addressed within the current research with regard to ECNDE are identified at the end of the chapter, outlining the need for the investigation of angular defects for QNDE.

2.1 Nondestructive testing and evaluation

Nondestructive inspection techniques are employed to examine an object, material or component without impairing its future usefulness. Since the techniques do not alter the article being inspected, they are valuable methods for material and component evaluation, troubleshooting and research that can save both money and time. A prominent application of NDE is to detect and characterise defects in order to assess the structural integrity of materials and components and it is employed in all types of engineering industries, especially in the transportation [5]; aerospace [6]; manufacturing [7]; petrochemical; [8] and defence industries [9]. The following will provide a brief description of the most commonly used NDE techniques in industry, including visual inspection (VI), radiography technique (RT), ultrasonic technique (UT), magnetic flux leakage (MFL), thermography and eddy current technique (ET). However, these are by no means all of the techniques available to NDE. Acoustic emission (AE), alternating current field measurement (ACFM) and spectrography have been used to provide information that the above techniques have been unable to yield, and development of new methods and techniques continues.

2.1.1 Visual inspection (VI)

The most basic NDE technique is visual inspection. The technique follows a procedure in which the inspector looks for surface imperfections that are indicative of defective parts or components. Liquid penetrant testing is a widely used form of visual inspection, where the component under inspection is coated with a solution that contains a visible or fluorescent dye [10]. Excess solution is then removed from the surface of the object but leaving it in surface-breaking defects. A developer is applied to the surface to draw the penetrant out, giving a visual indication of surface flaws. Liquid penetrant testing is applicable to almost any type of non-porous material but it is limited to surface-breaking defects with the requirement of surface preparation. Additionally, the technique is not applicable for automated systems and is unable to provide quantitative information.

Magnetic particle inspection (MPI) [11] is a visual inspection technique which can be used to detect surface and near-surface defects in ferromagnetic components and structures. Figure 2.1 illustrates the principle of MPI for defect detection. It is accomplished by inducing a magnetic field to flow in the material using permanent magnets or electromagnets. The presence of discontinuities such as surface or near-surface defects cause the induced magnetic field to leak out of the material into the air. By applying the surface with magnetic particles (either dry or suspended in liquid), the indication of the defect is made visible as the particles are attracted to the areas of the leaked magnetic flux. Major advantages of MPI come from its simplicity, economy, sensitivity and accuracy [12].

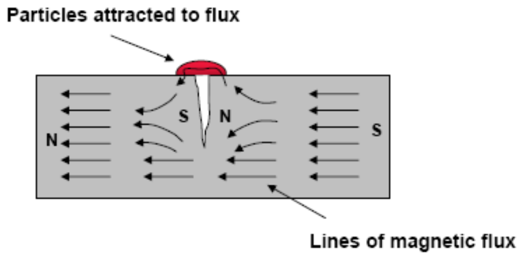

Figure 2.1: The leakage of magnetic flux caused by the presence of a defect in MPI inspection [13]

Although MPI provides a quick and easy technique for the inspection of ferromagnetic structures and is commonly used in applications such as the inspection of aircraft engine components [10], there are several drawbacks to the use of MPI, such as the insensitivity to defects that are oriented parallel to the applied field, the need for surface preparation and its inability to provide quantifiable data. FEM has been used to improve the analysis of MPI experimental data and ultimately for the improvements in MPI experimental design [12]. The optimum condition for detection of different sizes and complicated geometries of defects in materials also has been determined for MPI with the use of FEM [14].

2.1.2 Radiography technique (RT)

The basic principle of radiography is the attenuation of penetrating radiation in materials as a function of radiation energy, material density and material thickness. Due to the different attenuation coefficients of various materials and dependence of attenuation on the material thickness, defects in the test specimen cause variations in the transmitted radiation intensity [15]. The transmitted radiation beam is then recorded by some means (film or digital detectors) which forms a radiographic image [16-17] as shown in Figure 2.2 [18]. As may be seen in the figure, the presence of defects will be shown by the variants of black and white contrast on the exposed radiographic film. By evaluating the images, defects located inside the sample and geometrical conditions of the sample; such as thickness variations, can be detected.

Traditional sources of penetrating radiation are X-ray generators (tubes) and radioactive isotopes (industrial sources of gamma-rays are Ir-192, Co-50 or Se-75). Each source has its own characteristics and therefore has certain advantages in specific applications. The selection of the particular energy range of radiation to be used is one of the major factors responsible for penetrating ability and contrast [19-20].

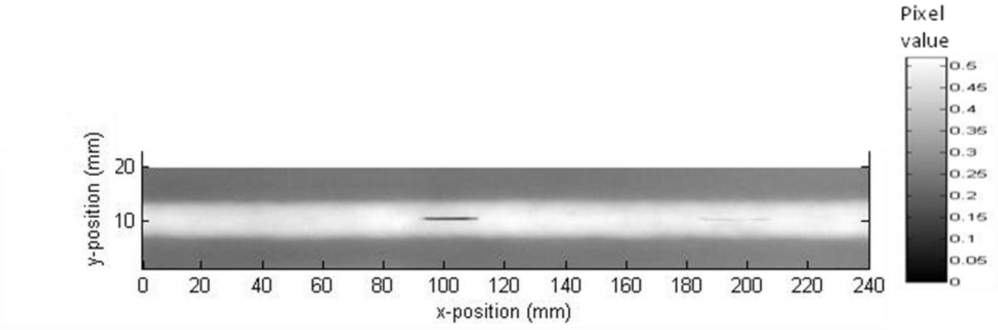

Figure 2.2: Example of radiographic image which shows indication of defects in a welded sample [18]

Computed tomography involves the reconstruction of the radiographic projection done at many different angles around the inspected sample. Its application results in a cross-sectional image of the sample. The data obtained from the radiographic projections are then reconstructed mathematically to produce the desired image [21]. Due to the absence of structural noise from detail outside the thin plane of inspection, images are much easier to interpret than conventional radiographic film. A number of slices through the sample can be reconstructed to provide a 3-D view of internal and external structural details. Through high resolution 3-D imaging by computed tomography, information about inspected structures, geometry and defects can be obtained by subsequent analysis and manipulation of the acquired 3-D images [22].

Even though RT is one of the most commonly used techniques for weld inspection, the reliability of detection of defects using this technique relies on the capability of an operator in interpreting the radiographic images. An incorrect evaluation may reject a piece in good condition, or accept a piece with defects exceeding the limit established by the applicable standards [20]. Apart from possible health hazards, there are several notable reasons which limit the use of RT for QNDE; it is not suitable for surface defects and it is not possible to extract quantitative information for defect depth estimation.

2.1.3 Ultrasonic technique (UT)

The ultrasonic technique (UT) has received a lot of attention in recent years in both industry and academia. In ultrasonic testing, piezoelectric transducers are usually used to transmit ultrasonic pulses into the material under test. The transmitted pulses are reflected by voids in the material due to discontinuities such as cracking or material boundaries such as inclusions as shown in Figure 2.3. Reflections transmitted and received by the same transducer are analysed using a computer based system to distinguish between reflections from the material edges and sides and reflections from flaws.

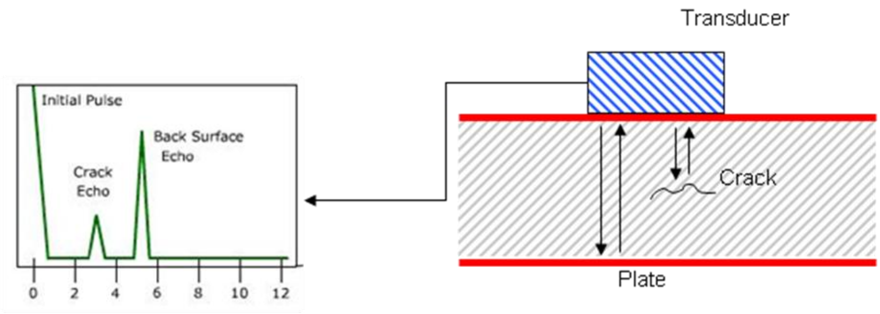

Figure 2.3: Ultrasonic testing (UT)

Although UT systems have the capability to detect defects throughout the bulk of the material, they suffer from a difficulty to distinguish between reflections from surface and near-surface flaws, and reflections from material surfaces. Another disadvantage of UT is the need to use a coupling medium such as water or gel to acoustically couple the pulses from the transducer to the material. This makes UT unsuitable in certain situations due to surface preparation requirements. Much work has been done in recent years to develop non-contact ultrasonic techniques with the defect characterisation and bulk inspection capabilities of UT, but without the surface preparation requirements. Air-coupled techniques include adaptations of traditional piezoelectric transducers [24] and systems using pulsed laser transmitters and air-coupled capacitive receivers [25]. Electromagnetic acoustic transducers (EMATs) have also been developed to generate and receive signals, although this does mean that EMATs are limited to electrically conductive materials [26, 27].

Developments in ultrasonic QNDE require simulation tools for cost effective research and engineering work [28]. FEM has been widely used as a tool in the design of ultrasonic transducers in the build-up of ultrasonic technology to cater the needs of the industry [29, 30]. This is also driven by the need for quantitative results in ultrasonic NDE which requires the development of models to predict the inspection outcome of actual experimental configurations [28].

2.1.4 Magnetic flux leakage (MFL)

Magnetic flux leakage (MFL) is a derivative of MPI which is based on the detection of leakage of magnetic flux at the sample surface due to the presence of defects. In practice, magnetisation is provided by a permanent magnet or an electromagnet powered by dc, ac or pulsed excitation. The difference between MPI and MFL is that MFL measures the flux leakage using a pickup coil or magnetic field sensors, e.g. Hall devices or magnetoresistive sensors, as shown in Figure 2.4, thus allowing computer-based data acquisition, signal processing and quantitative assessment of test results. In the case of dc magnetic fields, the variation of flux density can be detected by the induction coils by the movement of the coil in static field. An eddy current is induced within the sample when the MFL induction coil has relative speed to the sample, even though the excitation current is dc [31]. The influence of eddy currents in the sample on MFL signals involves not only the shape but also the magnitude of the signals measured. Thus, induction coils are not suitable when inspection speed varies, since the distribution of magnetic fields will be influenced by eddy currents due to the movement of the coil. The signal amplitude also decreases with decreasing speed and below a certain flux change rate, the signal disappears into noise [32].

MFL is used in various applications; including inspection of storage tanks, tube thread inspection and steel plate samples [32, 33], but the most common use is in the inspection of oil and gas pipelines [34, 35], where around 90% of pipeline inspection gauges (PIGs) use MFL technology [36]. Many modern systems use the so-called intelligent PIG, where permanent magnets are used to magnetise the pipeline wall and an array of Hall-effect sensors or induction coils are used to measure the leakage field around pipeline flaws. When the level of flux leakage rises above a predetermined threshold, on-board data acquisition and storage is triggered for offline analysis of data from flawed areas after the test is completed [37].

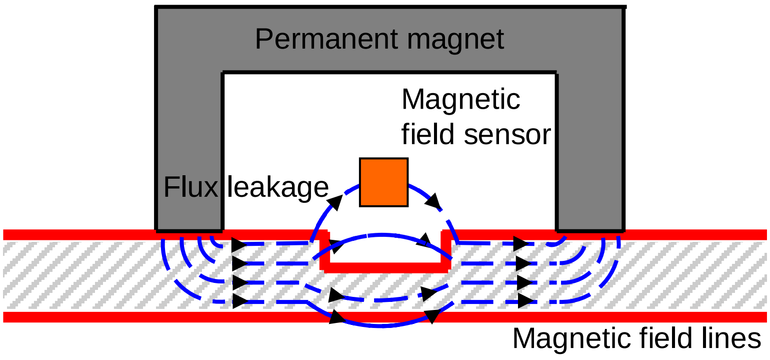

Figure 2.4: Magnetic flux leakage (MFL) inspection

The measured flux leakage signal in MFL systems reflects both geometrical discontinuities and stresses [38], but the degree to which stresses influence the measured signal is governed by the field intensity in the sample under inspection. Ferromagnetic materials have variable permeability, so if a field is induced which is well below saturation, the permeability is relatively high and the measured signal is heavily influenced by any stresses acting on that material. Conversely, if the induced field drives the material into saturation, the influence of stress is diminished and the influence of geometrical discontinuities is dominant. Notable limitations of this technique are its poor quantitative potential and its inability to distinguish between same side and opposite side defects.

Theoretical approaches have been utilised in an effort to improve and analyse the capabilities of the MFL technique. FEM is preferable in solving the equations governing electromagnetic fields in MFL systems [32, 35], since the analytical approach to modelling MFL is difficult to achieve due to the awkward boundaries associated with realistic defect shapes [35]. QNDE for the reconstruction of 3D defect shapes has also been realised with the analysis of MFL signals due to cracks of different shapes, calculated by FEM hybrid code which employed method and polarisation algorithms [39].

2.1.5 Thermography

Improvements in infrared (IR) camera technology have allowed thermography to develop from a qualitative overall inspection technique which needs to be supplemented by NDE techniques to a stand-alone technique able to supply quantitative information through the acquisition and analysis of image sequences. These technological innovations, paired with the development of advanced signal analysis techniques, have led to the emergence of thermographic defect detection as a viable industrial inspection tool which has found acceptance in many areas, including the safety inspection of critical aerospace structures [40]. The major advantage of thermographic inspection over other NDE techniques is that it is able to inspect a relatively wide area in a short time. Test results can then be immediately accessed to provide an indication of any major faults and the data sequences further analysed to provide quantitative information. The technique is also applicable to a wide range of materials, though selection of the optimal excitation parameters for the chosen application is important [41].

Thermographic NDE can be divided into two categories, the passive and active approaches. The passive approach tests materials and structures which are naturally at different (often higher) temperatures than the ambient background, while in the case of active thermography, an external heating stimulus is used to induce relevant thermal contrast as shown in Figure 2.5. The active approach to thermography has numerous applications in NDE. Moreover, since the characteristics of the required external stimulus are known, i.e. heating time applied to the sample, quantitative characterisation becomes possible. Two categories of heating technique are applicable to NDE defect detection: those that deposit heat on the material surface and then rely on the heat to propagate through the material to detect subsurface defects, and those that excite the material itself and have some direct interaction with subsurface defects.

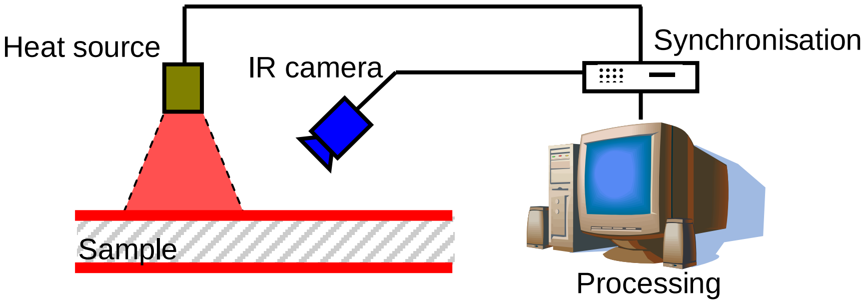

Figure 2.5: Experimental setup for active thermography

Traditional thermographic inspection utilises direct deposition of heat on the material surface using heat lamps [42, 43]. Despite the popularity of the technique, the utilisation of this type of heating for thermography does have a number of potential disadvantages; the reflected heat from the material under inspection can interfere with the measured signal, causing SNR problems, and it can be difficult to deposit a sufficient amount of heat on the material surface in the short time needed for pulsed thermography.

Heating of the material under inspection can also be accomplished via the application of sonic or ultrasonic energy using a device such as an ultrasonic welding horn; this is known as vibrothermography, thermosonics or sonic IR [44]. The applied excitation vibrates the material under inspection and leads the crack faces to rub against each other, the mechanical energy is converted to heat and the generated heat is detected at the material surface. Disadvantages include the need for contact between the test piece and the ultrasonic welding horn and the unreliability of this contact, which leads to the vibration spectrum produced being highly variable from contact to contact [44].

An alternative to heat lamp or sonic excitation is found in eddy current (EC) heating, where the part under inspection is heated by an inductively-generated current flow [45-48]. The induced eddy currents are converted to heat through ohmic heating, according to Joule’s law. Both direct heating and diffused heating contribute to defect detection; defects such as cracks, voids or delaminations which are within the range of the eddy current distribution disturb the current flow and thus change the temperature distribution. Defects which do not directly interact with the induced eddy currents may interact with the heat generated at the surface as it propagates through the material (as with traditional heat lamp techniques). Thus, eddy current thermography has many potential advantages over heat lamp and sonic excitation techniques; there is no interference from applied heating or excitation equipment (the change in temperature of the coil itself is very small), there is little chance of damage to the material under inspection, as heating is limited to a few °C and for near-surface defects, direct interaction with eddy currents can improve detectability [49].

Eddy current thermography involves the application of a high frequency (typically 50 kHz – 500 kHz) electromagnetic wave to the material under inspection. For pulsed thermography [46-48] this is simply switched on for a short period (typically 20ms – 2s), in contrast to lock-in techniques [45], where the amplitude of the high frequency wave is modulated by a low frequency lock-in signal.

2.1.6 Eddy current (EC) technique

The eddy current (EC) technique has been shown to be one of the most effective techniques for the detection and characterisation of surface defects in conductive samples. This technique is based on inducing electric currents in the material being inspected and observing the interaction between those currents and the material. The induced eddy currents are basically a circulating current generated by electromagnetic coils in the test probe, and monitored simultaneously by measuring the electrical impedance of the coil. Basic EC test equipment consists of an alternating current source (oscillator), a probe containing a coil connected to the current source, and a voltmeter that measures the voltage change across the coil [50]. When an alternating current is applied to the test coil, a primary magnetic field is established in an axial direction around the coil. As the coil approaches an electrically conductive material, the alternating magnetic field interacts with the test material, causing a circular electrical current (eddy current) to flow in the material, as predicted by Faraday's Law. This electrical current then creates its own secondary magnetic field which is, at all times, opposite in direction to the coil's magnetic field in accordance to Lenz's Law, as illustrated in Figure 2.6. The interaction between the magnetic field generated by the coil and the magnetic field generated by the eddy currents is monitored by pick-up coils or other magnetic sensing devices such as Hall device transducers or magnetoresistive devices, which give an indication of defects or any variations in the material's properties by displaying the results on the eddy current instrument [51].

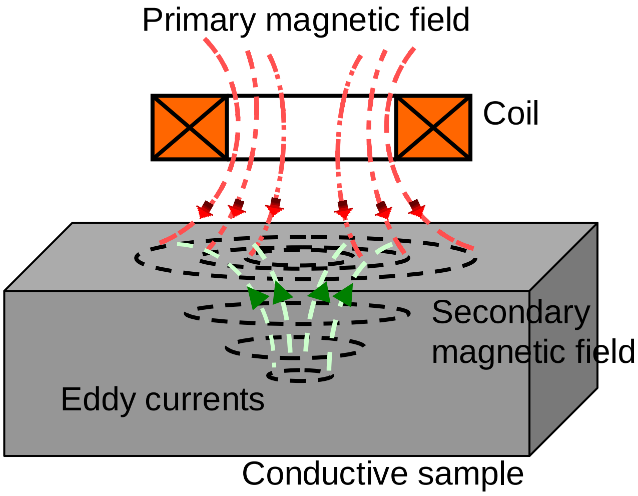

Figure 2.6: Eddy current interaction with conductive sample

Eddy currents are closed loops of induced current circulating in planes perpendicular to the magnetic flux. They normally travel parallel to the coil's winding and the eddy current flow is limited to the area of the inducing magnetic field. Eddy currents concentrate near the surface adjacent to an excitation coil and their strength decreases with distance from the coil. Eddy current density decreases exponentially with depth and this phenomenon is known as the skin effect [50]. The skin effect arises when eddy currents flowing in the sample at any depth produce magnetic fields which oppose the primary field, thus reducing the net magnetic flux and causing a decrease in current flow as the depth increases. Alternatively, eddy currents near the surface can be viewed as shielding the coil's magnetic field, thereby weakening the magnetic field at greater depths and reducing induced currents.

Phase lag is a parameter that makes it possible to obtain information from an eddy current signal about the depth of a defect within a material. Phase lag is the phase shift in time between the eddy current response from a disruption on the surface and a disruption at some distance below the surface. The generation of eddy currents can be thought of as a time-dependant process, so that the eddy currents below the surface take a little longer to be generated than those at the surface. Disruptions in the eddy currents away from the surface will thus produce more phase lag than disruptions near the surface [50].

The depth that eddy currents penetrate into a material is a function of the frequency of the excitation current and the electrical conductivity and magnetic permeability of the specimen. Therefore, the excitation frequency for EC testing is selected on the basis of the material and the depths of the defects to be detected. In obtaining the best sensor response, the sensor must induce the greatest eddy current density around the defect area [52]. The deeper the flaw, the lower the excitation frequency is needed. To date, the single frequency technique has been the most widely used among the NDE EC techniques, especially for surface and near-surface crack detection. The oscillation is sinusoidal, and may range from a few Hz up to a few MHz. The effectiveness of conventional single frequency EC NDE is limited to the identification of only one or two test conditions [53].

In order to obtain more information about the nature of the flaws embedded within a specimen, multi-frequency techniques have been proposed and used [53]. This technique is particularly useful when the defects have complex shapes, and in resolving the acquired data when it is affected by a large number of variables including conductivity, permeability, geometry and probe lift-off [54]. The limitation is its inability to perform quantitative measurements, and the difficulty of generating visualisations of the data in an intuitive manner.

To counteract some of the limitations of single and multi-frequency EC, the pulsed eddy current (PEC) technique has been introduced. PEC is currently an emerging technology in ECNDE. This technology is based on pulsed excitation current and provides new perspectives for the detection and characterisation of deep defects in the test material. It measures the transient response of the magnetic field instead of the impedance and reactance of coils used in conventional EC testing [54]. The emergence of the PEC technique is strongly supported by parallel advances in computing power and signal processing capability [52]. In recent years, PEC has gained attention in qualitative NDT [51] and extensive research has been performed in the area, thanks to its wideband spectrum excitation that is an improvement on the multi-frequency techniques. Detailed discussion of the PEC technique and investigation through modelling and experimental studies of ECNDE will be provided in the following section, along with the technique’s capabilities, and the need for improvement in defect characterisation using QNDE.

2.2 State-of-the-art in eddy current NDE (ECNDE)

One of the recent trends in ECNDE is the advancement from simple defect detection (qualitative evaluation) towards quantitative evaluation to estimate defect shape, type, size, and position [51]. Many methods have been proposed by researchers working in this field for the QNDE of materials using the EC technique [55-59]. To date, the PEC technique has been shown to exceed the capabilities of other EC techniques in the provision of quantitative information on the evaluation of defects. Apart from having a broad spectrum of frequency components in its excitation, for better eddy current penetration compared to other EC techniques, information such as the defect size, location and depth can be obtained through the features presented in the transient signal. Generally, the time-to-peak and the peak height of the PEC differential signals are the main features used to obtain the depth information and the size of the defect [60]. Despite significant advancements, characterisation of surface and deep sub-surface flaws still poses a major challenge.

The lift-off effect, where variation of the distance between the probe and the test sample changes the mutual inductance between the excitation coil and the test sample, is commonly known to be one of the main obstacles for effective PEC testing, as it can easily mask defect signals especially when the inspection involve complex geometry components i.e. aircraft components [61]. These lift-off variations can be caused by varying coating thickness, an irregular surface shape or by probe tilting during the scan [62]. Reduction of the lift-off effect has been attempted with some success using signal processing techniques, improved probe design and the construction and use of sensor arrays [63, 64].

The superiority of a magnetometer sensor over a coil system has been demonstrated with the PEC system, i.e. using a Hall device, GMR etc [64]. The use of high sensitivity magnetic detectors instead of conventional coil detectors allows the acquisition of optimum information from the component under test [50, 52]. It has been acknowledged that the sensitivity of EC technique, especially in PEC testing, is enhanced when magnetic field sensors are used instead of coils for picking up the field. Coils are not particularly sensitive to low frequency fields, where the generated electromotive force around the loop is proportional to the rate of change of the magnetic field, rather than the magnitude of the field. Therefore, the effectiveness of the coil decreases with decreasing frequency. To enhance the sensitivity and spatial resolution of the measurement, more advanced techniques based on the separation of the excitation and detection elements have been proposed [52]. For QNDE of defects, magnetic sensor arrays for PEC probes have been proposed and have exhibited greater potential for obtaining more information about defect location and orientation through the mapping of the magnetic field distribution, in addition to providing richer depth information [61-63]. With the array arrangement, more information is obtainable at a given time, and thus the probability of detection is improved.

It has been noted that PEC has demonstrated its superiority over other ECNDE methods for defect detection and characterisation. However, improvements in defect characterisation need to be explored still further in achieving better defect QNDE. This does not simply mean estimating defect location and depth, but it also means providing information about the overall geometries of defects. For 3-D defect reconstruction, accurate sizing of defects is a must. This is a major challenge in QNDE for ECNDE, as naturally occurring defects rarely have a simple geometry. This geometric complexity affects the resulting signals acquired from the interaction of eddy currents with defects. In order to fully understand the effect of defect geometry on the acquired information and to gain optimum defect information, the underlying phenomena of the interaction and their effect on the inspection results need to be understood. This understanding can be provided by a modelling approach in ECNDE, which facilitates not only the forward problem but also the inverse process, which is important for experimental design and specification as well as feature extraction for defect quantification and the reconstruction of 3-D defects.

The following sections provide an overview of the direction taken by the current research and the contribution of the approach employed to providing improved defect characterisation capabilities of ECNDE through modelling; imaging of eddy current distribution; and the potential of integrative NDE methods to tackle complex geometrical defect problems i.e. angular defects.

2.2.1 Modelling approach in ECNDE

Modelling is often used in ECNDE to simulate the eddy current phenomena and its application to NDE. In QNDE, a combined modelling/experimental approach is recommended. Establishing a good link between the modelling and experimental approaches can provide a better understanding and explanation of physical phenomena arising from practical experimental results. The constructed models in ECNDE work are typically used to simulate an eddy current test, and they provide the solution for inverse and forward problems in predicting the resulting signals associated with different defect and experimental conditions. Results of such studies are useful in EC probe design, visualisation of the interaction of EC with defects, optimising the test setup and defect identification that can be used to develop signal interpretation algorithms.

The modelling approach can be divided into analytical and numerical models with the ability to solve Maxwell's equations, in order to simulate eddy current phenomena with regard to the test environment. Sections 2.2.1.1 and 2.2.1.2 respectively will explain the application of analytical and numerical simulations for ECNDE.

2.2.1.1 Analytical simulations of ECNDE

Analytical simulations in ECNDE provide a closed-form solution to differential equations that are derived from Maxwell's Equations, or equations derived from equivalent models based on physical phenomena. This approach has shown advantages over numerical simulations in providing a fast and accurate solution, which benefits the inverse solution of ECNDE problems for the acquisition of information on the conditions of a sample from obtained signals.

Analytical modelling for ECNDE is based on Maxwell's equations, which govern the electromagnetic phenomena. Differential equations derived from Maxwell's equations predict the electromagnetic field distribution as well as its variations in electromagnetic systems. Via this approach, the closed-form solutions to the unknowns of these equations bring out the macroscopic description of electromagnetic field within ECNDE systems.

The application of analytical modelling for ECNDE began with Dodd and Deed's modelling of EC inspection applied to a coil on a conductive half-space and a 2-layered specimen including a rod specimen, using integral expressions [65, 66]. They represented the governing equations of EC inspection in cylindrical coordinates and were solved by the method of separation of variables. The first-order and second-order boundary conditions were taken into account when calculating the coefficients in the expression of the solution to the magnetic vector potential in each individual region. Since the solution has Bessel functions of the first kind, Fourier-Bessel equations were used to simplify the integration derived from boundary conditions. With the determination of the vector potential, the physical phenomena observable from electromagnetic induction are calculated for eddy current testing. The Dodd and Deeds analytical models have proved to be successful in predicting experimental data from eddy current measurements and have been widely used by the NDE community in the design of eddy current tests [1].

Work on analytical modelling for ECNDE then progressed to predicting the impedance change in an eddy current probe due to surface cracks in a material. Dodd and Deeds has shown, once the eddy current density is known, a defect can be modelled by superimposing a small current flowing in the opposite direction. With the consideration of the vector potential at the defect area and its volume, the effect of a defect is then described by calculating the impedance change [65]. Harfield and Bowler [67] presented a thin-skin analysis of eddy currents in which the electromagnetic fields on the crack faces are described in terms of a potential which obeys a two-dimensional Laplace equation. The solution is found by applying suitable boundary conditions, and the coil impedance change due to the crack is calculated from the potential. The scope of the work is limited to high frequency excitation, in which the electromagnetic skin depth is significantly smaller than the crack dimensions, and the induced eddy currents are restricted to flow in a thin skin at the surface of the conductor and at the faces of the crack. They then extended their work to model a crack as a rectangular region [68]. Boundary conditions that apply to the crack face and the boundary where the crack intersects with the surface of the conductor are determined in solving the Laplace equation. The conditions derived are valid for cracks in materials of arbitrary permeability, and the impedance change of the excitation coil due to the defect has been calculated from the harmonic solutions of the Laplace equation. Theodoulidis and Bowler have modelled a plate as a conductive half-space having a long notch with a rectangular cross section [69]. They extend the analysis of the electromagnetic field produced by a coil to account for the presence of the defect in the conductor. In obtaining the solution for a half-space with a slot, the domain of the problem is truncated into several regions and the field is expressed as a summation rather than as an integral expression.

Until now, many of the analytical packages for ECNDE modelling and simulations have not been widely commercialised, apart from CIVA that has been used in analytical simulations, particularly the modelling of EC applications for the aerospace [70], oil and gas [71] and nuclear [72] industries. Nonetheless, some self-designed software e.g. TEDDY [73], has exhibited a capability to provide the predicted impedance signals, focused on specimens with simple geometries such as stratified conductors, with the inclusion of straight notches to represent simple defects. The limitations of analytical packages are in their inability to solve complicated problems, i.e. complex defect components and geometries, which hinder the utilisation of this analytical approach towards solving real industrial problems.

2.2.1.2 Numerical simulations of ECNDE

Numerical simulations in general are more powerful than simulations using an analytical approach. In contrast to analytical simulation, numerical simulation is far more flexible and has the capacity to model complex defect geometries, material nonlinearity and other complexities associated with real test scenarios, with the required accuracy [1]. At the same time, the solution is obtained as numerical data rather than a closed form solution.

Numerical simulation methods for solving electromagnetic problems involving Partial Differential Equations (PDEs) can be categorised into two groups, according to the mesh conditions: mesh-based and meshless methods. For the group of mesh-based methods, FEM [74] originating from the Finite Difference Method (FDM) [75] is dominant in the solution of sophisticated electromagnetic problems, followed by the Finite Boundary Element Method (FBEM) [76] and Hybrid Methods, which integrate FEM and FBEM [77, 78]. In the group of meshless methods, the Element Free Galerkin (EFG) method is the most frequently used method in ECNDE [79, 80], and this is based on Smoothed Particle Hydrodynamics (SPH) methods [80].

The application of numerical simulations to ECNDE problems started with FDM, which is based on the formulation for EC inspection provided by Dodd and Deeds [81]. The equation governing eddy current properties was solved with a high accuracy. However, since FDM has limitations in dealing with complicated geometries; it was replaced by FEM, which is the dominant method for investigating ECNDE. Dai et al. applied a hybrid FEM and FDM computational model for studying PEC [82]. In contrast, FEM has been used independently for simulations of ECNDE such as EC and MFL [83-87]. FEM simulation has been developed for 2-D and 3-D models. FEM solvers for electromagnetic calculations have been expanded from magnetostatic and electrostatic solvers to transient solvers. All these present best performance of FEM for ECNDE simulations.

FEM is preferred to other numerical methods due to its flexibility in the description of the problem and its capacity to cope with nonlinear and anisotropic materials without too many restrictions; it provides fast solutions to specific electromagnetic problems and is capable of dealing with problems concerning multiphysics requirements e.g. electromagnetic issues coupling with heat diffusion [74]. Since extensive studies in the computation and implementation of FEM simulations have been conducted, such simulations have been realised by using not only self-designed programs in laboratories for specific purposes but also commercial simulation packages that can solve complex problems and particular issues defined by users. For example, the commercial packages such as COMSOL [88] and MagNet by Infolytica [89], facilitate modelling and simulation by embedding state-of-the-art FEM solvers, easy-to-use graphical interfaces, automatic as well as optimised meshing and computing algorithms and multiple post-processing functions for the display and analysis of results.

Along with the rapid development of computers, FEM simulation has been shifting from 2-D modelling to 3-D modelling, which is more suitable for handling asymmetric problems that cannot be simplified to a 2-D problem using azimuthal coordinates, for instance [90]. 3-D FEM simulation is beneficial to the theoretical study of ECNDE because the geometries of specimens and components modelled in simulations are usually asymmetric [91]. The commercial simulation packages which are prevalent in electromagnetic modelling are capable of implementing simulations not only in 2-D but also in 3-D, and so a better understanding of magnetic fields underlying the inspection systems can be obtained and used to verify the experimental results.

Even though much research work has been focused on FEM simulations for ECNDE, the drawbacks of FEM are noted: compared with analytical modelling, FEM simulations are mesh-dependent and subsequently time-consuming. In addition, tradeoffs between modelling accuracy and computing power usually need to be made, which can result in low-efficiency simulations.

2.2.2 PEC imaging in NDE

The improvement in PEC capabilities for defect characterisation is important for QNDE. PEC imaging in NDE has gained considerable research attention in both academia and industry for providing an alternative way towards improved signal interpretation. Through the imaging, clear indication of defects can be provided and information about sample conditions is obtained over a relatively large area. Information on defect location as well as defect sizing can be gathered, and this will be an important aspect if defects with complex geometries are encountered. Characteristics of defect geometries can be identified, and used to differentiate between simple defects through the comparison of the mapping profiles and extracted features, and this can provide information for defect characterisation. PEC imaging has become the subject of widespread interest because of its capability of acquiring more information, as well as the fact that it is more intuitive than traditional NDE methods and techniques in defect detection and characterisation for QNDE [92].

Various techniques have been developed to put PEC inspection data in the form of images. This has been made possible by the use of magnetic sensors for the imaging of eddy current distribution, through the mapping of magnetic field distribution using scanners or by array arrangements. In the scanning method for PEC imaging, the PEC system is linked to a scanning application. Positional information is acquired using one of many different types of scanner controlled by the scanning application software. The images are then recorded, based on the amplitude of the magnetic field distribution. QinetiQ has demonstrated the application of scanning using their TRECSCAN system (for detecting and characterising cracks in multilayered structures) to acquire images which show the ability to see between closely-spaced fasteners [93].

Sensor arrays and sensor networks have become a focus of attention in the sensor world recently. NDE methods, which are highly dependent on sensing and imaging, are no exception. Sensor arrays offer many advantages: the acquisition of more information simultaneously, an improved accuracy of detection [94], and maintaining the probe in close contact with the inspected sample during the inspection. Different approaches for eddy current arrays for magnetic field mapping have been investigated e.g. using pancake coil arrays [95], meandering winding magnetometer arrays (MWM-arrays) [96, 97], magnetic sensors arrays [98] etc. In PEC imaging, signal amplitudes are commonly used as the feature to present the C-scan images in greyscale [94, 99]. Grimberg used a super resolution method based on a maximum likelihood procedure to identify whether the sensor is on the flaw [95, 96], which can realise the edge identification with further processing of the measured signals.

The use of GMR technology for magnetic sensing looks promising due to the high sensitivity in a wide frequency range, the low cost, and the collective manufacturing process, which facilitates the construction of large array probes [100]. The GMR sensor, which is one of the families of solid state magnetic field sensors, is made up of several ferromagnetic metallic thin films that are separated by thin nonmagnetic layers, and basically measures the percent change in electrical resistance. When these layers are subjected to a magnetic field, the resistance can reduce by more than 20%. A GMR sensor has a high operation bandwidth of more than 1 MHz, with a magnetic range of -10 to +10 mT [101]. The wide bandwidth response and high sensitivity of these GMR sensors are of particular interest in PEC inspection. With their small dimensions, the use of GMR sensors can also give a high spatial resolution for defect detection. Smith et al. reported the technology of fabricating GMR sensor arrays that are promising for eddy current testing [98]. Hall sensor arrays that allow significantly faster scanning than a conventional single PEC sensor have also been demonstrated [102]. A 2-D array of GMR sensors can be built to form a magnetic imaging plane [103]. This would provide a high resolution image of a relatively large area at once, without the need to scan the probe. Using sensor arrays for PEC imaging provides a way to obtain more information about defect location and geometry, in addition to rich depth information. With the construction of more sophisticated array arrangements, the imaging technique can provide faster and more reliable inspection results for defect characterisation, assessment and reconstruction of 3-D defects [104].

Even though PEC imaging, through scanning or the use of sensor arrays, has advantages in providing the solution towards defect characterisation for QNDE, the feasibility for real-time imaging still poses a question. PEC imaging through scanning leads to low inspection efficiency due to the time taken to complete the scan and its dependence on a scanning system. Sensor arrays, on the other hand, depend on the spatial resolution of the array arrangement in providing detection sensitivity and the resolution needed for defect characterisation from the mapped distribution. For these reasons, both the suitability and the limitations of scanning and sensor arrays should be taken into consideration when the PEC imaging technique is employed for defect characterisation and QNDE.

2.2.3 Integrative NDE techniques

The reliability of defect detection within a particular sample can be increased by using several different NDE techniques, especially when the methods are particularly sensitive to different types of defects and material parameters. Complementary information can be provided by the integration of NDE techniques, which gives better inspection results and more information can thereby be acquired compared to the results from an individual technique. It can also provide a solution for the limitations posed by a single technique in acquiring the intended information and so achieving the required inspection efficiency. Integration can be achieved via combinations of NDE techniques; association of NDE data for complementary results; or incorporation of different excitation modes to provide a technique for improved inspection capabilities.

Integration of two NDE techniques has been proposed for the testing of surface defects in rail tracks. A combination of PEC and EMAT has demonstrated the capacity to accurately characterise surface-breaking defects with depths of up to 20mm. PEC is more sensitive to shallower surface cracks, discriminating defects up to 5mm deep, while the EMAT is more sensitive to surface-breaking defects between 2.5mm and 15mm deep [105]. Both techniques show good accuracy and the integration of the results enable more reliable depth measurement.

One example of a system integration study in NDE is an investigation funded by the US government into the feasibility of using multiple inspection techniques for assessing pipe wall conditions in natural gas pipelines [106]. The techniques considered for integration in the study are MFL, UT, thermal imaging and AE. Integration of MFL with thermal imaging shows the poorest results in the test due to limitations of both techniques in the identification of defect edges. On the other hand, UT and MFL produced the best integration results because these techniques give the most QNDE information relating to the geometry and location of defects.

A combination of magneto-acoustic emission (MAE) and magnetic barkhausen emission (MBE) has proved successful in characterising surface treatments, such as case hardening and peening of steel components and structures. Investigations of the utilisation of MAE and MBE integration for case depth measurement in gear steels have extended the limit for case depth measurement using MBE alone to several millimetres using complimentary MAE data [107]. Comparative MBE and MAE results from case hardened En36 gear steels are presented in the form of signal profiles and correlations are drawn between MBE and MAE profile features and domain activity within the soft core and the case hardened layer.

The utilisation of pulsed excitation in MFL has shown that pulsed magnetic flux leakage (PMFL) [108] has the potential to provide depth information through time domain analysis of the induced signal, although the technique has been more successful in the characterisation of surface defects than subsurface defects. The integration of the pulsed magnetic reluctance (PMR) probe with the PMFL probe has been proposed for the characterisation of surface and subsurface defects in ferromagnetic materials [109]. The results show that the integrated technique provides complementary information, with PMFL providing data on defect location and the characterisation of surface defects, while PMR offers subsurface defect characterisation capabilities.

Active thermography is another example of NDE technique, which utilises different modes of excitation for thermal stimulation in defect detection by thermographic images. Various modes of thermal stimulation are available for active thermography used in NDE; which can be broadly categorised into lock-in, pulsed or single frequency. In Lock-in Thermography (LT), the sample is heated periodically by a heat source. When optical heating is employed, the power output from the heat lamp is modulated by a low frequency sine wave, with frequency ω [110-113]. For inductive [114-117], and sonic [118-121] excitation, the periodic heating has two frequency components; the high frequency carrier and the low frequency amplitude modulator (ω). In order to extract phase information from the measured data, the data acquisition must be synchronised with ω, hence the term ‘lock-in’ thermography.

For Pulsed thermography, the material under inspection is briefly heated using a square or cosine pulse [122] and its temperature decay curve is recorded. The material is heated by applying a heating pulse to the material in the form of a flash from a heat lamp [123-126], a burst of sonic [127] or ultrasonic energy [128] or by inductive heating [129-131]. The surface temperature of the material first rises during the application of the pulse then decays as the thermal wave propagates by diffusion through the bulk of the material. The presence of a subsurface defect (i.e. delamination) reduces the diffusion rate, leading to a heat accumulation around the defect and consequently an area of higher temperature at the material surface with respect to the surrounding material.

Although integrative NDE techniques have shown the capacity for improving defect characterisation and inspection reliability, special attention should be given to the complexity of the integrative system and the possibility of having redundancy of information, which can provide more problems than solutions. Therefore, evaluation and initial investigations are required should integrative NDE techniques be used to overcome the limitations of individual NDE techniques. This is where numerical simulation investigations can be used to their full potential in providing the initial results and evaluating the proposed integrative NDE technique.

2.3 Summary and problems identified

An extensive literature survey of NDE techniques for defect detection and characterisation is reported in this chapter. This is followed by a brief summary of analytical and numerical methods and the simulations employed in the theoretical study of ECNDE in order to predict the resulting signals associated with different experimental conditions. The effectiveness of PEC imaging in providing alternative ways of defect characterisation and quantification in conductive materials looks promising, with the use of magnetic sensors for the mapping of magnetic field distribution by scanning or array arrangement. Integration of NDE technique has shown that the reliability of detecting defects can be increased by using several different NDE techniques. Thus, limitations of individual techniques could be overcome by implementation and utilisation of an integrative NDE technique.

It is apparent from the literature survey that there are several problems in ECNDE inspection which need to be specifically addressed, particularly those involving defects with complex geometries:

- The need of QNDE for defect characterisation. The influence of defect geometries on inspection results, especially the angle of defects relative to the surface under inspection. Defects are usually complex in shape and this poses a major problem for accurate characterisation and quantification. Most of the inspection results and findings are based on the assumption that defects encountered are taken as simple defects, i.e. straight slot or notch defects. With this assumption, the accuracy of the inspection is at risk for obtaining QNDE of defects. Therefore, a comprehensive and scientific study of angular defects and their influence on the inspection results needs to be undertaken in order to provide the knowledge and the much-needed solution in achieving quantification of defects.

- Acquiring reliable defect information and faster inspection results for defect characterisation and QNDE. Eddy current imaging for 3-D defect information through mapping and visualisation can overcome the false evaluation of defects due to geometrical characteristics. The information gathered covers a relatively wide area and is suitable for the characterisation of complex defects. Through the imaging of the resulting eddy current interaction with defects, profiles of the mapping can be linked back towards defect geometries through the identification and extraction of features, with the help of numerical simulations.

- Understanding the underlying phenomena of eddy current interaction with defects that leads to the resulting distribution responses. Implementation of study via FEM for the visualisation and mapping of the resulting distribution can provide an explanation of the inspection results and help in the analysis of eddy current and angular defect interaction for defect QNDE. This is fulfilled by using FEM e.g. implemented in MagNet and COMSOL, to simulate electromagnetic NDE involving PEC and multiphysics PEC thermography problems. Through the simulations, the solutions for inverse and forward ECNDE problems in predicting and assessing the resulting signals associated with different types of defect and experimental conditions can be provided.

- Building the relationship between the acquired information and defect characterisation. By establishing a good link between theoretical and experimental approaches, a better understanding and explanation of physical phenomena arising from practical experimental results can be provided. This includes the ability to provide 3-D shape, size and location of defects, which not only facilitates the forward problem but also inverse processes involving experimental system specification and configuration, pattern recognition, defect quantification and reconstruction of 3-D defects through the analysis of simulation results. This would open the door towards bridging the gap between theoretical and experimental studies in NDE.

Chapter 3

Theoretical background of ECNDE

In this chapter, the theoretical background of ECNDE is discussed. This applies to both modelling investigation via numerical simulations and the experimental approach. The fundamental solutions that govern ECNDE phenomena are presented, which provide the basis for the research methodology adopted in the current research to address the problems identified in Chapter 2. A numerical modelling approach for the solution of ECNDE problems is discussed before its implementation in the investigations, based on its flexibility in providing accurate predictions of experimental results. The graphical visualisation of eddy current related phenomena is presented for better explanations of the inspection outcome. Many practical ways are available for performing the task of defect characterisation but the numerical approach seems to be the most feasible in providing information about the practicality of proposed techniques, supported by experimental verification of the results.

3.1 Maxwell's equations

Since ECNDE employs electromagnetic field interaction in all its applications, each is governed by the rules of electromagnetism, specifically a series of physical laws, which comprise Maxwell-Ampere's Law (1), Faraday's Law (2) and Gauss' Law in electric (3) and magnetic (4) forms. The problem of electromagnetic analysis on a macroscopic level is that of solving Maxwell's equations subject to certain boundary conditions.

These comprise a set of equations, written in differential or integral form, describing the relationship between the electric and magnetic fields within a system.

For general time-varying magnetic fields, Maxwell's equations in differential form are [1]:

$$\nabla \times \overline{H} = \overline{J} + \frac{\partial \overline{D}}{\partial t} \qquad (3.1)$$

$$\nabla \times \overline{E} = -\frac{\partial \overline{B}}{\partial t} \qquad (3.2)$$

$$\nabla \cdot \overline{D} = \rho \qquad (3.3)$$

$$\nabla \cdot \overline{B} = 0 \qquad (3.4)$$

where, $\overline{H}$ and $\overline{B}$ denote magnetic field intensity and magnetic flux density respectively; $\overline{E}$ stands for electric field intensity; $\overline{J}$ and $\overline{D}$ are current density and electric displacement current, respectively; ρ is electric charge density and t represents time. Another fundamental relationship is the equation of continuity which is written as:

$$\nabla \cdot \overline{J} = -\frac{\partial \rho}{\partial t} \qquad (3.5)$$

The electromagnetic phenomena in a closed system can be investigated on a macroscopic level as long as Maxwell's equations are solved in conjunction with the constitutive relationships representing the properties of each material, which are shown in (3.6)-(3.8) [1]:

$$\overline{D} = \varepsilon_0 \overline{E} + \overline{P} \qquad (3.6)$$

$$\overline{B} = \mu_0 \left(\overline{H} + \overline{M} \right) \qquad (3.7)$$

$$\overline{J} = \sigma \overline{E} \qquad (3.8)$$

where $\overline{P}$ denotes the electric polarisation vector; $\overline{M}$ is the magnetisation vector; ε_0 represents the permittivity of a vacuum; μ_0 denotes the permeability of a vacuum; and σ is conductivity.

Since the wavelength of an electromagnetic wave is much larger than the dimensions of investigated systems when using frequencies up to Megahertz, as in most ENDE problems, the displacement current $\bar{D}$ vanishes. Thus (3.1) and (3.5) can be simplified to [1]:

$$\nabla \times \bar{H} = \bar{J} \tag{3.9}$$

$$\nabla \cdot \bar{J} = 0 \tag{3.10}$$

With the introduction of magnetic vector potential $\bar{A}$, the curl of which gives $\bar{B}$:

$$\bar{B} = \nabla \times \bar{A} \tag{3.11}$$

The electric field can be expressed as:

$$\bar{E} = -\nabla V - \frac{\partial \bar{A}}{\partial t} \tag{3.12}$$

where V denotes electric potential, which is scalar. Note that $\bar{A}$ satisfies the Coulomb Gauge:

$$\nabla \cdot \bar{A} = 0 \tag{3.13}$$

In consideration of (3.4) and (3.5), and substituting (3.9) into (3.11), the governing equations describing the electromagnetic field in ECNDE systems are deduced from Maxwell’s equations. For time-harmonic fields in particular, the governing equation is [1]:

$$\sigma j\omega \bar{A} + \nabla \times \left(\frac{1}{\mu} \nabla \times \bar{A} \right) - \sigma \bar{v} \times \left(\nabla \times \bar{A} \right) = \bar{J}_s \tag{3.14}$$

where μ is permeability of material; $\sigma\left(j\omega\bar{A}\right) = \bar{J}_e$ denotes eddy current density; $\bar{J}_s$ is the source current density; $\bar{v}$ denotes media velocity; σ is the electrical conductivity; ω is the angular frequency.

For time-variant fields, (3.14) changes into:

$$\sigma \frac{\partial \bar{A}}{\partial t} + \nabla \times \left(\frac{1}{\mu} \nabla \times \bar{A} \right) - \sigma \bar{v} \times \left(\nabla \times \bar{A} \right) = \bar{J}_s \tag{3.15}$$

3.2 Numerical modelling approach in solving ECNDE problems

Numerical modelling approaches such as the FEM are based on the application of iteration methods, with a prerequisite that the ECNDE problem domain of interest is discretised into a number of composite elements which make up a mesh. In conjunction with the shape function of each element, governing equations of ECNDE are substituted with interpolation functions set up in all elements. Boundary conditions assigned set up the initial values, which are iterated on each element node. The iteration does not halt until the residual is less than the error tolerance.

Numerical modelling approaches to solving time-stepping problems have significant advantages over analytical methods of ECNDE when investigating samples having defects with complicated shapes and arbitrarily shaped surfaces. They can provide closer fits to the nonlinear ECNDE problem because of their better description of problem geometries and properties by means of discretisation. They can achieve the required accuracy but with flexibility in modelling complex cases which is not available to analytical or experimental modelling [1]. However, numerical methods mostly rely on the conditions of elements and mesh. Using a denser mesh will achieve a better computational accuracy, with the disadvantage of requiring a longer computing time.

In order to provide guidelines for the PEC and PEC thermography investigations performed throughout the study, a series of simulations have been conducted, which involve time-stepping FEM simulations in a 3-D environment. Commercial FEM simulation packages COMSOL Multiphysics by COMSOL [88] and MagNet by Infolytica [89] were employed, as different FEM simulation software packages have different strengths.

A general introduction to these two packages, along with the relevant information for modelling PEC and PEC thermography problems, is presented in the following, Sections 3.2.1 and 3.2.2. Using these simulation packages, the forward problem of PEC and PEC thermography inspection of angular defects has been investigated, via the time-stepping method which uses the transient solver. For PEC investigations, MagNet is used to predict the resultant magnetic field distribution from the interaction between the induced eddy currents and angular defects. For PEC thermography, when the phenomena need a multiphysics-solving capacity to add resistive heating from the induction currents as a heat source, COMSOL is utilised.

3.2.1 Solving PEC problems via MagNet

MagNet is a numerical simulation software package for the analysis of static or time-varying electromagnetic fields. MagNet implements FEM for a quick and accurate solution to Maxwell's equations. Different modules in MagNet are designed to simulate different types of electromagnetic fields, relevant to applications such as machines, sensors and transformers, either in time-harmonic or transient solver.

In providing the solutions for PEC investigations, MagNet has been used to solve the problems via the transient 3-D solver. The solutions for the models were acquired by solving the time-variant field's equation in (3.15), particularly for the magnetic field within the constructed models.

In the 3-D FEM of analysis, the model is divided into a mesh of tetrahedral-shaped elements. Each element is defined by four vertices (nodes). The vector field inside each element is represented by a polynomial with unknown coefficients. Finite element analysis gives the solution of the set of equations for the unknown coefficients. The accuracy of the solution depends upon the nature of the field and the size of the mesh elements. In regions where the direction or magnitude of the field is changing rapidly, higher accuracy requires smaller elements.

The transient solutions in MagNet are obtained by the time-stepping method. The transient solver begins by finding a static solution for the fields that would exist, assuming the conditions at the start time held unchanged for all earlier times. The transient solution then develops from this starting condition. Fixed-interval time steps are used for the solutions and at each step, the change in the solution is monitored until the specified number of steps has been reached.

3.2.2 Solving PEC thermography problems via COMSOL Multiphysics

COMSOL Multiphysics is a multiphysics modelling package for numerical simulation of physical processes which can be described using partial differential equations

(PDEs). State-of-the-art solvers are embedded in the package for users to address complicated problems quickly and accurately. It contains specific modules for different applications in Chemical Engineering, Earth Sciences, Heat Transfer, Micro-electromechanical system (MEMS), Structural Mechanics and Electromagnetics.

In providing the solutions for PEC thermography, COMSOL Multiphysics has been utilised to simulate the eddy current and temperature distribution via the Electro-Thermal module which combines the application mode for induction currents with general heat transfer. The predefined interaction adds the resistive heating from the induction currents as a heat source in the application mode for the heat transfer.

When an electromagnetic field is applied to a conductive material, the temperature of the material increases due to resistive heating from the induced eddy current, which is known as Joule heating. Solving the magnetic field propagation simultaneously with the heat transfer is therefore crucial for an accurate description of the whole simulated system. The governing equations to be solved for magnetic field propagation and heat transfer are given by (3.14) above and (3.16) below [89]:

$$\rho C_P \frac{\partial T}{\partial t} - \nabla \cdot k \nabla T = Q \tag{3.16}$$

where ρ is the density, C_P is the specific heat capacity, k is the thermal conductivity, and Q is the inductive heating (heat source density).

The sum of the generated heat (Q) is proportional to the square of electric current density, J_s. Current density, in turn, is proportional to the electric field intensity vector E. These relationships are taken into consideration when solving the numerical problem and can be expressed by the following equation [89]:

$$Q = \frac{1}{\sigma}\left|J_s\right|^2 = \frac{1}{\sigma}\left|\sigma E\right|^2 \tag{3.17}$$

σ, which represents the temperature-dependent electrical conductivity of a material, $\sigma = \sigma(T)$, is given by the expression:

$$\sigma = \frac{\sigma_0}{1+\alpha\left(T - T_0\right)} \tag{3.18}$$

where σ_0 is the conductivity at the reference temperature, T_0 , and α is coefficient of resistivity, which describes how resistivity varies with temperature.

Eq. 3.18 shows the dependency of conductivity on temperature change. In metals, conductivity decreases with increasing temperature. This will also be reflected in the eddy current propagation inside the sample, as the conductivity value changes with temperature, thus giving an accurate representation of the induction heating phenomena.

The governing equations introduced above are solved numerically using the time-stepping method in FEM for an accurate description of the heating mechanism around a particular defect.

3.3 Experimental approach in solving ECNDE problems

The theoretical background applies to experimental investigation of ECNDE, since the electromagnetic properties underlying the inspection systems are also governed by Maxwell’s equations. Consequently the measured signals can be analysed via comparison with the predicted signals. The effective interpretation and analysis of measured signals can be conducted alongside the investigation of electromagnetic phenomena that are consistent with theoretical background.

Dedicated set-ups play a vital role in the experimental study of ECNDE. Basically, the set-up comprises excitation sources, for generating the electromagnetic field injected into the sample under evaluation, sensing modules for measuring and quantifying the electromagnetic field, signal conditioning and processing that provide automatic and systematic results for the experiment by using sophisticated designs in hardware and dedicated algorithms in software.

The experimental approach to solving ECNDE problems is derived from measurements in eddy current tests, either actual or simulated. Both analytical and numerical modelling relies on experimental verification of results to validate and evaluate the findings of the modelling approach. Modelling has the potential to reduce the need for trial and error, the manufacturing of sample components and it provides an alternative to actual experimental tests that are difficult, hazardous or costly in their implementation.

The strong relationship between experimental and numerical approaches in ECNDE has contributed to the improvement of practical experimental systems in solving ECNDE problems. Apart from providing guidelines for experimental designs and system development, e.g. coil design; test frequency selection and optimisation; and interpretation of test results, numerical modelling with its versatility and accuracy has provided an alternative approach to evaluating experimental technique and systems. In other words, the combination of experimental and modelling approaches has given progressive benefits in solving inverse and forward problems of ECNDE.

3.4 Research methodology

In order to address the problems of defect characterisation in ECNDE outlined in Chapter 2, a series of investigations via PEC and PEC thermography techniques were conducted. These investigations used modelling and experimental approaches by means of visualisation and mapping of the resulting responses either via magnetic field distribution (PEC) or temperature distribution (PEC thermography). This study focuses on the characterisation of angular defects using extracted features from the responses of the eddy currents' interaction with defects inside the investigated sample. Identification of these features was made possible by analysis of the simulation results. Apart from having the capacity to model complex defect geometries, simulations using numerical modelling have been shown to provide accuracy of test results [132] and defect characterisation parameters [3] in ECNDE.

Numerical simulations are performed prior to experiments using either the PEC or the PEC thermography technique, in order to provide an expected response from defects. The simulations also provide guidelines for experimental designs; an understanding of the underlying physics surrounding a particular defect; and the means for feature extraction from the acquired responses. The experimental investigations are performed to verify the simulation results and to demonstrate the feasibility of techniques to be used in acquiring information about a particular defect. As illustrated in Figure 3.1, the work covers: (1) Investigation of the capabilities of the PEC testing technique for the characterisation of angular defects, based on the mapping and visualisation of magnetic field distribution; (2) Evaluation of the PEC thermography technique's potential to overcome the limitations of the PEC technique for defect characterisation; (3) QNDE investigation of angular defects using features extracted from the simulated temperature distribution, with experimental work undertaken for verification; (4) Feasibility study using the PEC thermography technique for defect assessment on rail heads. Sections 3.4.1 and 3.4.2 will provide outlines of the approaches taken in the research.

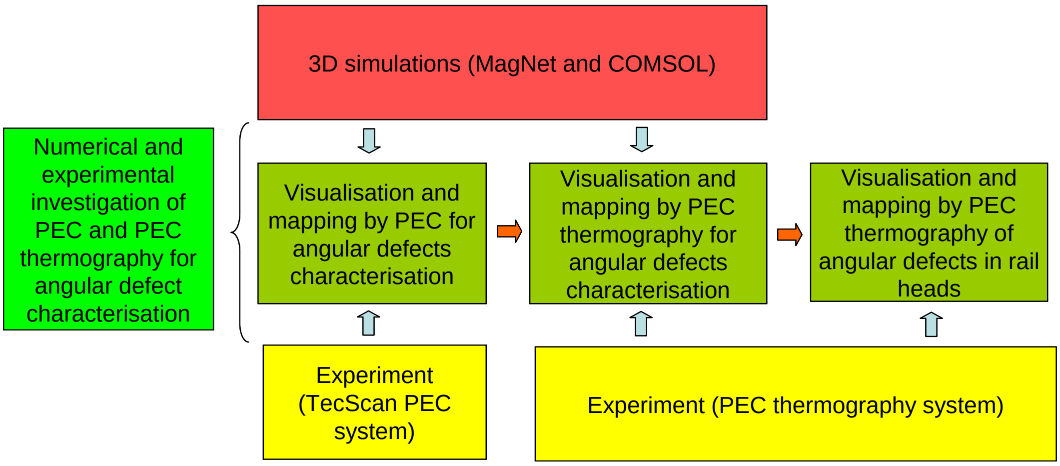

Figure 3.1: Overview of the implemented methodological approach

3.4.1 *Numerical investigations via FEM simulations*

3.4.1.1 Numerical investigations of PEC NDE

The FEM simulations for the PEC technique are performed by the transient solver, via the time-stepping method implemented in MagNet. For the study of the PEC technique for defect characterisation presented in Chapter 4, an investigation of the pulse width selection used in the study of angular defects is first undertaken. To implement this, Fourier transformations are performed on the acquired response pulses. These are in the time-domain, displayed in the form of a spectrum distribution which shows the variation of amplitude with frequency. Different depth responses which are related to the eddy current skin effect phenomena are then obtained, and explained by analysing the simulated spectrum distribution under different pulse widths. The investigation helps to decide the selection of the pulse width to be used in the characterisation of angular defects investigation. It also provides the means to verify the modelling of PEC by 3-D numerical investigations conducted in MagNet.

The investigation of PEC testing for angular defects is then performed through the mapping of simulated magnetic field distribution. A forward approach of characterising the angular defects is taken, based on the visualisation of the resultant magnetic field mapping of the interaction between the eddy current and the angular defects modelled in a 3-D environment. In the case of angular defects, the characterisation is made based on how the mapped eddy current distribution changes with angular defects having different angles. Features from the mapping are then extracted for the characterisation of the angular defect. Particularly, the potential of 3-D visualisation of magnetic field distribution for complex defect characterisation via the PEC technique is explored. From the investigation, the suitability of the PEC technique for defect characterisation through the visualisation of magnetic field distribution can be assessed in terms of its experimental practicality.

3.4.1.2 Numerical investigations of PEC thermography NDE

PEC thermography is proposed as an alternative technique for the mapping of the responses from the eddy current and defect interaction. Towards understanding the fundamental behaviour of eddy current heating and heating diffusion, Chapter 5 presents FEM simulation investigations performed to predict the thermographic behaviour of two fundamental defects; a slot and a notch. From the simulations, the heating mechanism around a particular defect can be visualised, and how the thermographic response distributes itself in the presence of a defect can be understood. These simulation results and analyses help in the evaluation of the PEC thermography technique to overcome the limitations of the PEC technique for defect characterisation. Through the investigation, guidelines for experimental designs can be acquired to fulfil the requirements needed for characterisation of defects via the PEC thermography technique.

For the QNDE investigation of angular defects via the PEC thermography technique presented in Chapter 6, FEM simulations are performed in order to provide initial results and analyses of the capabilities of the technique for 3-D defect characterisation. From the simulations, the interaction between the induced eddy currents and the angular defects is first visualised and then resulting thermographic responses are analysed to provide an explanation of heating distribution and for pattern recognition of the angular defect.

Following the analysis of thermographic responses from the angular defect, features have been identified and extracted for angular defect characterisation. These features provide geometrical information on the investigated angular defects.

3.4.2 Experimental investigations

The experimental study focusses on the verification of the findings from the numerical simulations for the characterisation of angular defects. Since there are two techniques involved throughout the study; PEC and PEC thermography, two experimental setups are employed.

For the PEC investigations, the system consists of a TecScan PEC system and a PEC probe having an outer excitation coil (driver coil), concentric with a pickup coil having a ferrite core at the centre. The investigated sample is made of three layers of 1mm thick 2024 T3 aluminium (electrical conductivity 29.6-30.1 %IACS). Each layer contained a through-wall hole of 4.5mm diameter which is aligned along the scanning axis. These holes are used in the PEC experimental study to simulate different locations of defects inside a sample, using varied pulse width excitation. As the probe is moved along the scanning axis of the sample, transient responses for different pulse widths are acquired as C-scan images. The C-Scan results are then analysed to validate the results obtained through FEM simulations.

The system setup of the PEC thermography system consists of an induction heating control box which supplies power to the work head. The work head contains a transformer-coupled resonant circuit, including two capacitors and the excitation coil itself. The excitation of the coil is controlled by the function generator, which also controls the heating duration of the experiment. The excitation frequency is dictated by the values of the capacitors, the inductance of the coil and the load of the circuit, i.e. the material, volume and proximity of the sample under inspection. A PC which is linked to the IR camera stores the thermal images captured by the camera for subsequent analysis.

In the PEC thermography investigations, two different Infrared (IR) cameras are employed to capture the themographic distributions. A DeltaTherm 1410 IR camera system is used for the evaluation of the PEC thermography technique for defect assessment. Through the evaluation, it was concluded that a higher resolution and a camera which can operate at a higher speed is needed for an optimum investigation using the PEC thermography technique. Therefore, a FLIR SC7500 IR camera system is then used for the QNDE investigation of angular defects. These IR camera systems are constructed by Cheltenham Induction Heating Ltd., around the Easyheat induction heating system. The Easyheat system has a maximum excitation power of 2.4kW, a maximum current of 400 RMS and an excitation frequency range of 150 kHz – 400 kHz.

The thermal image sequences generated by the developed system are analysed in terms of:

- The temperature distribution within a single image; for example the image at the end of the heating sequence
- The development of heating over time in one or more positions on the sample surface

Prior to testing, all samples are painted with a black acrylic paint to increase and even out the thermal emissivity at the sample surface.

3.5 Summary

In this chapter, a brief introduction to Maxwell's equations that govern electromagnetism, and the equations derived from them, has been presented. Based on the aims and objectives of the research, a numerical modelling and an experimental approach to solving ECNDE problems are presented and summarised. The methodology for the research, via numerical modelling and experimental investigations by means of visualisation and mapping of the resulting responses for PEC and PEC thermography, is then presented.

Following the description of the implementation of study for the research, the remainder of the thesis in Chapters 4-7 will report the results of the investigations of eddy current distribution for angular defect characterisation through the modelling and experimental approaches. This will be implemented by the visualisation and mapping of the resulting responses of the eddy current interaction with defects, using the PEC and PEC thermography techniques.

Chapter 4

PEC for the characterisation of angular defects

The PEC testing technique, based on mapping a magnetic field distribution within a sample, is investigated in this chapter. Angular defect characterisation is achieved through a combination of numerical simulations and experimental studies. We begin with an investigation of variations in PEC pulse width for defect detection at various depths. Numerical investigations with variable pulse widths of constant period are initially performed in order to visualise the effect of pulse width variation on frequency-dependent amplitude in the spectrum analysis. This forms the basis for explaining the effect of pulse width variations on the magnetic field distribution as affected by defects located at different depths in a multilayer conductive sample. With the information so obtained, a suitable pulse width for the PEC technique can be determined. The subsequent experimental investigations provide the means to verify the modelling of PEC by the 3-D numerical investigations conducted in MagNet.

The study subsequently proceeds to the investigation of PEC for the characterisation of angular defects in 3-D, through the mapping of a magnetic field distribution. This provides an alternative and improved technique for defect characterisation when compared with the imaging of an eddy current distribution.

4.1 PEC defect detection at various depths

When predicting the lifetime of a component, rigorous damage-tolerance calculations should take into account not only the size, but also the location, of any defect and how it extends within the examined component. This is especially true in aircraft structures, which are normally composed of multiple layers of variable thickness made up of different materials. For example, in the description of a defect which extends deep inside a sample, the depth penetration of the eddy currents must be sufficient to produce a detailed defect characterisation.

PEC testing has the advantage of having a deeper penetration than does conventional eddy current testing. From a single excitation procedure, better information on defects in electrically conductive materials can be obtained via the PEC technique, due to the low frequencies in the pulse spectrum used for the excitation of the driving coil. However, quantifying the depth of a defect using this technique remains a major challenge, since the signal features in the time domain are not linearly correlated to the depth of the defect.

The frequency spectrum contained in the excitation pulse for PEC depends on both the period and the pulse width of this waveform. The exact nature of this excitation current varies between the different PEC systems, but a typical form is shown in Figure 4.1. The effect than influence the driving coil comes from the interaction between the magnetic field from the excitation coil and the magnetic field coming from the sample. The pulse follows the profile as shown in Figure 4.1, due to the time it takes for the eddy current to diffuse in the sample. In a current driven excitation, the current is directly proportional to the magnetic field with constant amplitude. With this, the same magnetic field is introduced in the sample, regardless of the local changes that might happen in the sample under the excitation coil.

The pulses contained in the excitation are rich in high and low frequency components, which give the PEC technique more flexibility for inspection and defect characterisation. The present study utilises these frequency components to distinguish between defects close to the surface and those located in deeper layers within a multilayered structure. This pulse width variation methodology extends previous PEC research by using pulses with different pulse widths of constant period. This allows an identification of the suitable pulse width that gives the required eddy current depth of penetration for the characterisation of defects within the scope of the study. It also provides the means to verify the 3-D modelling and simulation of PEC conducted in MagNet.

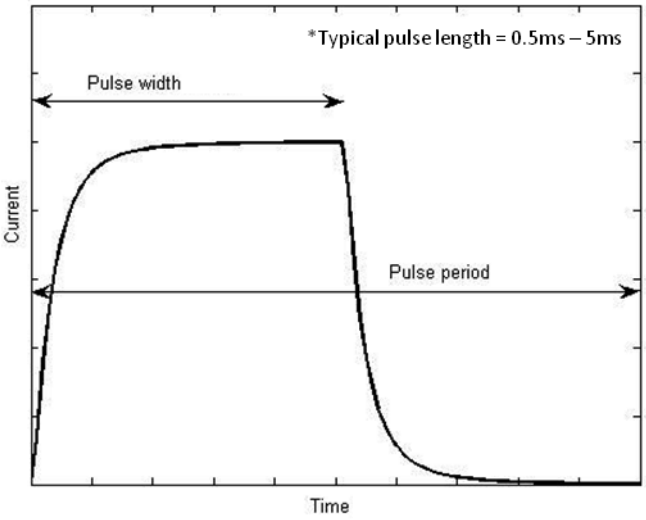

Figure 4.1: A typical PEC excitation pulse waveform

4.1.1 Investigation background

PEC numerical simulations and experimental investigations with variable pulse widths of constant period are performed in order to establish the effect of pulse width variation on the magnetic field distribution inside a three-layer, electrically conductive sample. The pulse width variations provide different frequency spectra, providing more detailed information from the broadband frequency harmonics than is available from a single excitation process.

The PEC probe used for this study consists of an outer excitation coil (driver coil), concentric with a pickup coil having a ferrite core at the centre. Figure 4.2 shows the schematic presentation of the probe configuration. Table 4.1 provides the dimensional and electrical characteristics of the driver and pickup coil used in the collaborative work with Dr Catalin Mandache from the National Research Council (NRC) of Canada, funded by the Royal Society of UK, which resulted in the experimental results presented in section 4.1.3 of this chapter.

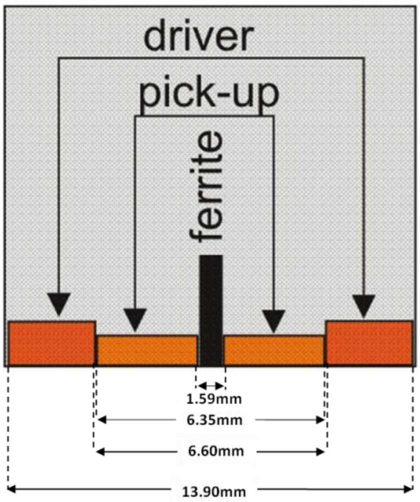

Figure 4.2: The PEC probe configuration used in the study which consists of a driver coil, a pickup coil and a ferrite core

Table 4.1: Parameters of the driver and pickup coil

	Driver Coil	Pickup Coil
OD (mm)	13.9	6.35
ID (mm)	6.6	1.59
Height (mm)	0.685	0.660
No. of Turns	400	625
DC Resistance (Ohm)	62.31 ± 0.01	91.99 ± 0.01
Inductance (mH)	2.140 ± 0.01	1.903 ± 0.01
Lift-off (mm)	0.15	0.15

The investigated sample is made of three layers of 1mm thick 2024 T3 aluminium (electrical conductivity 29.6-30.1 %IACS) provided by NRC, Canada. Each layer contained a through-wall hole of 4.5mm diameter which is aligned along the scanning axis. These holes were used in the experimental study to simulate different locations of defects inside a sample for different depth of penetration at different pulse widths. The present work takes advantage of the PEC technique in order to distinguish defects close to the surface from ones located in deeper layers in a multilayer structure, with direct application to the evaluation of aircraft structures. Figure 4.3 shows the schematic diagram of the probe and multilayered sample as used in the investigation.

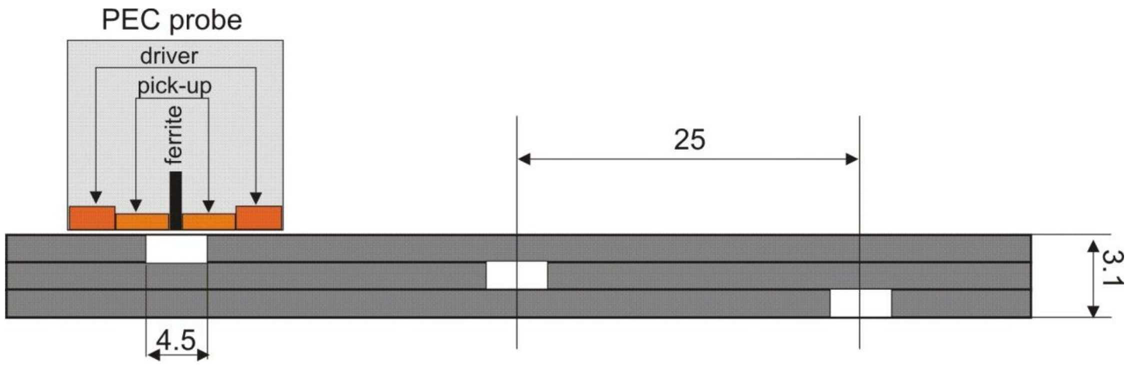

Figure 4.3: Schematic representation of the probe and multilayered aluminium sample having holes at each layer of the sample (the dimensions are given in mm; the drawing is not to scale)

A rectangular waveform of 10V amplitude and 1ms period is used to feed the driver coil to match the setup used in the experimental investigations. Six different pulse widths were investigated, of 0.01ms, 0.02ms, 0.05ms, 0.1ms, 0.2ms and 0.5ms, which correspond respectively to 1%, 2%, 5%, 10%, 20% and 50% pulse widths.

The simulation model of the probe and the multilayered aluminium sample is built in MagNet with 3-D coordinates to implement a better description of the problem. Taking into consideration the symmetrical geometry of the problem, the probe and sample are modelled as a half model and solved using the time-stepping 3-D transient solver. Due to the physical phenomena of electromagnetic field, the electric field and magnetic field should be continuous over the interfaces of each two layers. Therefore, continuous boundary conditions are assigned at each subdomain boundaries in the multilayered aluminium sample model, in order to realise the different layers and the borders of the sample. In the FEM analysis, the model is divided into a mesh of tetrahedral-shaped elements. In order to get better results in 3-D, a fine mesh is generated within the region of interest. The mesh quality is enhanced around the region where the direction or magnitude of the magnetic field is changing rapidly, by setting the maximum element size for a component volume, which reflects the area between the coils and the sample. Details and descriptions of the modelling and simulation setup for PEC conducted in MagNet are presented in Appendix A.

The simulation studies are performed prior to the experimental investigation in order to provide predicted responses from the PEC probe in the time-domain representations. By analysing these responses, pulse widths in the PEC excitation waveform can be selected on the basis of the eddy current's required depth of penetration into the sample under study.

4.1.2 Spectrum analysis and modelling results

Figure 4.4 shows the layout of the coil and sample modelled as a half model in MagNet and solved as a 3-D problem. In the time-stepping FEM, the transient responses are acquired when the probe is positioned on top of the specimen with a lift-off distance of 0.5mm, above an unflawed area. This ensures that the simulated responses are not influenced by the presence of a defect and can act as reference responses in the subsequent analysis.

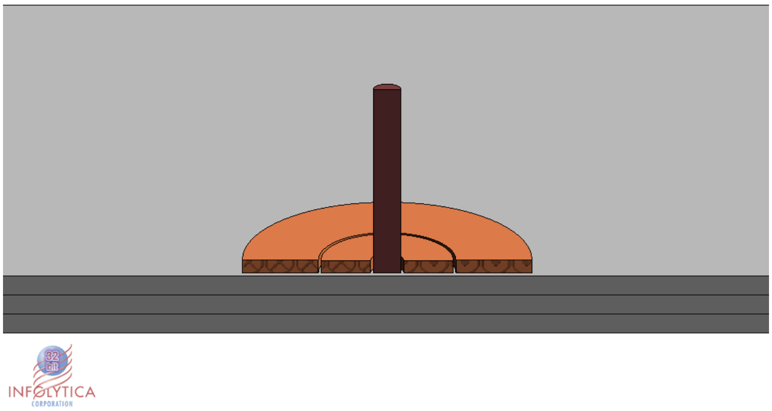

Figure 4.4: 3D axi-symmetric model of the coil with a lift-off distance of 0.5mm above an unflawed area of the multilayered aluminium sample

The simulated transient responses from the unflawed area, for 1%, 2%, 5%, 10%, 20%, and 50% pulse widths are shown in Figure 4.5. Figure 4.5a shows the excitation current input flowing inside the coil with varied pulse width. Figure 4.5b shows the voltage readout from the pickup coil, depicting the difference in the signal profiles with different pulse widths in the presence of the aluminium sample; these transient responses are due to the interaction between the primary magnetic field from the driver coil and the secondary magnetic field from the induced eddy currents.

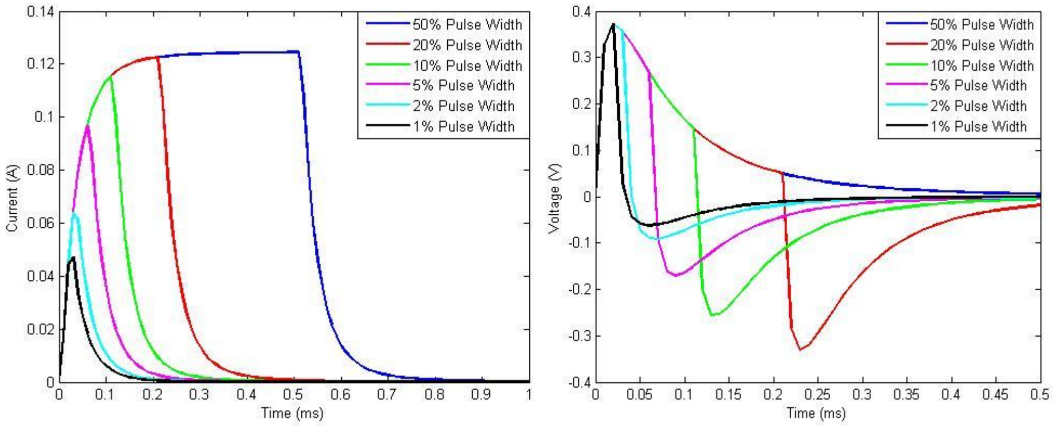

a) b)

Figure 4.5: Numerical modelling results - time domain representations of: a) Excitation current input with varied pulse width, b) Transient response on an unflawed section of the multilayered aluminium sample with varied pulse width.

The inspection sensitivity in PEC has a close relationship with the eddy current penetration depth, which is inversely proportional to the square root of the frequency. The depth of penetration decreases with increasing frequency and increasing electrical conductivity and magnetic permeability. The depth at which eddy current density has decreased to 1/e, or about 37% of the surface density, is called the standard depth of penetration (δ_{ec}). The word ‘standard’ denotes plane wave electromagnetic field excitation within the sample (conditions which are rarely achieved in practice). Although eddy currents penetrate deeper than one standard depth of penetration, they decrease rapidly with depth. At two standard depths of penetration ($2\delta_{ec}$), eddy current density has decreased to the square of 1/e, or approximately 13.5% of the surface density. At three standard depths ($3\delta_{ec}$), the eddy current density is only approximately 5% of the surface density [50]. In the existing literature, much importance is attached to the relationship between electromagnetic skin depth and defect depth, but as the skin depth formula is only applicable to perfectly flat and flawless samples, this relationship can provide, at best, only a rough guide when inspecting defected samples.

By performing a Fourier transformation, the pulse acquired by a pickup coil in the time domain can be displayed in the form of a spectrum distribution which shows the variation of amplitude (magnitude) with frequency, as shown in Figure 4.6. Different depth responses which are related to the eddy current skin effect phenomena can then be obtained by analysing the simulated spectrum distribution under different pulse widths.

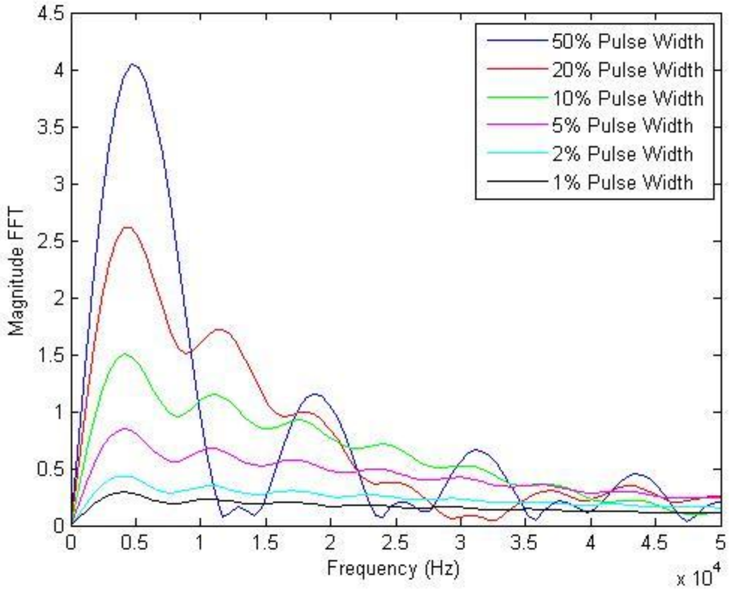

Figure 4.6: Simulated spectrum distribution under different pulse width which shows the change in amplitude of the signals

The simulated frequency spectrum obtained from the different pulse widths shows that wider pulses are richer than narrower pulses in low frequency components. For wider pulses, the low frequency components are dominant, thus giving relatively deeper eddy current penetration. As the pulse width decreases, the high frequency components prevail and the induced eddy currents become more concentrated at the surface layer of the inspected sample. Given that the frequency dictates the penetration depth of the eddy currents into a conductive sample, the resulting responses are expected to indicate eddy current interactions with defects at different depths. This will reflect the maximum depth covered by the frequency spectrum for the specific excitation pulse width. The results can be utilised for the practical application of defect depth discrimination and quantification.

4.1.3 Experimental results

Experimental investigations were performed using a TecScan PEC system and the PEC probe described in Table 4.1. Transient responses are initially recorded for 1%, 2%, 5%, 10%, 20%, and 50% pulse width, with the probe having a lift-off of 0.5mm, placed on an unflawed area of the aluminium sample. When the responses, shown in Figure 4.7, are compared with the simulation results seen in Figure 4.5b, it can be seen that there is a good agreement between them.

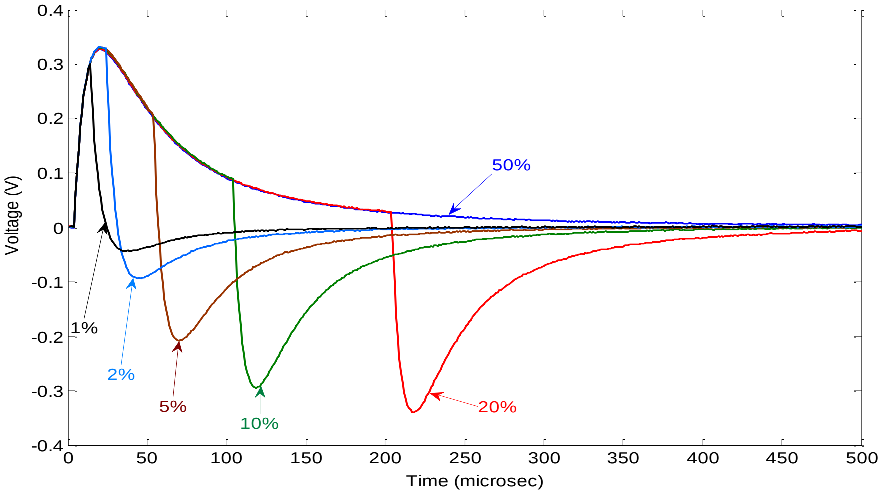

Figure 4.7: Time-domain transient responses obtained experimentally on an unflawed section of the aluminium sample for different pulse widths (probe lift-off = 0.5mm)

In the defect detection analysis of the holes located at different depth inside the sample (as illustrated in Figure 4.3), transient responses are acquired in the form of C-scan images for the different pulse widths as the probe is scanned along the scanning axis of the sample. It is expected that through this investigation, we can estimate a suitable pulse width to be used so that the PEC technique for the characterisation of angular defects will cover sufficient depth inside the investigated sample.

The signal feature investigated in the experimental study is the standard deviation of the signal gathered by the pickup coil. This quantity represents how widely the recorded data is displaced from the average transient signal value acquired from the entire scanned area, and for a vector signal containing *N* samples, it uses the following relationship for data analysis:

$$V_{STD} = \left[\frac{1}{N-1} \sum_{i=1}^{N} (V_i - V_{mean})^2 \right]^{1/2} \tag{4.1}$$

where V_{STD} is the standard deviation voltage of the transient response, V_i is the voltage value sampled at the time step *i*, and V_{mean} is the average voltage value of the transient signal.

Figures 4.8 to 4.11 present the normalised C-scan results for excitation waveforms of 2%, 5%, 10%, and 50% pulse width, respectively. The scanned area represented a surface of 32mm x 75mm, with a scanning step of 0.25mm in both directions.

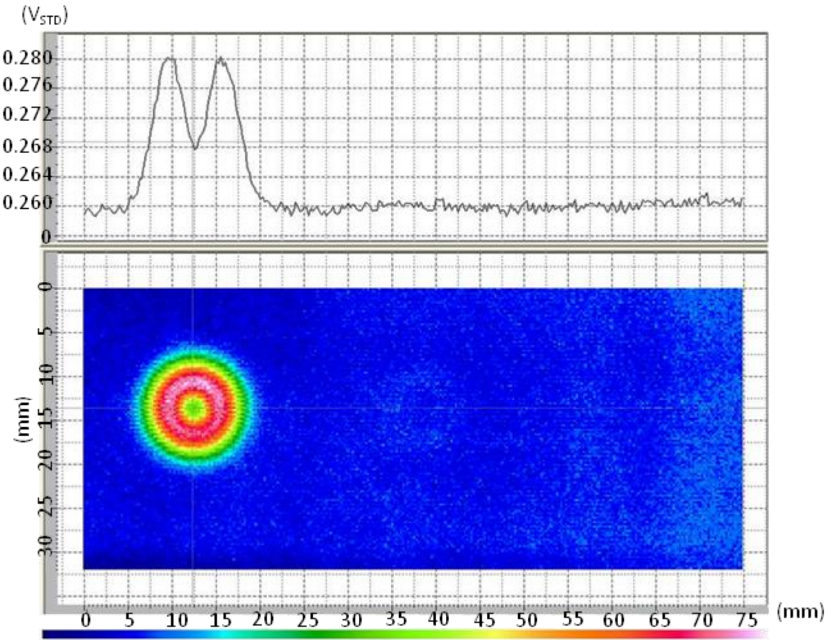

Figure 4.8: Normalised data obtained from the experiment for an excitation pulse width of 0.02ms (duty cycle of 2%), signal period of 1ms

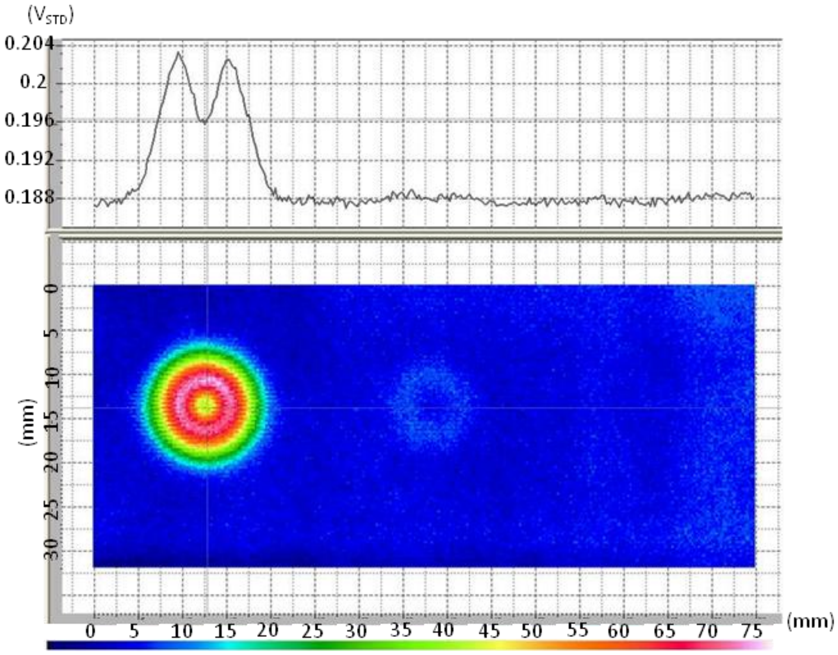

Figure 4.9: Normalised data obtained from the experiment for an excitation pulse width of 0.05ms (duty cycle of 5%), signal period of 1ms

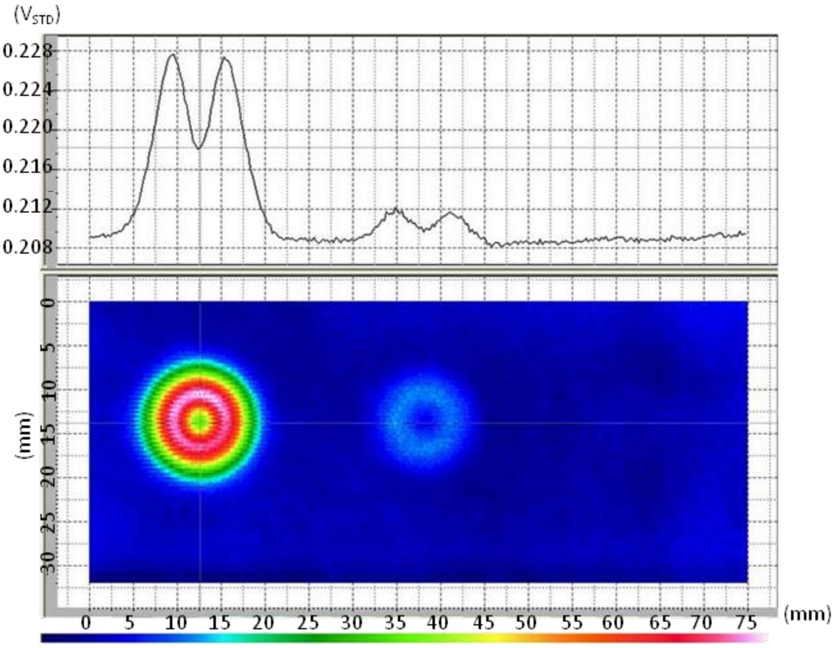

Figure 4.10: Normalised data obtained from the experiment for an excitation pulse width of 0.1ms (duty cycle of 10%), signal period of 1ms

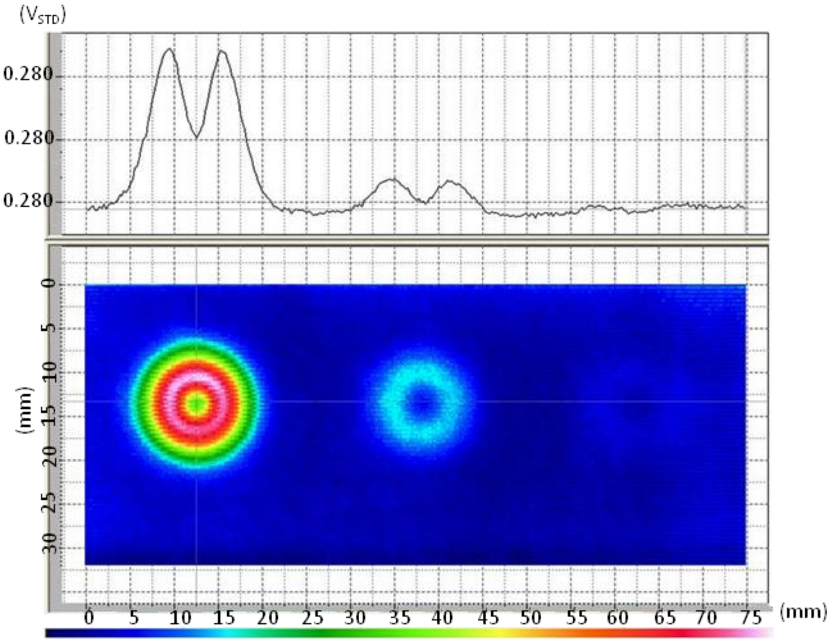

Figure 4.11: Normalised data obtained from the experiment for an excitation pulse width of 0.5ms (duty cycle of 50%), signal period of 1ms

The C-scan results shown in Figures 4.8 – 4.11 confirm the earlier results from the simulations. For the shorter pulse widths of 2% and 5%, the top defect can be clearly detected but there are scarce indications of the defect located at the second layer. Increasing the pulse width gives more information from the second and third layers, without losing information regarding the top layer defect. These experiments validate the results obtained through the numerical simulations presented previously in section 4.1.2, which indicated that the spectrum distributions contained in different pulse widths give different depth profiles under (otherwise) the same testing procedure. In other words, shorter pulse widths which are richer in higher frequencies are more appropriate for eddy current inspections of defects closer to the surface. Wider pulse widths contain lower frequency components and allow deeper penetrability of the eddy currents. To summarise, for an investigation of defects which extend deep inside the sample, a wider pulse width should be chosen for the excitation. The skin depth formula can provide a guideline for the length of the pulse width to be used, but the final decision should be based on the deepest depth of detection by the chosen pulse width.

In the varied pulse width investigation, a defect 3mm deep could be detected with a 50ms pulse width. For a defect which is deeper than this, a wider pulse width should be used. Since the angular defects modelled in the study extend 5mm into the sample, a 1ms pulse width is to be used in the following experimental investigation, presented in Section 4.2. The wealth of low frequency components with this pulse width provides the required eddy current depth penetration for angular defect characterisation with the designated defect geometries.

4.2 Magnetic field mapping for angular defects characterisation

To analyse PEC testing on complex geometrical defects, i.e. angular defects, the FEM time-stepping method is applied to a 3-D transient problem. A forward approach of characterising the angular defects has been taken, based on the extracted features of the resultant magnetic field mapping from the interaction between the eddy current and the defects in the sample.

4.2.1 Simulation model and setup

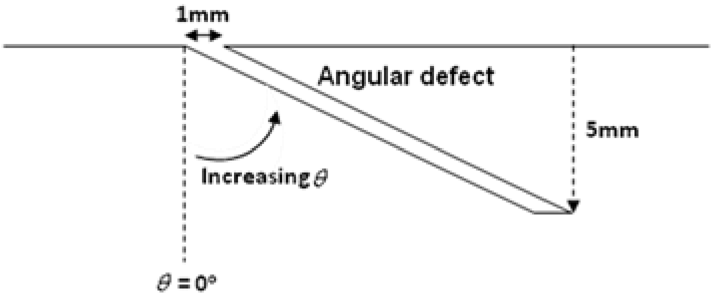

Figure 4.12: Illustration of the angular defect modelled in the simulation having a depth of 5mm, 1mm in width and the angle of the defect, θ

In the simulation, the coil used has the dimensions of 14mm inner diameter, 16 mm outer diameter, 1 mm height and 1000 turns of wires, and is current-driven with a rectangular waveform of 1 Ampere amplitude to generate a varying magnetic field. Aluminium samples are modelled with long angular defects in the form of notches which cut through the length of the sample. These are at a depth of 5mm, have a width of 1mm and are set at angles of 0º, 10º, 20º, 30º and 40º, as shown in Figure 4.12. What will henceforth be referred to as “the angle of the defect, θ” is in fact the angle between the defect axis and a perpendicular to the sample surface. The resulting magnetic field along the coil axis, which is vertical to the sample surface, is visualised for the 3-D transient magnetic field mapping of the angular defects. As analysed in the pulse width variation investigations, a wider pulse should be utilised for deeper eddy current penetration. This is why a pulse width of 1ms in length is used in this investigation, so that the eddy currents can penetrate the sample sufficiently to cover the depth of the angular defect inside it. Figure 4.13 illustrates the excitation current input waveform used to drive the coil.

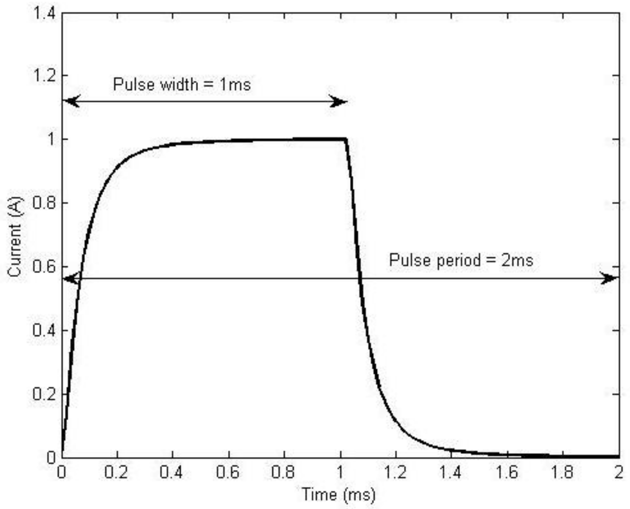

Figure 4.13: Coil excitation current input waveform

In the time-stepping FEM, the transient magnetic field visualisation is made when the coil is positioned above the defect opening with a lift-off of 0.5mm. The time step of the pulse waveform is 0.01ms with a 1ms excitation pulse width. The time step used in the simulation is the setting which can provide sufficient information to represents the pulse waveform. All simulations are performed using MagNet. Figure 4.14 shows the layout of the coil and the sample, modelled as a 3-D problem.

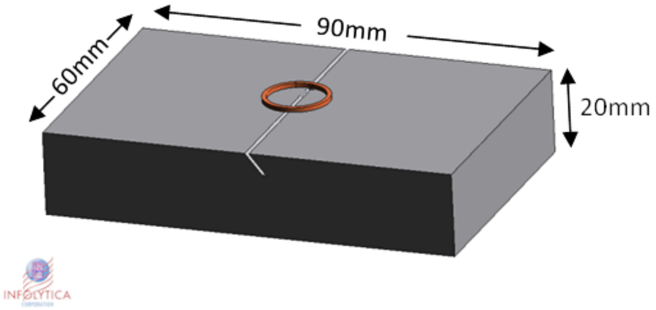

Figure 4.14: 3-D model of the coil and the aluminium sample

FEM simulations for the 3-D visualisation of magnetic field are conducted in transient mode. It is expected that the extracted features from the simulations can help in building the inverse model for defect identification from the acquired magnetic field mapping. They are also intended to facilitate decisions on the sensor selection and the practicability for eddy current imaging through magnetic field mapping and visualisation for defect characterisation by PEC.

Figure 4.15 shows the visualisation (3-D and top view) of a magnetic field distribution for an unflawed sample, as measured along the z-axis of the coil at the steady state region of the transient, i.e. 1 ms, with a coil lift-off of 0.5mm. The visualisations shown are an absolute value of the magnetic field distribution. It can be seen that the magnetic field emanating from the coil shows a distribution which corresponds to the shape of the coil itself. The region near the coil shows a high magnitude of field which decreases abruptly with distance from the coil. This shows that the magnetic field intensity is a function of the radius of the coil. In running the simulation, due to limitations in the computer used, the 3-D mesh assigned to the model was rather coarse, which meant that the magnetic field distribution immediately beneath the coil was not smooth. As a result, an interpolation function has been used to smooth the absolute value of magnetic field distribution at the coil region. Theoretically, the maximum value of magnetic field outside the coil is a lot smaller than the magnetic field maximum value inside it, due to the fact that the flux lines are loose outside the coil. However, the difference vanishes due to the interpolation function used, which mitigates any abrupt fluctuations within the profile of magnetic field distribution over the coil.

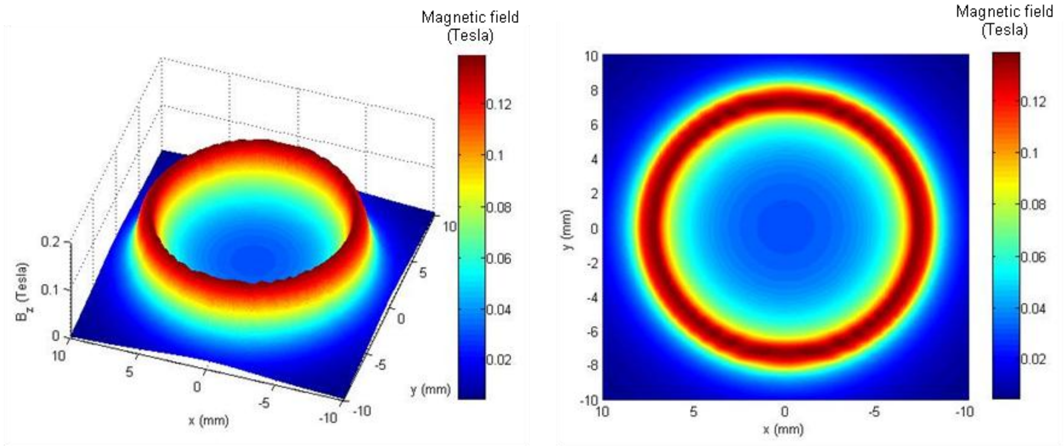

a) b)

Figure 4.15: Magnetic field visualisation acquired at 1ms from an unflawed aluminium sample measured along the z-axis of the coil at lift-off distance of 0.5mm; a) shows a 3-D visualisation and b) a top view visualisation

The magnitude of change in the magnetic field distribution from an unflawed to a flawed sample is relatively small. To visualise the change of the field with the change of the defect angle, the visualisation is made by taking the difference between the magnetic field distribution of a flawed sample and that of an unflawed sample. In the visualisation construction of the differential magnetic field, data acquisitions are performed on two different models; one for the sample with a flaw and the other for the unflawed sample. The differential magnetic field visualisations for all the angular defects can be mathematically defined as follows:

$$\Delta B_{Zm} = B_{Zm} - B_{Zref} \tag{4.2}$$

where B_{Zm} is the magnetic field for a sample with a flaw, B_{Zref} is the magnetic field for an unflawed sample and m represents the defects with angle m = 0°, 10°, 20°, ….., N°.

4.2.2 3D visualisation and feature extraction

4.2.2.1 Mapping analysis

Magnetic field distributions from defects with different angles are simulated and the 3-D visualisation of the fields are mapped and analysed for defect characterisation. Simulations of angular defects are made with defect angles of 0°, 10°, 20°, 30° and 40°. In the simulations, the lift-off between the coil and sample is set at 0.5mm. Data acquisitions for the visualisations are made at 1ms for every angular defect. The objective here is to visualise the change of the magnetic field distribution profile with defect angle. Figures 4.16a) to 4.16e) show the visualisation (top view) of the differential magnetic field with angular defects from 0° to 40° respectively. The dotted line superimposed in the figures represents the central position of the coil.

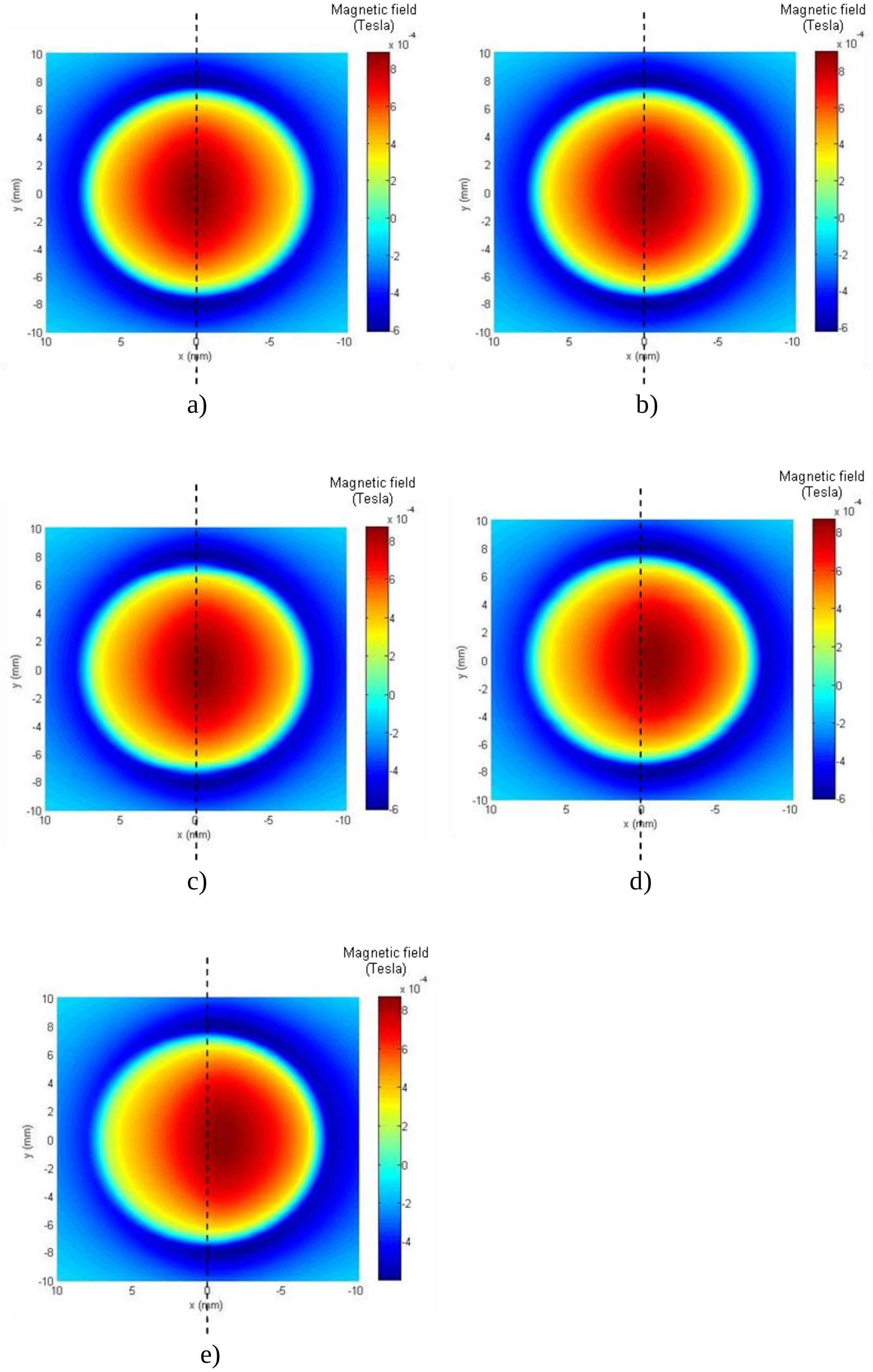

a)

b)

c)

d)

e)

Figures 4.16: Simulated differential magnetic field visualisation at 1ms acquired from the aluminium sample (lift-off = 0.5mm) for (a) 0° angular defect (b) 10° angular defect (c) 20° angular defect (d) 30° angular defect and (e) 40° angular defect (The dotted line represents the central position of the coil)

As can be seen from the maps shown in the figures, the peak of the distribution for every angular defect is shifted towards the right, which shows the defect angle direction inside the sample. Analysing the visualisation results obtained, it is found that the peak of the magnetic field distribution of the angular defects will be shifted according to the angle of the defect as it increases from 0° to 40°. This demonstrates that the shifting of the peak distribution can be used as one of the features for quantitative estimation of angular defects. Through the analysis, a correlation between the peak distribution shift and the defect angle can be made, as shown in Figure 4.17b. This can be developed as a potential feature for angular defect characterisation.

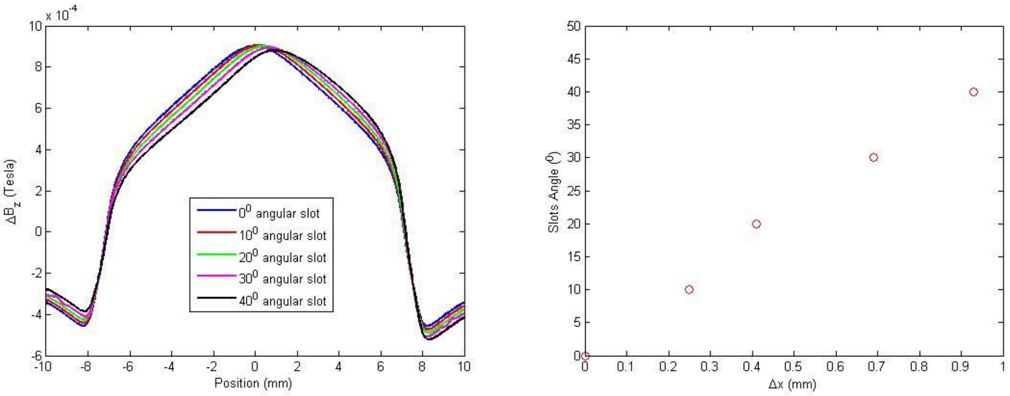

a) b)

Figure 4.17: a) Differential magnetic field distribution against angular defects; b) correlation between the peak distribution shift and the defect's angle

4.2.2.2 Temporal analysis

Angular defects will exhibit different kinds of responses as the eddy current interacts with their geometry. The change of magnetic field distribution for an angular defect is analysed in more detail by analysing the temporal responses of the magnetic field distribution. Figures 4.18 show the visualisation (top view) of the differential magnetic field in the region of the transient response rise time before it reaches a steady state, for the 30° angular defect at 0.04ms, 0.08ms, 0.12ms and 0.16ms The dotted line superimposed in the figures represents the peak (amplitude) of the distribution for the 30° angular defect.

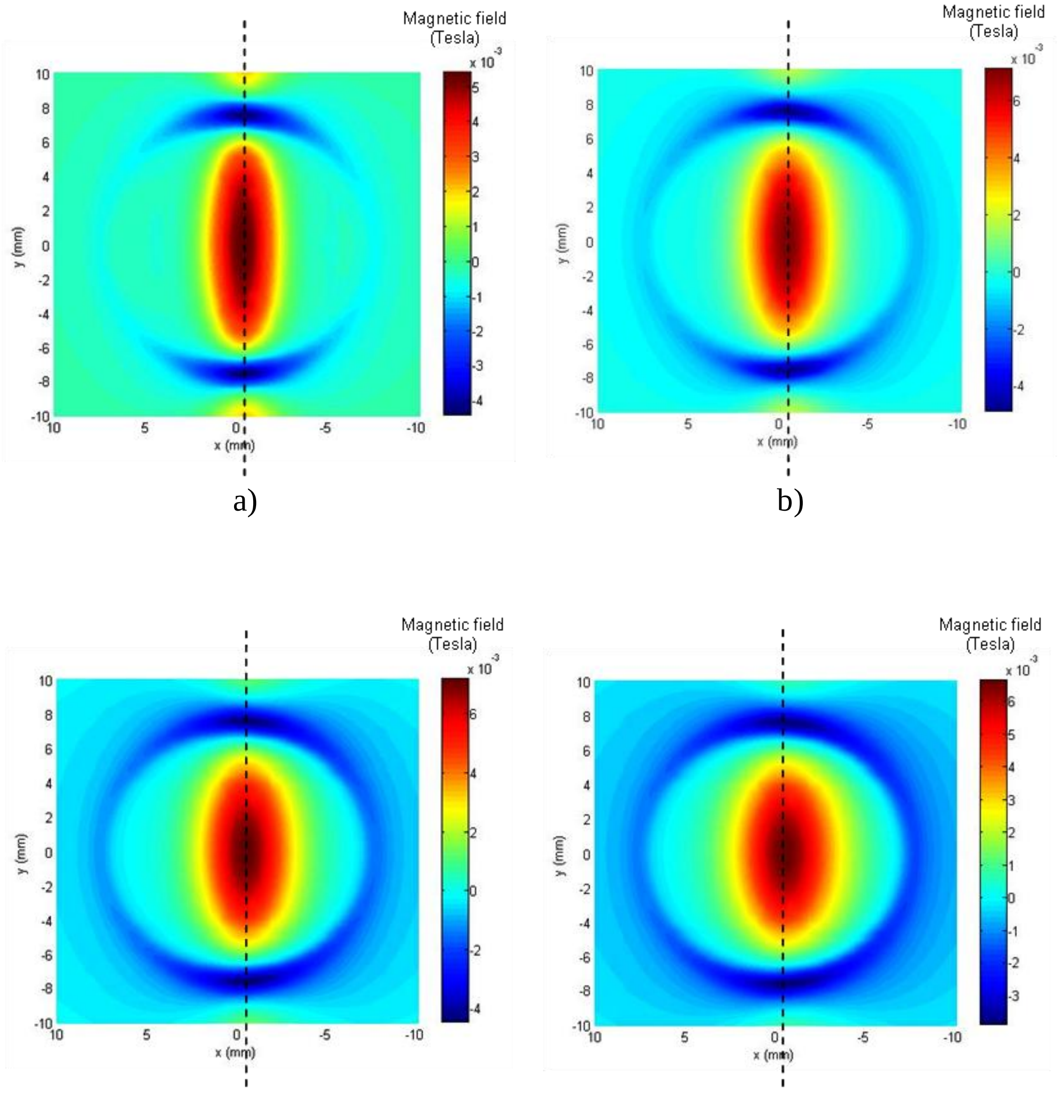

a) b)

c) d)

Figures 4.18: Simulated differential magnetic field visualisation of a 30° angular defect from an aluminium sample at (a) 0.04ms (b) 0.08ms (c) 0.12ms and (d) 0.16ms (The dotted lines represents the peak (amplitude) of the distribution which corresponds to a 30° angular defect)

The magnetic field mapping shown in Figures 4.18 shows how the magnetic field profiles varies with time. As explained in the previous section, the position or the shift of the peak of the magnetic field distribution from the central position of the coil represents the angle of the defect. The results for the 30° angular defect indicate that the position of the peak distribution remains the same, as shown by the dotted line superimposed in the above figures. In the early stage of the transient responses, 0.04ms, it can be seen from the mapping that the magnetic field exhibits a symmetric distribution which corresponds to the opening of the defect. As time increases, the width of the differential magnetic field distribution becomes wider and asymmetric as an effect of the interaction between the eddy current and the 30° angular defect, as the eddy current penetrates deeper inside the sample. The difference in width, Δx of the peak distributions is measured at the half maximum of the linescan amplitude as shown in Figure 4.19. Figure 4.20 shows the change in the width of the peak distribution in temporal response. The data in the figure are fitted by the curve fitting tools in Matlab.

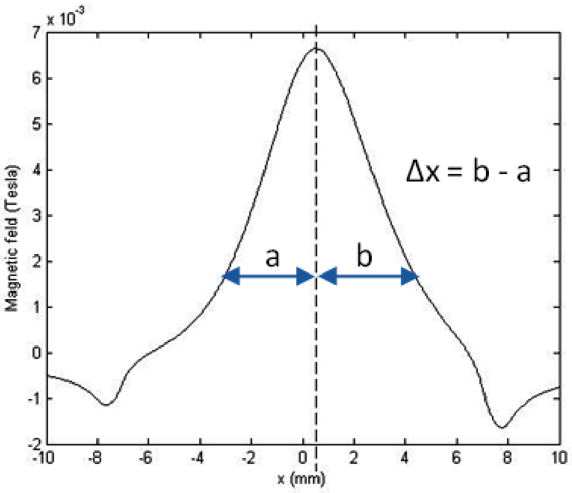

Figure 4.19: The change in width, Δx, of the distribution measured at the half maximum of the linescan amplitude

From Figure 4.20, it can be seen that with this temporal response feature, information on the defect geometry can be obtained at the earlier stages (0.04ms, 0.08ms, 0.12ms and 0.16ms) of the transient responses and used for defect quantification. With the information gathered from the mapping analysis (section 4.2.2.1) for angle discrimination, the temporal analysis will provide additional information for the characterisation of a particular defect, on the length of the defect extension inside the sample.

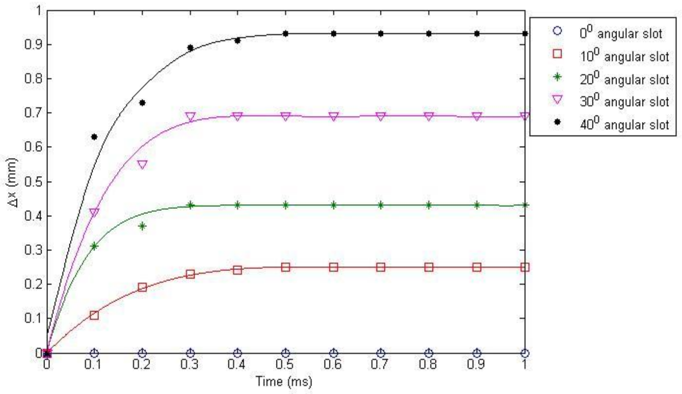

Figure 4.20: The change in width of the peak magnetic field for the angular defects in temporal response

4.3 Practicality for the implementation of visualisation and mapping by PEC

The investigation provided by numerical modelling and simulation in this chapter has assisted the PEC capabilities for angular defect characterisation through the visualisation and mapping of magnetic field distribution. With the advantage of a better penetration (due to frequency components within the pulse excitation), its potential for characterisation of angular defects via features extracted from the mapping analysis and temporal analysis has been identified. Those features can be extracted by the technique of visualisation and mapping of magnetic field distribution. Based on the results presented, one important drawback for the implementation of the mapping by PEC lies with the fact that the shift of the distribution and the change in width of the peak distribution are showing very small changes (< 1mm). In practical applications of the PEC technique, magnetic sensor arrays will be employed for the visualisation and mapping. Commercially available magnetic sensors in the market having a small physical size (packaging size), such as GMR and Hall magnetic sensors, are >3mm [101, 133].

For the purpose of visualisation and mapping through an array configuration, the available size of the magnetic sensors leads to a low spatial resolution in the experimental application. In order to utilise the features extracted for defect characterisation, relatively high spatial resolution is needed to detect the changes presented by those features. Apart from the high cost imposed in constructing sensor arrays, their use implies that the sensing configuration will be rigid, as in the magnetic camera [134] to be used in eddy current imaging for defect characterisation. This limitation on flexibility becomes problematic when inspecting components with uneven or complex surfaces. The use of a sensor array can also cause electrical interference, which results in distortion of measured magnetic field and degradation in the signal-to-noise ratio (SNR), especially for low level signals. Thus, real-time magnetic field visualisation and mapping becomes unfeasible, since scanning will be required which results in low inspection efficiency. These factors: 1) spatial resolution; 2) high cost of construction; 3) rigidity of the array configuration; 4) interference; and 5) low inspection efficiency, limit the practicality of implementing magnetic field mapping by PEC.

4.4 Summary

The capabilities of the PEC testing technique for the characterisation of angular defects, based on a modelled visualisation and an experimental mapping of magnetic field distribution, has been investigated for defects at different depths within a specimen component. Initially, different pulse widths in the excitation waveform were investigated in system simulations using MagNet (see section 4.1.1). The predicted transient responses (see Section 4.1.2) were confirmed by experimental results (see Section 4.1.3), both suggesting that for defects which were close to the specimen surface, shorter pulse widths were appropriate but for defects at deeper levels, wider pulse widths should be chosen. A pulse width of 1ms was used in the investigation of angular defects, so that the penetration of generated eddy currents would cover the depth to which the angular defect extends.

The results of angular defect characterisation by numerical simulations showed that angular defect characterisation can be made through extracted features of the magnetic field mapping. Through the mapping and temporal analyses of those features, geometrical information on the angular defects was obtained. The features: 1) shift in the peak magnetic field distribution and 2) width of the peak magnetic field distribution; have shown the potential to provide information on angle discrimination and defect quantification. However, due to the relatively high spatial resolution required to extract the features from the magnetic field mapping (and other contributing factors discussed in section 4.3), the practical infeasibility of the mapping limits the visualisation and mapping technique to be implemented by PEC. An alternative technique, to visualise and map the resulting eddy current interaction with defects, has to be adopted to overcome this limitation. The selected technique for angular defect characterisation will be introduced in the next chapter.

Chapter 5

Modelling and evaluation of PEC thermography

An alternative technique used for the task of characterisation of defects, which combines eddy current heating and thermography, is now examined. PEC thermography (also known as induction thermography [135], tone burst eddy current thermography [136], and thermo-inductive [137] inspection) with eddy current excitation is an integrative NDE method which allows the imaging of eddy current distribution with the ability to inspect for defects over relatively large areas with high spatial resolution, rather than using magnetic sensor arrays. The resultant surface heat distribution from direct eddy current heating and diffused heat can be easily obtained with a thermal camera but for quantitative defect characterisation, techniques for the determination of heating mechanisms around a particular defect are required. Consequently, modelling of PEC thermography is essential if the relationship between the applied field and the resultant temperature distribution is to be fully understood. The modelling can also provide guidance on the experimental specification and configuration for the PEC thermography technique.

In this chapter, numerical modelling and experimental studies are applied to investigate the PEC thermography underlying phenomena on simple discontinuity defects, including transient eddy current distribution and heating distribution. Through the graphic visualisation provided by the numerical simulations, the effect of defects on the heating distribution can be explained and thus provides the means for evaluating the proposed PEC thermography capabilities (through eddy current heating) for defect characterisation by the visualisation and mapping technique.

The FEM is initially employed to simulate the thermographic behaviour of the two fundamental defects, the slot and the notch, to provide an understanding of the heating mechanism surrounding a particular defect. Through the simulation results, visualisation of the heat distribution inside the investigated sample can be obtained and the heating pattern which is observed at the sample surface can be properly explained. This section of work is inspired by the work by Vrana et al. [135], which described the effects of slots and notches in a finite body on the current density distribution via numerical and analytical models. Two fundamental defect models shown to cause a characteristic heat distribution were introduced in their work but experimental implications and discussion of the contributing factors were limited.

The work in this chapter is then extended to look at a defect, which combines the characteristics of the two fundamental defects (slot and notch), in a mild steel sample using both simulation and an experimental approach. In the investigation, the distance between the induction coil and the end of the defect is varied and the results are related back to the fundamental defect types in order to explain the heat distribution. This fundamental understanding of eddy current distribution and heating propagation through thermal visualisation and mapping will aid in the understanding and the development of feature extraction and pattern recognition via the PEC thermography technique. Through the investigations, the PEC thermography technique can be evaluated for quantitative analysis of induction heating images and defect characterisation.

5.1 Fundamental defect models

A great deal of work has been done on the modeling of defects in NDE. Analytical models have been developed for defects with elliptical shape, since realistic defects are more elliptical in nature. For example, Lewis et al. [138] had worked on analytical models for ACFM of semi-elliptical defect in a metal to model the resulting magnetic fields above the surface. Through their work, magnetic field strengths have been estimated for various combinations of defect length, depth and sensor lift-off.

With the intention of understanding the fundamental behaviour of eddy current heating and heating diffusion, Vrana et al. [135] have reported an analytical model for the calculation of the current distribution with FEM, with the coil simplified to a linear wire in the simulation model. Two fundamental defect models are introduced:

1. the slot - finite in length but extending completely through the sample.
2. the notch - infinite in length, but finite in depth;

A defect can be described by its specific length and its depth profile. Therefore, depending on the nature of the defect, the induced eddy currents flow either around the defect tips or beneath the defect. To model this behaviour, it is therefore best to look at these two alternatives individually, i.e. a model needs to be designed for the case where the current only flows around the defect and another model for the case where the current only flows beneath the defect to complete its path. The introduction of the slot and notch defects provides the means to demonstrate the variation in the induced eddy current distribution which is dependent on the geometry of the defect within the inspected sample. Through the acquired knowledge of the heating mechanism around a particular defect, the resultant thermographic images can be explained in relation to the encountered defect and its geometrical parameters.

Using the PEC thermography technique, the inspected sample is heated up rapidly by an inductively generated current flow. PEC thermography uses brief 20-200 ms pulses to heat the sample to a moderately defined overall temperature. In this process, the presence of defects will disturb the flow of the induced eddy currents and this affects the temperature distribution on the sample surface, so that the defect can be visualised using a suitable thermographic camera. Figure 5.1 shows the illustration of the eddy current distribution for the two fundamental defects described in the previous work [135]. The introduction of a slot in the eddy current path results in a diversion of the eddy currents around the tips of the slot, causing an increase in eddy current density and resultant hot spots at the slot tips coupled with a cooler area at the centre of the slot, where eddy current density is decreased. The introduction of a notch in the eddy current path results in a diversion of the eddy current flow underneath the notch, resulting in an increase in eddy current density and a resulting hot spot at the edges and underneath the notch.

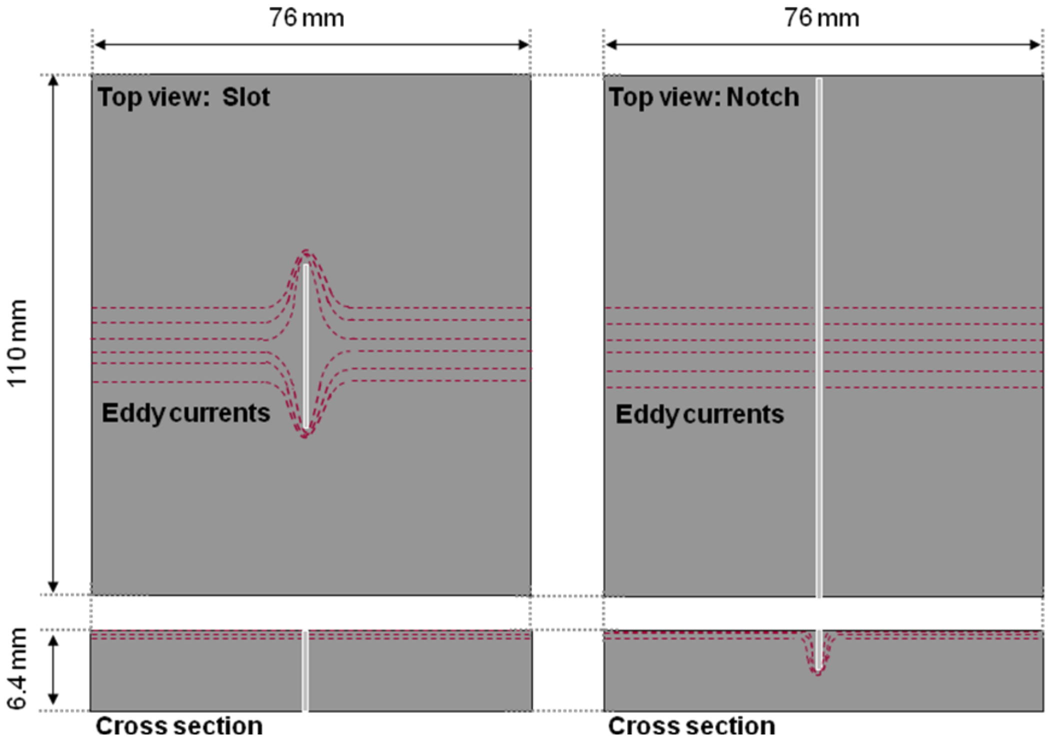

a) b)

Figure 5.1: Illustration of the eddy current with the presence of a) slot, and b) notch (Drawings are not to scale)

The following section (Section 5.1.1) will investigates the competition between these two modes and its dependence on system geometry. It builds on previous work [135] to look at the transient temperature change in various positions around a defect, the correlation between induction heating and eddy current distribution and the relationship between coil position and defect. The work provides a step towards quantitative defect characterisation through analysis of the transient change in temperature at various surface positions with respect to the defect.

5.1.1 FEM modelling and simulation results for the fundamental defect models

The slot and notch defects for the simulation are modelled in a steel block measuring 110 x 76 x 6.4mm. A square coil with an OD of 100 mm and ID of 87.3 mm is used in the simulation. The coil is modelled on the experimental coil used in the tests in section 5.2.2 and is positioned perpendicular to the sample (simulating a line inductor) and at 90° to the defect. The current input for the coil is set at 350 A. The lift-off (the distance between the coil and the sample) of the coil from the sample is positioned at 0.5mm.

The lift-off is set to remain constant in all simulation models to avoid lift-off effect. As described in [135], the induced current density on the sample surface will follow a Lorentzian shape, with its maximum directly under the inductor. The full width half maximum of this distribution is twice the distance between the inductor and the surface of the sample, while the maximum amplitude decreases with increasing distance from the surface. As the sensitivity of detection depends on the interaction between the induced eddy current and defects, the lift-off should be minimised and constant in order to get reliable and consistent results.

The simulations are implemented in COMSOL via the multiphysics application which combines the application mode for induction currents and general heat transfer to provide the solution for PEC thermography and is modelled in 3-D. In the FEM method of analysis, the model is divided into a mesh of tetrahedral-shaped elements. In order to get good accuracy from the 3-D simulation, a fine mesh is generated within the region of interest. The mesh quality is enhanced around the defect area and the region where the direction or magnitude of the magnetic field is changing rapidly, which is at the area between the coil and the sample. The initial temperature of all the domains in the model is set to 19.85^{o}C. The 3-D induction heating linear solver is employed to calculate the eddy current and temperature distribution and is solved using the time-stepping method. Details and descriptions of the modelling and simulation setup for PEC thermography conducted in COMSOL are presented in Appendix B. Table 5.1 summarises the electrical and thermal parameters for steel used in the simulations. These electrical and thermal parameter values for steel are given in COMSOL material library which is a framework for a number of extensible databases with properties for a broad collection of physical, elastic, electromagnetic, fluid, piezoelectric and thermal properties of materials as well as heat transfer coefficients.

Table 5.1: Electrical and thermal parameters for steel provided by COMSOL

Parameters	Steel
Electrical conductivity, δ $[S/m]$	4.0319 × 10^6
Relative permeability	100
Temperature coefficient $[K^{-1}]$	12.3 × 10^{-6}
Density, d $[kg/m^3]$	7850
Heat capacity, C_P $[J/kg.K]$	475
Thermal conductivity, k $[W/m.k]$	44.5
Thermal Diffusivity, α $(=k/dC_P)$ $[m^2/s]$	1.1934 × 10^{-5}

Figure 5.2 shows the simulation results for the slot and notch after 200ms of heating. The eddy current flow for the two defects is visualised by the streamline plot (Figure 5.2a). In the presence of a defect, eddy currents will divert to complete their closed loop path, which leaves a unique eddy current distribution based on the defect geometry that can provide useful information about a defect. Comparison of the streamline plots for the slot and the notch shows that the presence of the through slot causes an obvious diversion of the eddy currents around the tip of the slot. The diversion of the current flow for the notch is less obvious, but some disturbance in the eddy current distribution surrounding the notch can be identified. The streamline plots also illustrate the large influence that sample geometry has on eddy current distribution; where the eddy current loops encounter a material edge an area of higher current density is formed, e.g. at the sample edge, under the coil. Thus, defects with the same geometry and orientation, but different positions on the sample under inspection can interact with the induced eddy currents in different ways and cause very different heat distributions.

Figure 5.2b shows the heat distribution for the slot and notch, viewed from the top of the sample for surface heating distribution and as a cross section under the linear coil, directly under the induction coil. It can be seen from the top views that for both samples, there are hotter areas directly under the induction coil, plus a build up of heat at the edges of the samples. In addition to this, the slot exhibits a characteristic heat build up at the tips of the slot and cooler areas either side of the slot. The presence of the notch is not as obvious in the top view, but examination of the cross sectional view shows a clear build up of heat at the edges and under the defect.

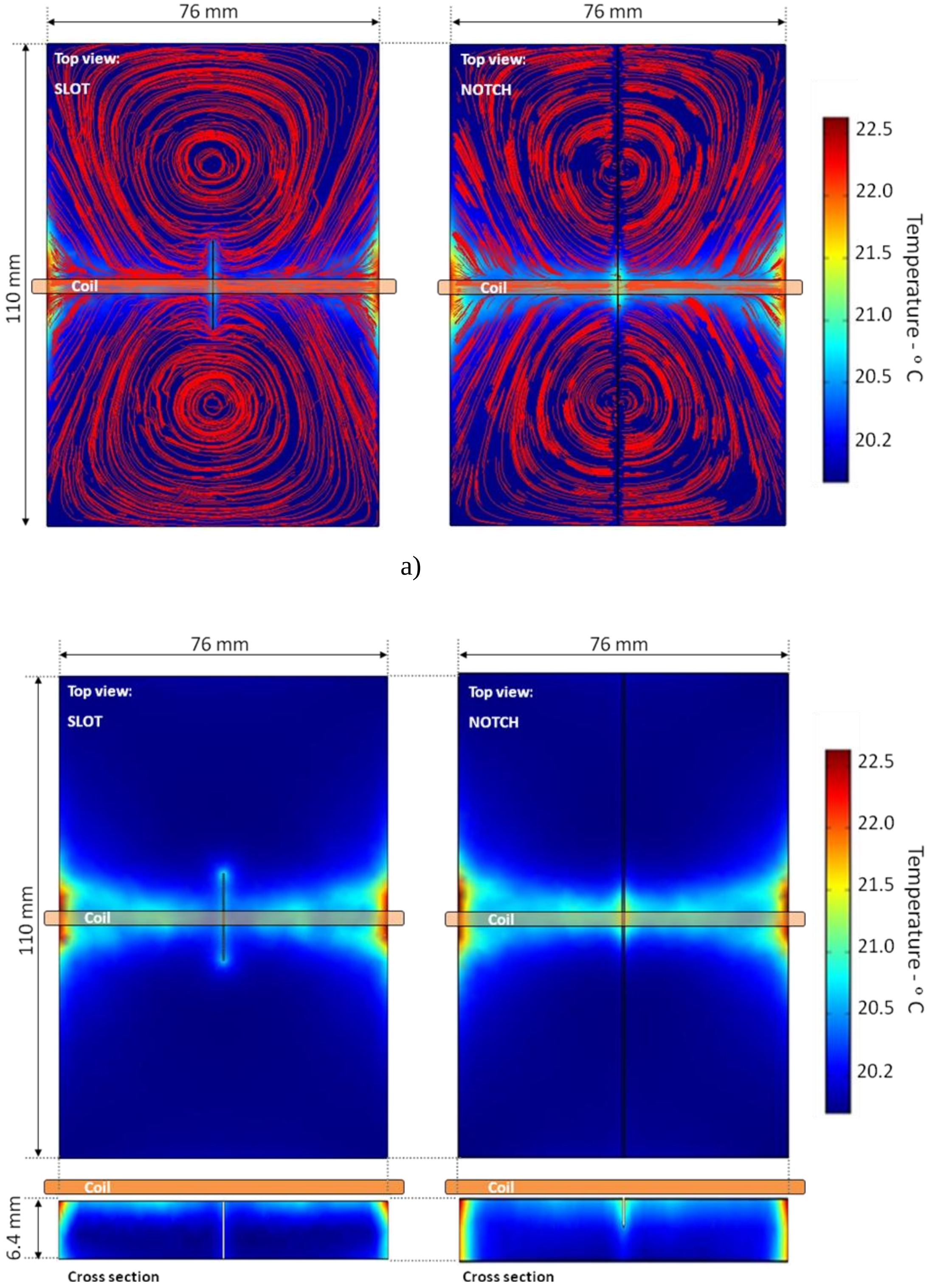

a)

b)

Figure 5.2: Simulation results for steel sample after 200ms of heating of a) eddy current and b) heat distribution for ideal slot and notch. (lift-off = 0.5mm)

Based on the simulation results, the theoretical eddy current distributions and resultant heating patterns for the two fundamental types of defect are shown in Figure 5.3. These results are consistent with Vrana's [135] work, where different heat distributions exist around a slot and a notch. The introduction of a slot into the eddy current path results in its diversion around the tips of the slot causing an increase in eddy current density and resultant hot spots at the slot tips, coupled with a relatively cooler area at the centre of the slot where eddy current density is decreased. The introduction of a notch into the eddy current path results in its diversion underneath the notch, resulting in an increase in eddy current density at the edges of the notch and a slight increase of temperature at the bottom of the notch. The heat distribution for real world defects can be understood by considering the contributions from the two modes; heating at the tips of defects due to lateral diversion of eddy currents and heating at the edges of the defect due to medial diversion of eddy currents.

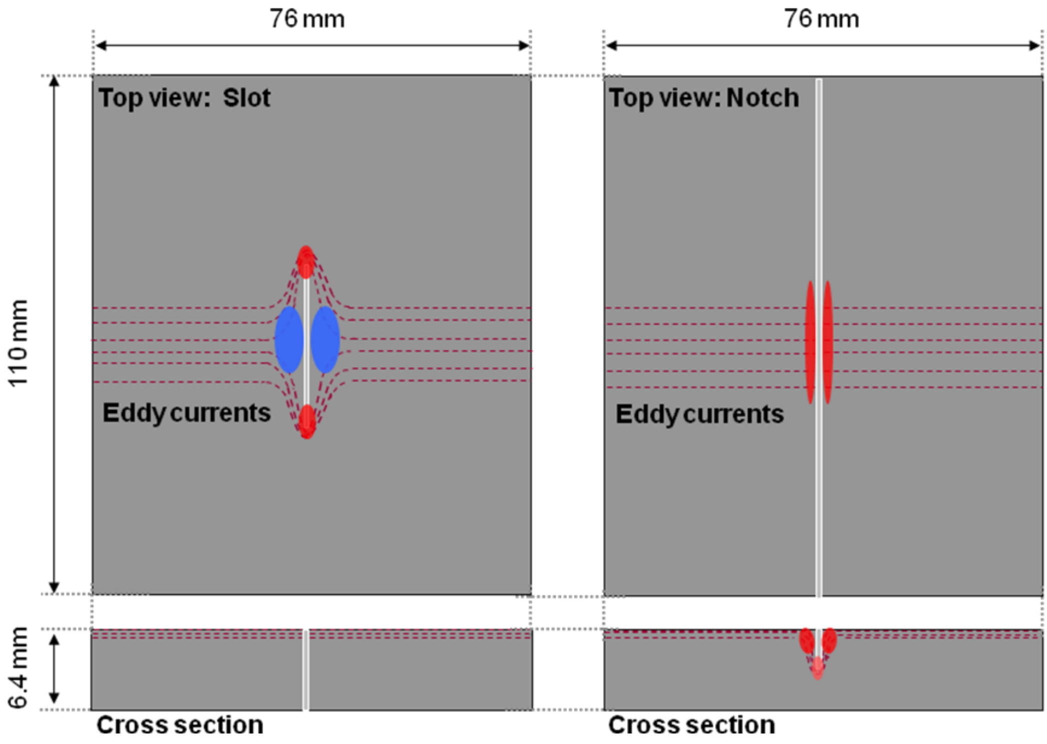

a) b)

Figure 5.3: Schematic of theoretical eddy current distribution and resultant heating patterns for a) slot and b) notch type defects (Drawings are not to scale)

5.2 PEC thermography investigation of mild steel sample

In this section, a mild steel sample containing a rectangular, surface-breaking defect is introduced. A schematic diagram of the investigated sample is shown in Figure 5.4. The sample is chosen to reflect a real world defect situation where combinations of the fundamental defects' influences (shown in Figure 5.3) are in operation; i.e. diversion of the eddy currents around the tips of the slot, which results in hot spots at the tips; and diversion of the eddy current flow underneath the notch, resulting in a hot spot at the bottom of the notch. The work provides a step towards quantitative defect characterisation through analysis of the transient change in temperature at various surface positions due to the presence of a defect.

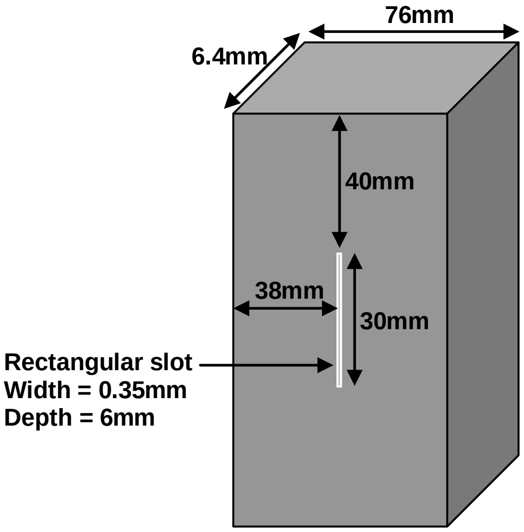

Figure 5.4: Schematic diagram of the mild steel sample containing a rectangular defect (the drawing is not to scale)

The proportional influence of the two types of heating phenomena is analysed by varying the coil position with respect to the tip of the defect. As in the previous investigation, the square coil is positioned normal to the test sample, with the edge of the coil orthogonal to the defect under inspection, simulating a line inductor configuration. The position of the coil is quantified by distance *d* (Figure 5.5), which represents the distance between the top edge of the coil and the tip of the defect. The three data averaging positions, #1 - 3 shown in Figure 5.5, are chosen to represent the development of heating around the defect and are used for analysis of the transient temperature change. For the experimental results, the mean pixel value is chosen to quantify the heating in these positions.

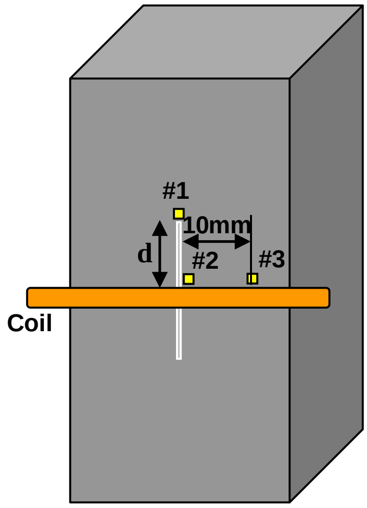

Figure 5.5: Illustration of the coil position (quantified by *d*) and data acquisition positions #1 - 3 for analysis of transient temperature (the drawing is not to scale)

Simulations and experimental investigations are performed in the analysis of the development of heating around the defect as the coil position is varied. The simulations, implemented in COMSOL, are intended to visualise the eddy current and the resulting heating distribution inside the investigated sample. Verification of the results will be provided by comparing the experimental results with the simulations.

5.2.1 PEC thermography system

The system setup of the PEC thermography system consists of an induction heating control box which supplies power to the work head. The work head contains a transformer coupled resonant circuit, including two capacitors and the excitation coil itself. The excitation of the coil is controlled by the function generator which also controls the heating duration of the experiment. The excitation frequency is dictated by the values of the capacitors, the inductance of the coil and the load of the circuit, i.e. the material, volume and proximity of the sample under inspection. A PC which is linked to the IR camera stores the thermal images captured by the camera for subsequent analysis. Figure 5.6 shows the system setup for the PEC thermography system used in the investigations.

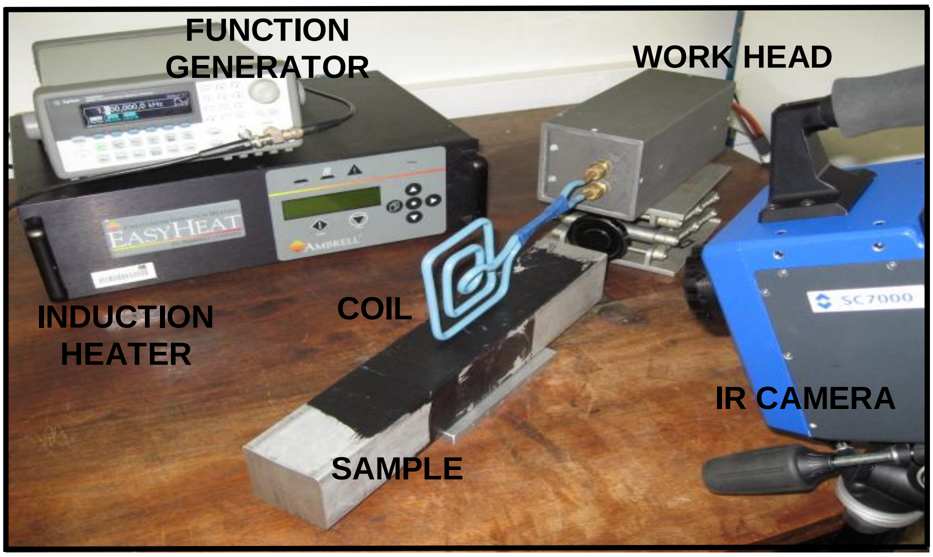

Figure 5.6: System setup for PEC thermography system

The experimental system used in the investigation is constructed around a DeltaTherm 1410 IR camera system and the EasyHeat induction heating system from Cheltenham Induction Heating Ltd. The EasyHeat system has a maximum excitation power of 2.4kW, a maximum current of 400A_{RMS} and excitation frequency range of 150 kHz – 400 kHz. A square coil with an OD of 100 mm and ID of 87.3 mm is used in the tests, positioned perpendicular to the sample (simulating a line inductor to provide localised heating) and at 90° to the defect. The test set-up for the investigation of the mild steel sample is shown in Figure 5.7 below.

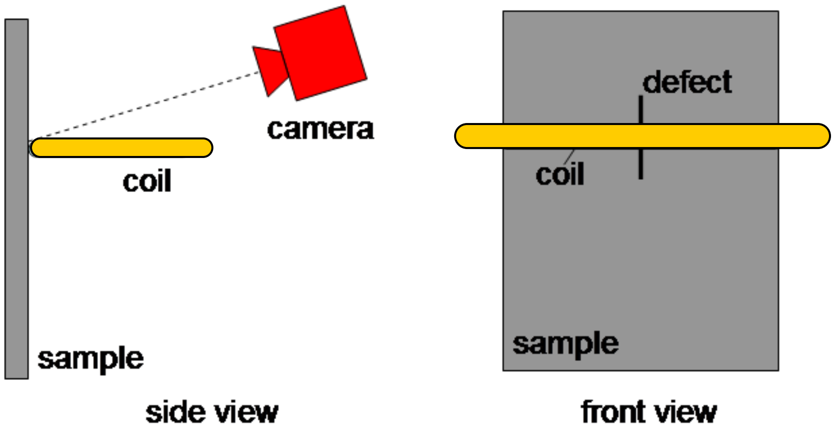

Figure 5.7: Experimental set-up for the investigation of the mild steel sample

A current of 350A_{RMS} is applied to the coil for a maximum of 200ms. The excitation frequency is determined by the resonant frequency of the circuit formed by the coil, the sample and passive components contained in the work head of the EasyHeat system. In these tests the frequency settled at 257 kHz. Images are acquired at a sampling frame rate of 142fps (maximum frame rate of the DeltaTherm 1410 camera) and the acquired image sequences are processed in Matlab.

5.2.2 Simulation results and discussion

Figure 5.8 shows the simulated eddy current and heating distribution along one face of the defect in the mild steel sample. The dotted line in the figure illustrates the position of the defect. It can be seen from figure 5.8b) that throughout the heating period, the eddy current distribution remains fairly static, but the heat distribution changes considerably. In the early stages (10ms), only heat generated at the tip reaches the surface. As the heating period increases to 150ms, heating at the tip of the defect are joined at the surface by a small amount of diffused heat from the bottom of the defect, hence the build up of heat which surrounds the defect. The result shows that a good definition of the defect tip edges can be obtained in the early stage of the heating period, where eddy current heating is dominant and there is less contribution from diffused heat. In figure 5.8c), the coil is positioned near the centre of the defect (*d* = 14mm). The eddy current density is greatest at the edges of the defect and the distribution remains fairly constant throughout the heating time. Heat is generated predominantly at the edges of the defect and there is some contribution of heating from the bottom of the defect diffuses to the surface as the heating time increases.

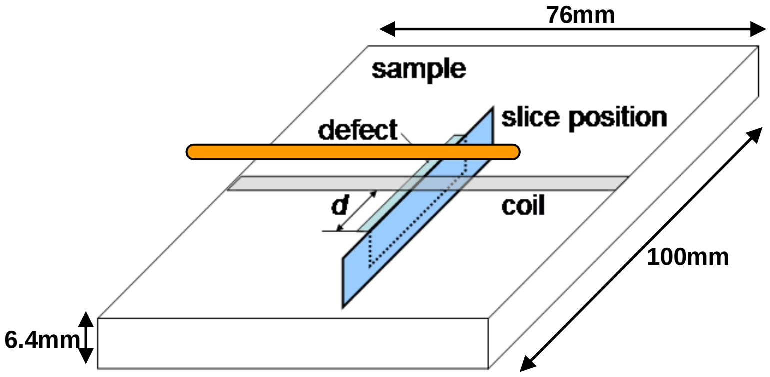

a)

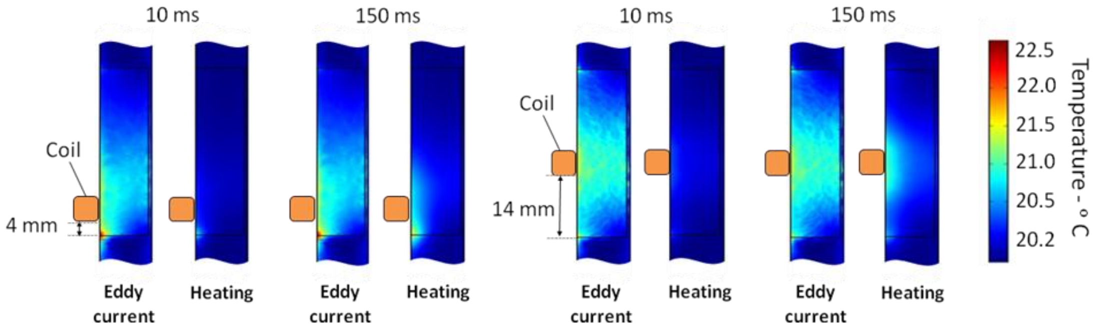

b) c)

Figure 5.8: Slice images of eddy current distribution and heating from simulation model for heating times of 10ms and 150ms for the mild steel sample; a) Slice position, b) Slice images for *d* = 4mm, c) Slice images for *d* = 14mm

5.2.3 Experimental results and comparison with simulation

Figure 5.9 shows the temperature distribution at the sample surface from the PEC thermography experiment conducted on the mild steel sample for *d* = 4mm and *d* = 14mm, after 200ms of heating. From here onwards, the experimental results will be presented by pixel values as an arbitrary representation of the temperature reading. When the inductor is close to the tip of the defect (*d* = 4mm), there is significant eddy current flow around the tip of the defect and the defect behaves predominantly as a slot. When the inductor is close to the middle of the defect (*d* = 14mm), the path of least resistance is around the bottom of the defect and the defect behaves predominantly as a notch. It can be seen from the images that for d = 4mm, the heat distribution conforms to the heating at the tip of the defect. For d = 14mm, the heating is negligible at the tip, but there is significant build up of heat at the sides of the defect, close to the induction coil. These observations confirm the results presented by the numerical simulations in section 5.1.1, where the eddy current follows the path of least resistance which forms the dedicated heating distribution with a particular defect. Through the graphical results provided by the simulations, the heat distribution due to the presence of a defect was observed, and provides support for the experimental results.

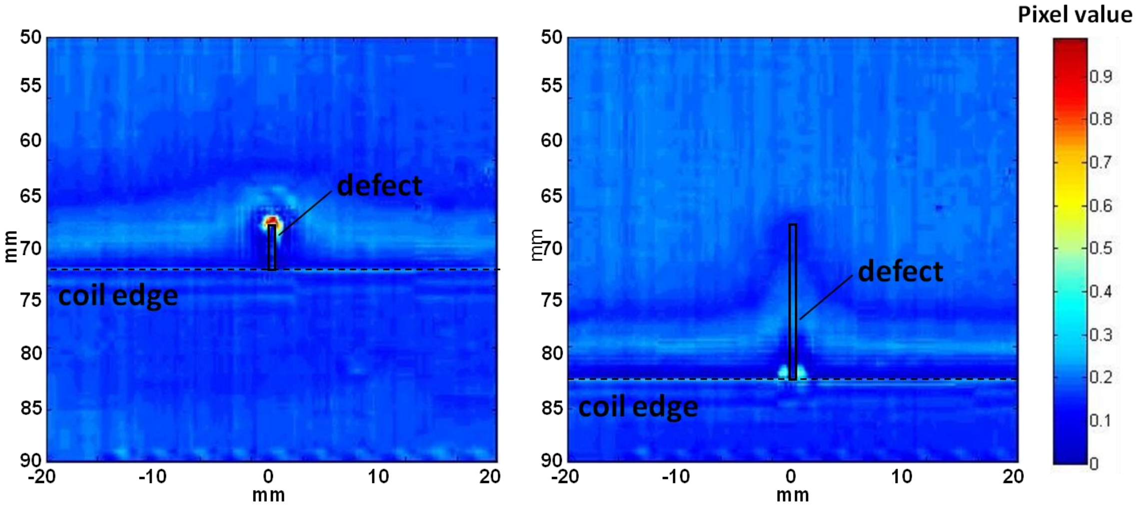

a) b)

Figure 5.9: a) Thermal images from the experiment conducted for the mild steel sample after 200ms of heating for *d* = 4mm, b) Thermal image for *d* = 14mm

Figures 5.10 show the temperature history for the defect, with a heating time of 20ms. A short heating time is chosen for these tests in order to maximise the separation of direct Joule heating and diffused heat; direct heating dominates in the heating period, whereas diffused heat dominates in the cooling period. It is found that 20ms is the shortest heating period which could be recorded at the maximum data acquisition rate of 142fps and that would also induce a reasonable change in temperature.

It can be seen that for d < 6mm, after the heat is switched off at 20ms, the values for positions #1 and #2 (see Figure 5.5) converge at around 40ms, indicating a negligible contribution from heat propagation from deeper in the sample. However, when d >= 6mm, position #2 cools much slower than position #1, so the contribution of subsurface heat propagation to the surface over time is much greater.

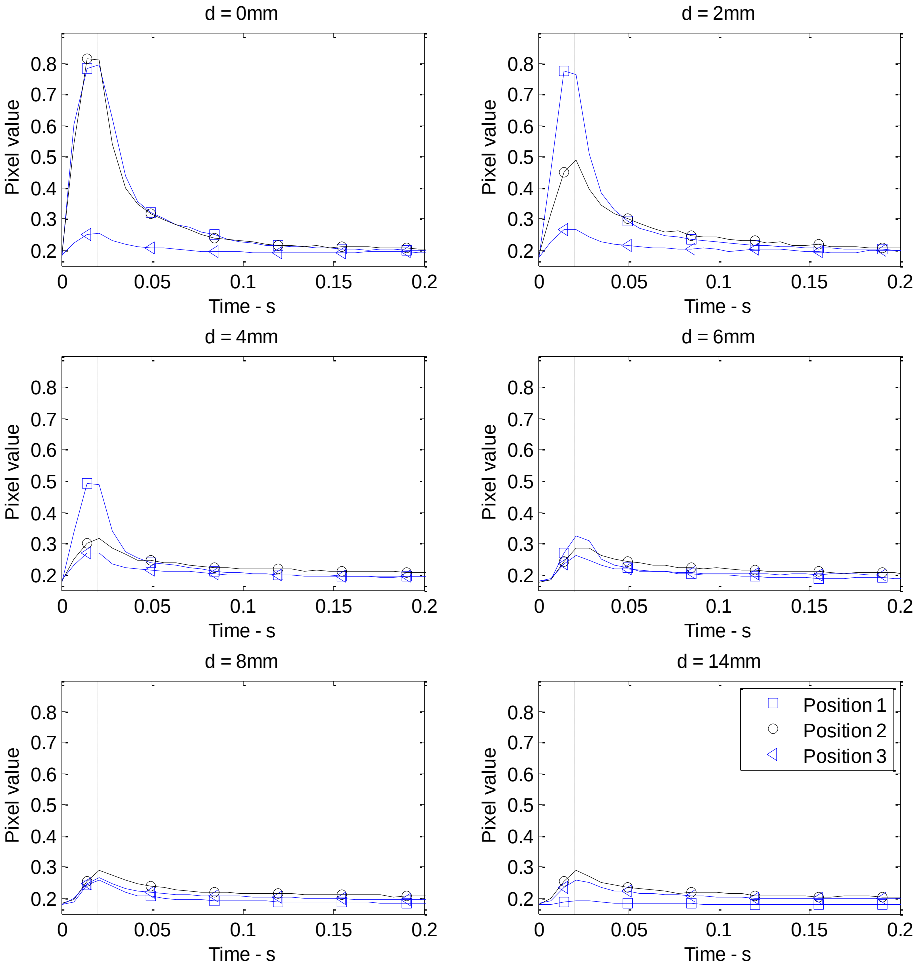

Figure 5.10: Experimental results for 20ms heating time for the mild steel sample, with *d* = 0mm, *d* = 2mm, *d* = 4mm, *d* = 6mm, *d* = 8mm and *d* = 14mm

The experimental results show a good agreement with those of the simulation in terms of how the eddy current will divert itself according to the least resistance path, and the resulting transient temperature change as the coil position is varied. From the results, it is observed that the maximum temperature always occurs at either position #1 or position #2 (see Figure 5.5) which are the distinctive points for describing the defect. Figure 5.11 shows the maximum temperature for positions #1 and #2 over a 20ms heating period for both simulation and experiment.

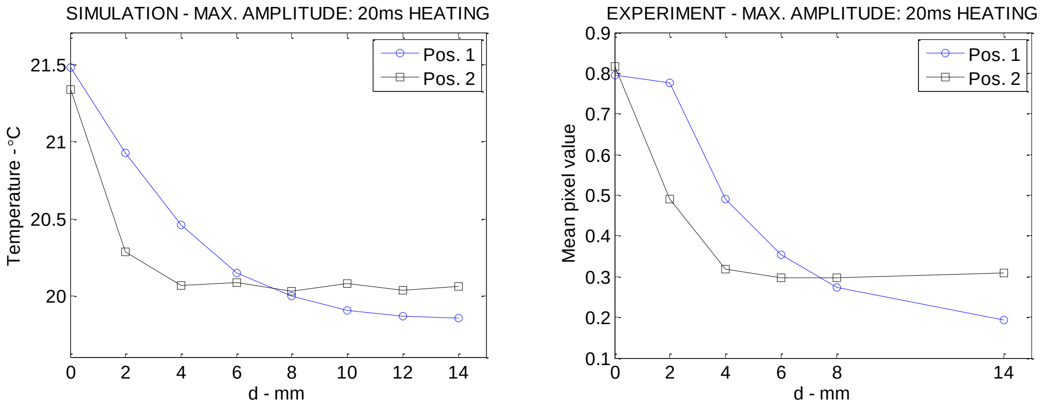

a) b)

Figure 5.11: Maximum temperature over heating period for variation in coil position *d* a) Simulation, and b) Experiment

It can be seen from the plots that heating in position #1 decreases monotonically as the distance between the coil and the tip of the defect (*d*) increases. Although heating for position #2 exhibits an initial decrease, up to around 4mm, the plot levels out as the diffused heat from the bottom of the defect begins to dominate. An interesting feature of the plot is the crossover point between positions #1 and #2, at around *d* = 7.5mm for both the experiment and simulation; the point at which heating at the tip of the defect drops below the level of the diffused heat from the bottom of the defect. Figures 5.10 and 5.11 show that the defect exhibits behaviour which is equivalent to either a slot or notch, or a combination of both, depending on the positional relationship between the coil inductor and the defect, e.g. position and orientation, with the surface transient heating pattern playing a crucial role for defect characterisation.

5.3 Summary

The PEC thermography investigations performed in this chapter illustrate the different heat distribution around two fundamental defect models, a slot and a notch. FEM simulations for PEC thermography were conducted using COMSOL via the multiphysics application. Through the analysis of the simulation results provided in section 5.1.1, the underlying phenomena of temperature distribution due to the presence of a defect inside the investigated sample were visualised. The pattern for a slot is characterised by a diversion of eddy currents around the tip of the defect, with corresponding heating at the tip. The pattern for a notch is characterised by heating at the bottom of the defect and a greater retention of heat in the sample after heating has been removed. The two characteristic heat distributions for the slot and notch are used to explain the heat distribution around a defect with finite depth and finite length. Thus, by consideration of these two simple cases (slot and notch), the mechanism of heating surrounding a defect was understood.

The PEC thermography system was introduced in section 5.2.1 of this chapter. The investigations on the mild steel sample provide the means to evaluate the PEC thermography technique for defect detection and characterisation through the mapping and visualisation of eddy current distribution by the use of an IR camera. The numerical simulation results on the fundamental defects provided an explanation of the heat distribution encountered with the defect in the mild steel sample. Good agreement was shown between the results from the simulation and experiment in terms of heating patterns, supported by the graphic visualisation of the heating mechanism provided by the simulations. It has been shown that the PEC thermography technique has the capability to provide means for defect characterisation through eddy current imaging, where the pattern of heating is dependent on the eddy current distribution resulting from its interaction with a defect. The employment of the IR camera with the PEC thermography technique provided the high spatial resolution required to perform the visualisation and mapping technique for defect characterisation.

Transient analysis performed at distinctive points in the vicinity of the defect has presented the development of heating patterns for the description of the defect. The results presented in section 5.2.3 suggested that defects exhibit behaviour which is equivalent to either a slot or a notch, depending on the positional relationship between the coil inductor and the defect. The experimental results show a good agreement with the simulation in terms of how the eddy currents are diverted according to the least resistance path, and the resulting transient temperature change as the coil position is varied. The results have shown that the PEC thermography technique has the ability to provide quantitative information about a defect through the induction heating images.

Due to the importance of acquiring the temperature history shown in the transient analysis, the specification of the IR camera used to capture this information needs to be taken into consideration. A fast frame rate was identified as a critical factor in camera selection, along with excellent thermal sensitivity. In section 5.2.2, the simulation results show that a good definition of defect edges can be obtained in the early stage of the heating period. This provides the information needed for the mapping of defects for characterisation and quantification. As mentioned in section 5.2.3, 20ms is the shortest heating period that could be captured by DeltaTherm 1410 IR camera system at its maximum data acquisition rate of 142fps. With that consideration, a new IR camera which can provide a faster frame rate is introduced in the experiments with PEC thermography in the following chapters.

The capabilities of PEC thermography for defect characterisation have been demonstrated in this chapter. Chapter 6 presents the investigation of angular defects by PEC thermography. The chapter will discuss the capability of PEC thermography to provide quantitative information on angular defects by the mapping of temperature distribution and extracted features for QNDE of defects.

Chapter 6

PEC thermography QNDE of angular defects

The PEC thermography technique has been evaluated when mapping the eddy current distribution for defect detection and characterisation in the previous chapter. Through numerical simulation and experimental study, the underlying phenomena of PEC thermography on simple fundamental defects have been investigated. Since real defects or cracks rarely have a simple geometrical shape, the influence of a defect's angular characteristics on the thermographic information gathered by the PEC thermography technique must be assessed carefully in order to avoid misinterpretation of the thermographic signal. The capacity to acquire quantitative information about defect geometry, i.e. angle, depth and length, is therefore important for the full description of a defect.

In this chapter, numerical modelling is applied to investigate the thermal behaviour associated with the interaction between induced eddy currents and the angular defects inside an aluminium sample, with experimental work undertaken for verification. Through the simulation of eddy current heating for angular defects having different geometries, i.e. angles, lengths and depths, the eddy currents distributions can be visualised and the resultant temperature distribution can be analysed for feature extraction in the QNDE of angular defects.

6.1 Angular defect investigation via FEM simulations

The simulation models for the PEC thermography investigations of angular defects are built in COMSOL with 3-D coordinates in order to implement a better description of the problem. As shown in Chapter 5, description of the heating phenomena by PEC thermography was displayed by the simulation implemented in COMSOL. The same tetrahedral-shaped mesh element used for the simulation in Chapter 5 is implemented for the angular defects investigations. The mesh quality is enhanced around the defect area and the area between the coil and the sample. The 3-D induction heating linear solver is employed to calculate the eddy current and temperature distributions, and solved using the time-stepping method. Appendix B provides the details of the modelling and simulation setup for PEC thermography conducted in COMSOL.

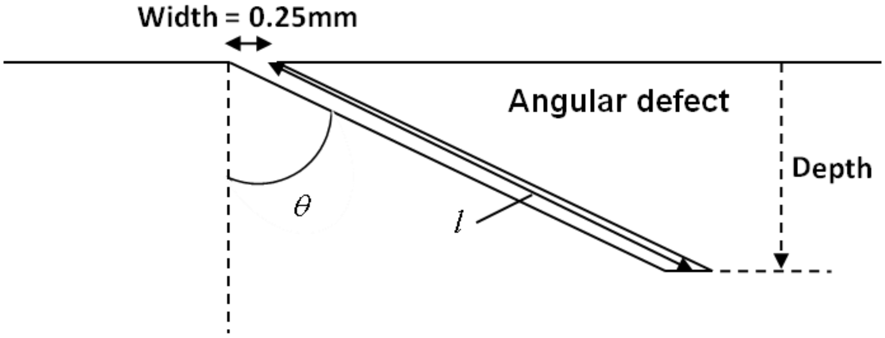

Figure 6.1: Illustration of an angular defect with length l and angle θ inside a sample.

In the investigations, the aluminium sample which contains the angular defects was modelled with dimensions of 80 x 150 x 5mm. The angular defects (see Figure 6.1) have lengths l of 1.5mm, 2.0mm, 2.5mm and 3.0mm and a constant width of 0.25mm with angles θ, of 0º, 22.5º, 45º and 67.5º. The depth to which each angular defect cuts the sample depends on its respective angle and length. The specific angles of the defects are based on the artificial angular defects in the aluminium used in the experimental tests in section 6.3. In the investigations, the width of the notches has no practical influence on the temperature distribution [139], hence the constant width for the angular defects throughout the investigations.

The initial temperature is set at 19.85 ^{0}C for every case of the simulation. The electrical and thermal parameters for aluminium used in the simulations are shown in Table 6.1.

These electrical and thermal parameter values are given in COMSOL material library for aluminium.

Table 6.1: Electrical and thermal parameters for aluminium provided by COMSOL

Parameters	Aluminium
Electrical conductivity, δ $[S/m]$	3.7736×10^7
Relative permeability	1
Temperature coefficient $[K^{-1}]$	2.31×10^{-5}
Density, d $[kg/m^3]$	2700
Heat capacity, C_p $[J/kg.K]$	897
Thermal conductivity, k $[W/m.k]$	237
Thermal Diffusivity, α $(= k/dC_p)$ $[m^2/s]$	9.7857×10^{-5}

The same rectangular coil introduced in Chapter 5 is used in the investigation and is positioned perpendicular to the sample (simulating a line inductor) and at 90° to the angular defect. The current input for the coil is set at 350A with an excitation frequency of 256 kHz. These excitation parameters are chosen to match the experimental set-up. The eddy current penetration of depth with these settings and material parameters is calculated to be 0.162mm, which is smaller than the angular defect depths investigated. However, the heat generated by the induced eddy currents is transferred to the inner part of the material by thermal conduction, which is determined by the thermal diffusivity of the material and not by the penetration depth of the induced currents. This allows interaction with defects, well beyond the skin depth of the induced eddy currents, and so the eddy current penetration depth can be neglected when considering the PEC thermography response to deep defects [48]. The lift-off (the distance between the coil and the sample) is positioned at 0.5mm. As in the previous chapter, this is set to remain constant in all simulation models to avoid lift-off effect.

The numerical simulations undertaken in this work provide a basic understanding of the temperature distribution caused by the interaction of eddy currents with an angular defect inside a sample. Through the simulations, visualisations can be made of induced eddy currents and their interaction with angular defects, which leads to the resulting thermal responses.

6.2 Simulation results and analysis

6.2.1 Eddy current and temperature distribution

Figure 6.2 shows the simulated eddy current distributions in the form of streamline plots, plot simultaneously a slice plot of the heating distribution at the sample surface after 100ms of heating for angular defects of length 2.5mm, with angles of 0º, 22.5º, 45º and 67.5º. The streamline plot represents the contour plot of eddy current density in 3-D (x, y and z-component). A heating period of 100ms is chosen since the thermographic distribution exhibits a reasonable level of thermal contrast in the experimental work on an aluminium sample using this duration. From Figure 6.2a it can be observed that a 0º angular defect exhibits a symmetrical eddy current density distribution on both sides of the defect opening. As the angle of the defect increases in Figure 6.2b to Figure 6.2d, the distribution becomes more asymmetric as the angle increases due to an increase of eddy current density accumulating between the slanted area of the defect and the surface. This flow of eddy current then leads to Joule heating due to the resistance of the metal sample.

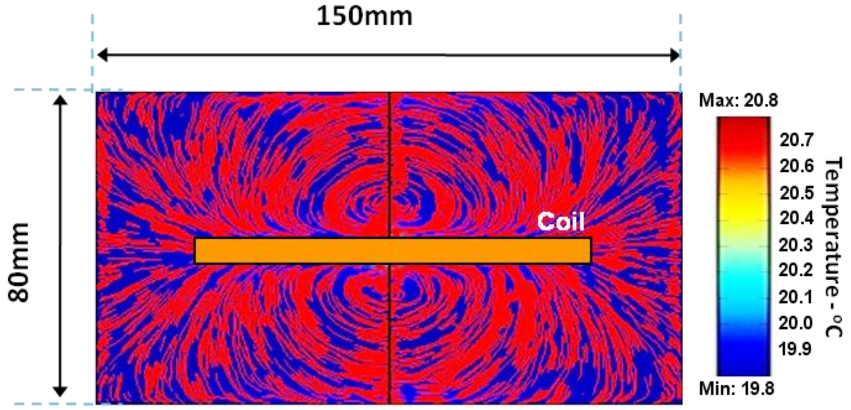

a)

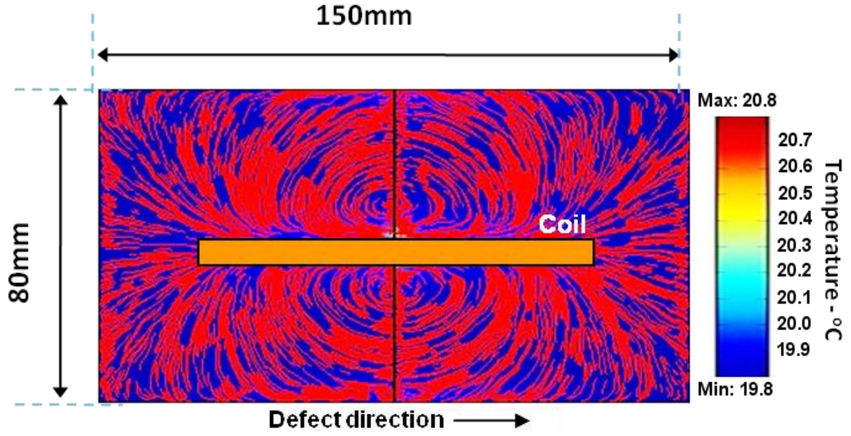

b)

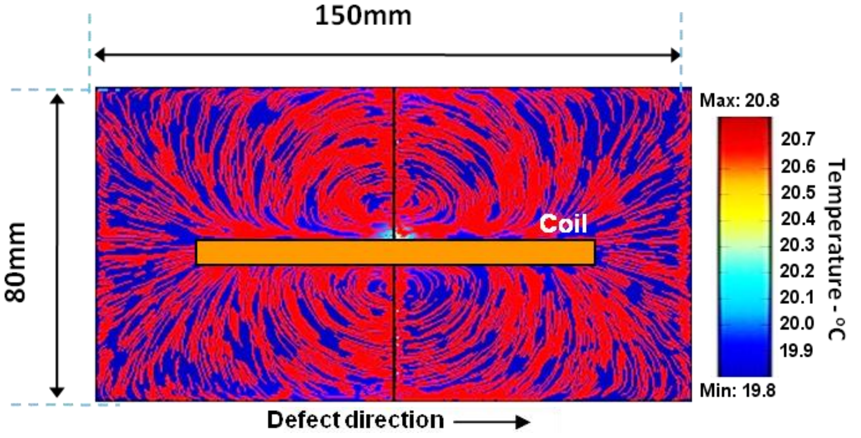

c)

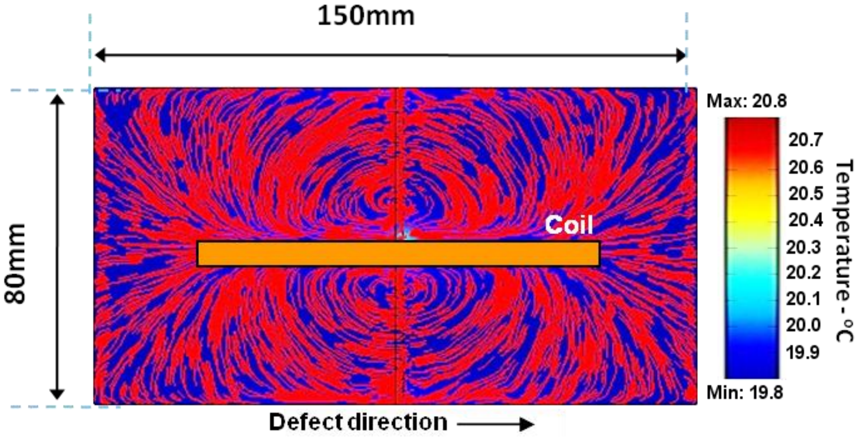

d)

Figure 6.2: Streamline plot of simulated eddy current distribution after 100 ms of heating from top view of the aluminium sample for a) 0° defect, b) 22.5° angular defect, c) 45° angular defect and d) 67.5° angular defect. (Lift-off = 0.5mm)

Figure 6.3 shows the resulting temperature distribution after 100 ms of heating for each of the cases in Figure 6.2. For 0°, which is actually a straight defect, a symmetrical distribution of heating pattern can be observed on either side of the defect. As discussed in Chapter 5, a notch type of defect experience heat generated predominantly at the defect edges. Due to the diversion of the eddy current underneath the notch, heating from the bottom of the defect contributes to the overall heating as it diffuses to the surface as the heating time increases. An angular defect shows a heating distribution which is dominant in the defect direction within the sample. The figures also show that an increase in temperature contrasts with increasing angle. Figure 6.3 illustrates the phenomena; the angle of the defect causes a modification of the eddy current distribution in the sample, leading to a build of eddy current in the corner of the notch. This area experiences increased levels of Joule heating, much greater than would typically be found around a straight defect in the same sample. This can be further explained by Figure 6.4, where it can be seen that for angular defects of greater angle; more heat tends to accumulate within the slanted area between the defect and the sample surface, thus contributing to a higher temperature contrast at the surface of the sample. Since the area is bounded by the defect, the heat is trapped between the defect and the surface and propagates through this bounded area over time.

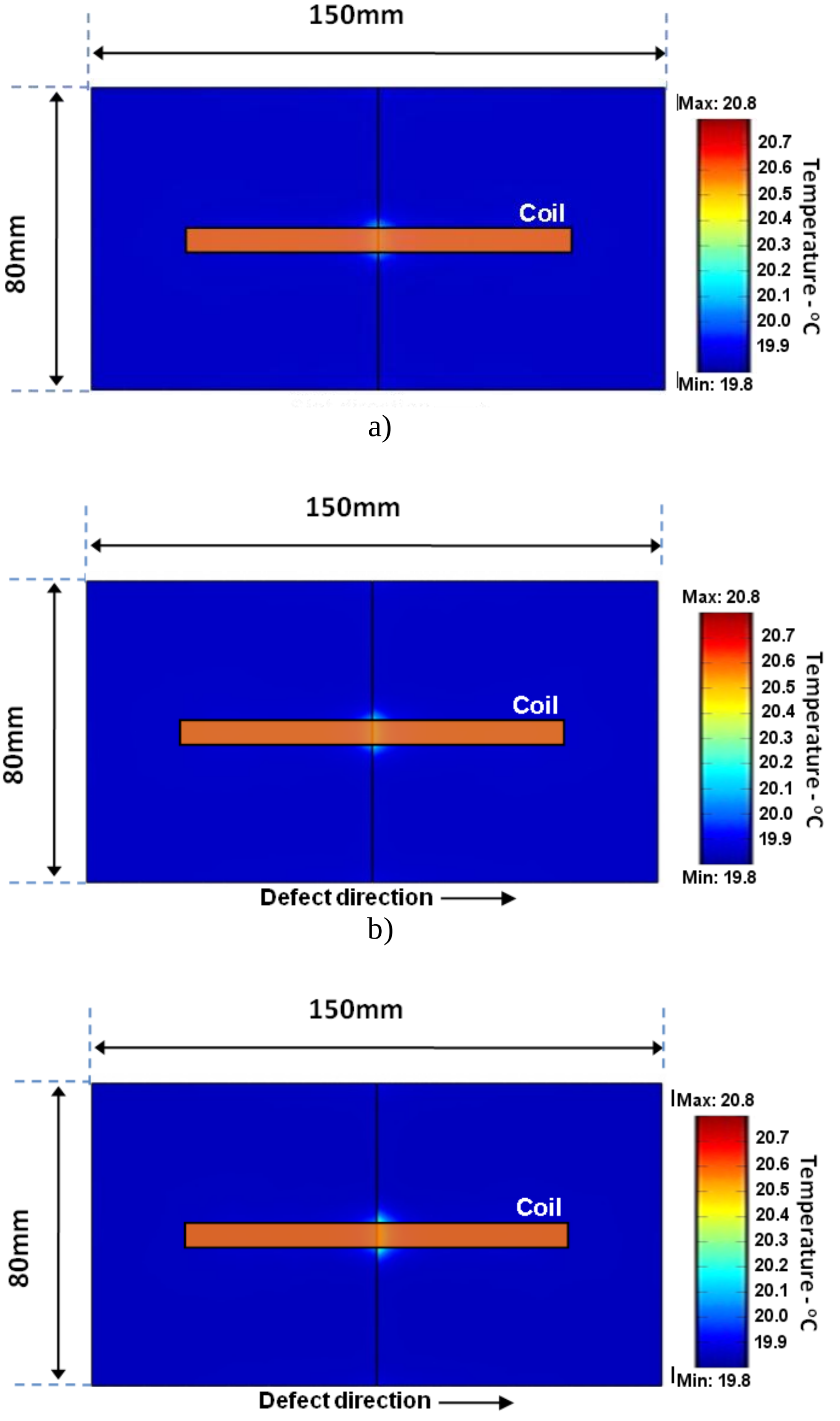

a)

b)

c)

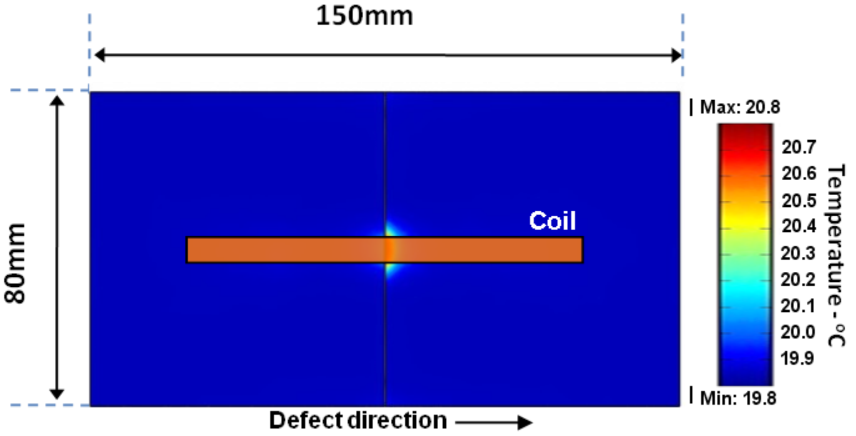

d)

Figure 6.3: Simulated temperature distribution after 100 ms of heating from top view of the aluminium sample for a) 0° defect, b) 22.5° angular defect, c) 45° angular defect and d) 67.5° angular defect. (Lift-off = 0.5mm)

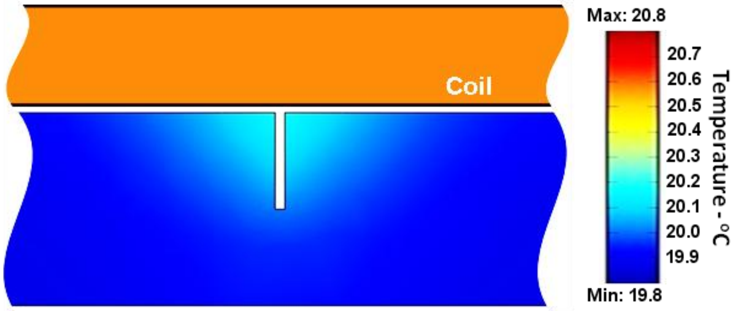

a)

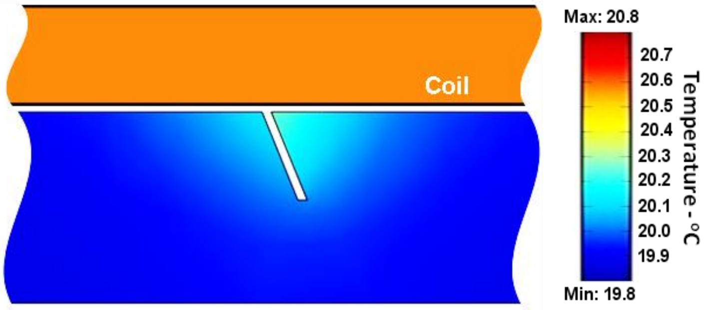

b)

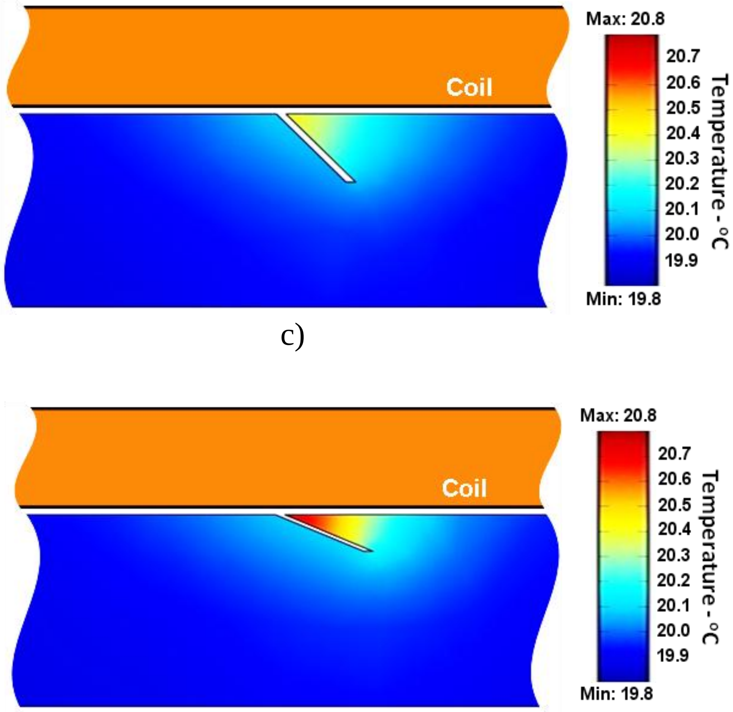

c)

d)

Figure 6.4: Simulated heat distribution after 100ms of heating from cross section view of the aluminium sample for a) 0° defect, b) 22.5° angular defect, c) 45° angular defect and d) 67.5° angular defect. (Lift-off = 0.5mm)

In crack detection by the thermographic technique, it has been known that the deeper the crack is, the greater the thermal contrast displayed at the surface of the sample [139, 140]. However, in the case of angular defects, the thermal contrast and temperature distribution has been shown to be influenced by the angular characteristics of the defects. Since the eddy current heating for angular defects is both angle and depth dependent, the characterisation of the angled defects becomes more complicated. Defects with a wider angle and length (thus depth) trap more heat between defect and the surface, which contributes to higher temperature amplitude measured at the surface.

The heat inside the sample transfers by conduction from warmer to cooler areas, which effectively occurs by diffusion. From equation 3.16 in Chapter 3, the heat flux that flows inside the sample per unit area per unit time can be expressed by Fourier's law of thermal conduction:

$$Q = -k\nabla T \tag{6.1}$$

where Q is the heat source density, k is the thermal conductivity of the material and ∇T is a vector quantity of temperature gradient with distance.

For PEC thermography, Q is the heat source density induced by eddy current per unit time in a unit volume. For angular defects, the dominant heat source is local to the corner of the area enclosed by the defect itself and the surface of the material (see Figure 6.4d); eddy currents are confined to an increasingly small area as they approach the corner, leading to an increase in eddy current density and a resultant increase in heating. As this heating effect is comparatively large, the heating of the surrounding area can be seen as low compared to a point source in the corner.

Since the temperature gradient, ∇T, is directly proportional to the heat source induced by the eddy current, defects having the same angle (thus the same heat source density, Q), but different lengths always display the same ∇T in the area enclosed between the shorter defect and the sample surface. This characteristic of ∇T is depicted as a constant feature of the temperature profile for the thermographic signal acquired at the sample surface for defects with the same angle.

6.2.2 Feature extraction

In order to analyse the temperature profiles of angular defects, temperature linescans taken at the edge of the induction coil (see Figure 6.5) at the sample surface are acquired for 22.5º, 33.75º, 45º, 56.25º and 67.5º angular defects after 100ms of heating for different defect lengths of 1.5 mm, 2.0 mm, 2.5 mm and 3.0 mm. Two more angles (33.75º and 56.25º) are added in the investigation for the analysis of the features from the acquired temperature profiles. The linescan is taken at that specific location to observe the change of temperature distribution on both sides of the defect opening.

From the linescan results shown in Figure 6.6, it can be observed that this constant feature of the temperature gradient for defects having the same angle is depicted as the slope of the temperature profile at the defects slanting area. Angular defects with a wider angle exhibit a steeper slope. The slope of the temperature profile can be extracted and measured by taking the half maximum of the temperature value of the distribution (refer to Figure 6.7) as the reference point. The slope, SL, is then obtained by measuring the gradient (divide the change in temperature by the change in position) between two temperature points at $\pm 10\%$ of the half maximum reference point as shown in Figure 6.7. Through the analysis of the *SL* feature from the temperature profile, the identification of angle for the investigated defects can then be made.

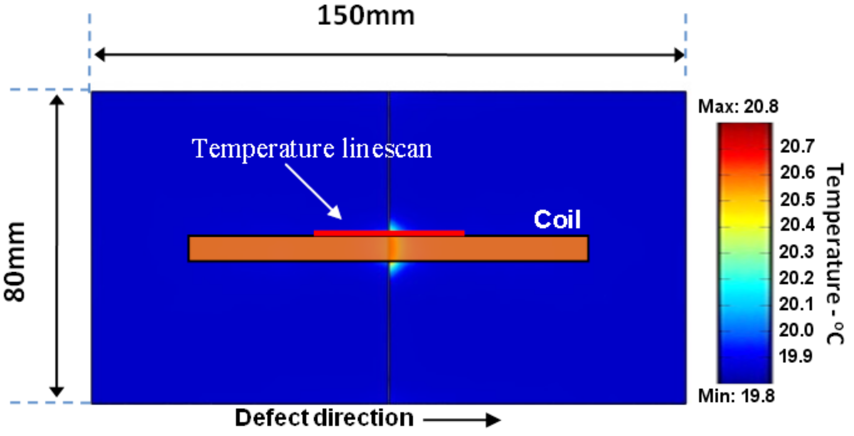

Figure 6.5: Illustration of temperature linescan taken at the sample surface

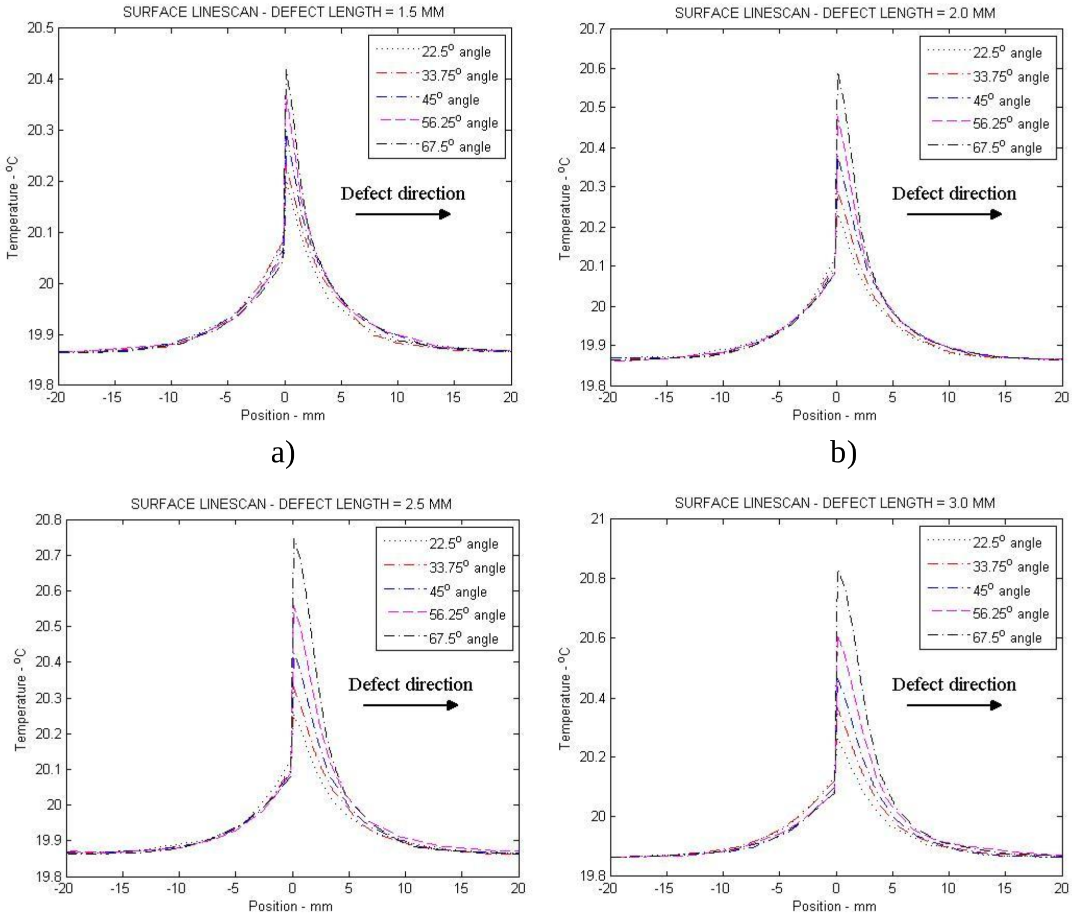

a)

b)

c)

d)

Figure 6.6: Temperature linescan for angular defects of length a) 1.5 mm, b) 2.0 mm, c) 2.5 mm and d) 3.0 mm

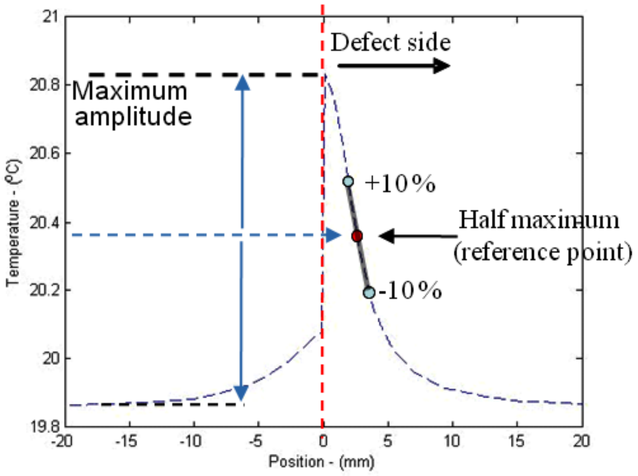

Figure 6.7: Features from the acquired signal from a particular defect to be analysed for characterisation

Figure 6.8 shows the correlation of the SL feature with the geometrical parameters of the defect i.e. angle, length and depth. The error bars in the figures are obtained by taking the difference between the maximum and minimum of the SL values at respectives defect angle and plotted at the mean SL value. From Figure 6.8a, it can be observed that defects with a greater angle of inclination exhibit a steeper SL. The defect length and depth seem to have a minimal effect on the slope of the temperature profile for each angular defect with a different angle. The observation of these results shows that, by using this feature, the angular identification of a defect is independent of other physical parameters of the defect itself, i.e. its length and depth.

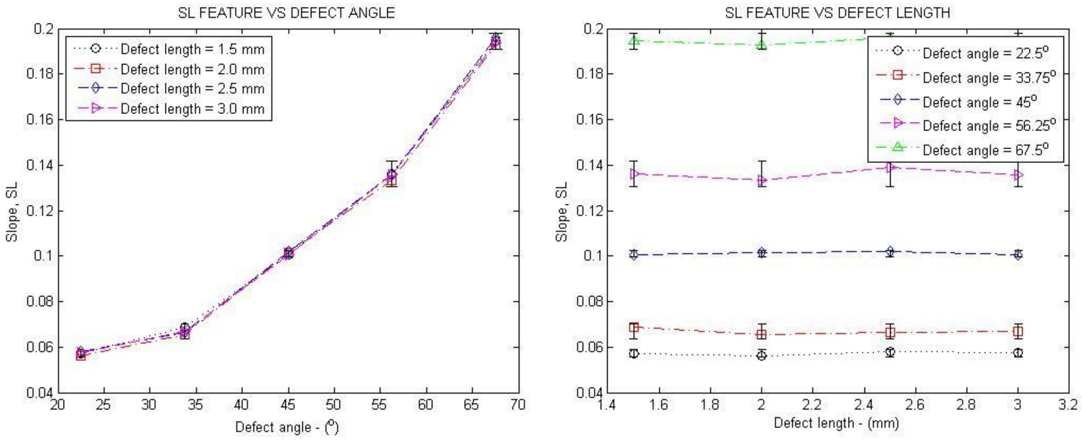

a) b)

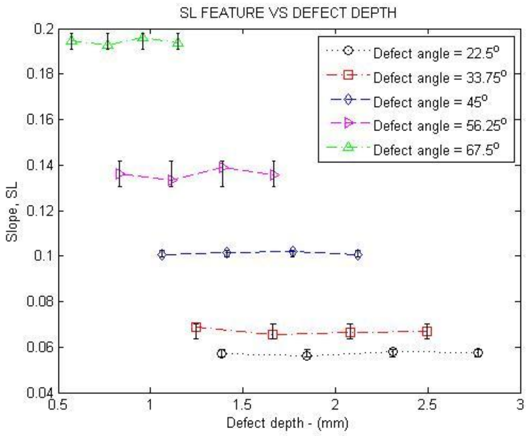

c)

Figure 6.8: Correlation of SL feature with a) defect angle, b) defect length and c) defect depth

The area, A covered by the diffused heat inside the investigated sample depends on the thermal diffusivity of the material and the diffusion time measured at any instant:

$$A = \alpha \times t \tag{6}$$

where A represents the area covered by the diffused heat for a defect with angle θ, α is the thermal diffusivity of the inspected material and t is the diffusion time.

For example, t_h is the heating time chosen to heat the sample, and at this time instant the heat has diffused along a defect with angle θ to a length of l_h from the heat source, covering a slanted area of A_h (see Figure 6.9 below).

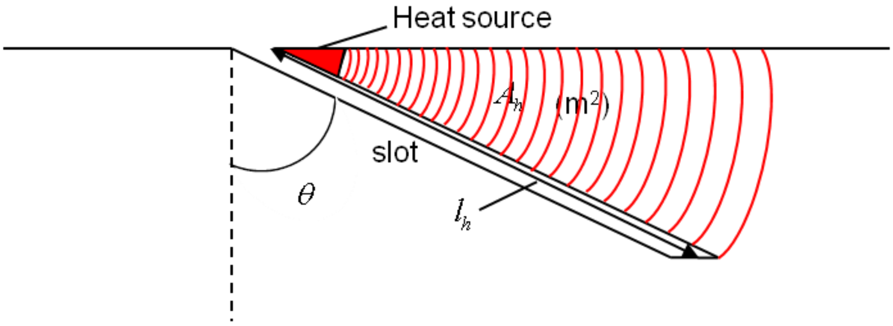

Figure 6.9: Illustration of area covered by heat diffusion at time, $t = t_h$ for angular defects

For any angular defect with length, $l \geq l_h$, the area, (A_h) covered by the diffusion of heat from the heat source remains the same at $t = t_h$. However, in the case of defects (at the same angle) with length, $l < l_h$, the area covered by the diffused heat is larger than A_h , i.e. the diffusion of heat exceeds the area covered by the defect length, and less heat is trapped within the slanted area. If we ensure that the temperature is measured at a time greater than the time required for the heat to fill the area A_h, the difference in heat intensity due to different defect lengths will manifest itself as a difference in the maximum temperature amplitude of the temperature profile for defects having different lengths.

Having identified the angle of the defects using the SL feature, the length/depth of the defect inside the sample can be quantified by making comparisons between angular defects having the same angle using the maximum temperature amplitude, $T_{\max}$ feature. Figure 6.10 shows the temperature linescan for angular defects with different lengths after 100ms of heating.

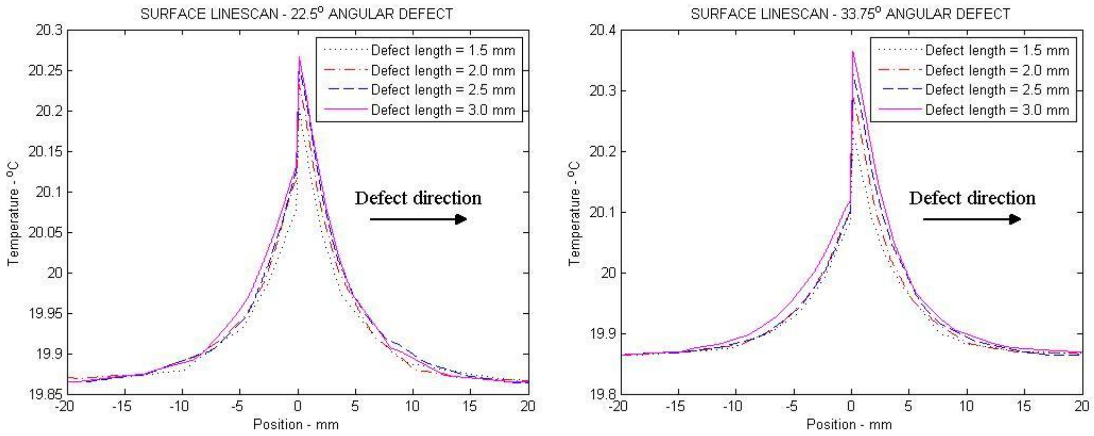

a) b)

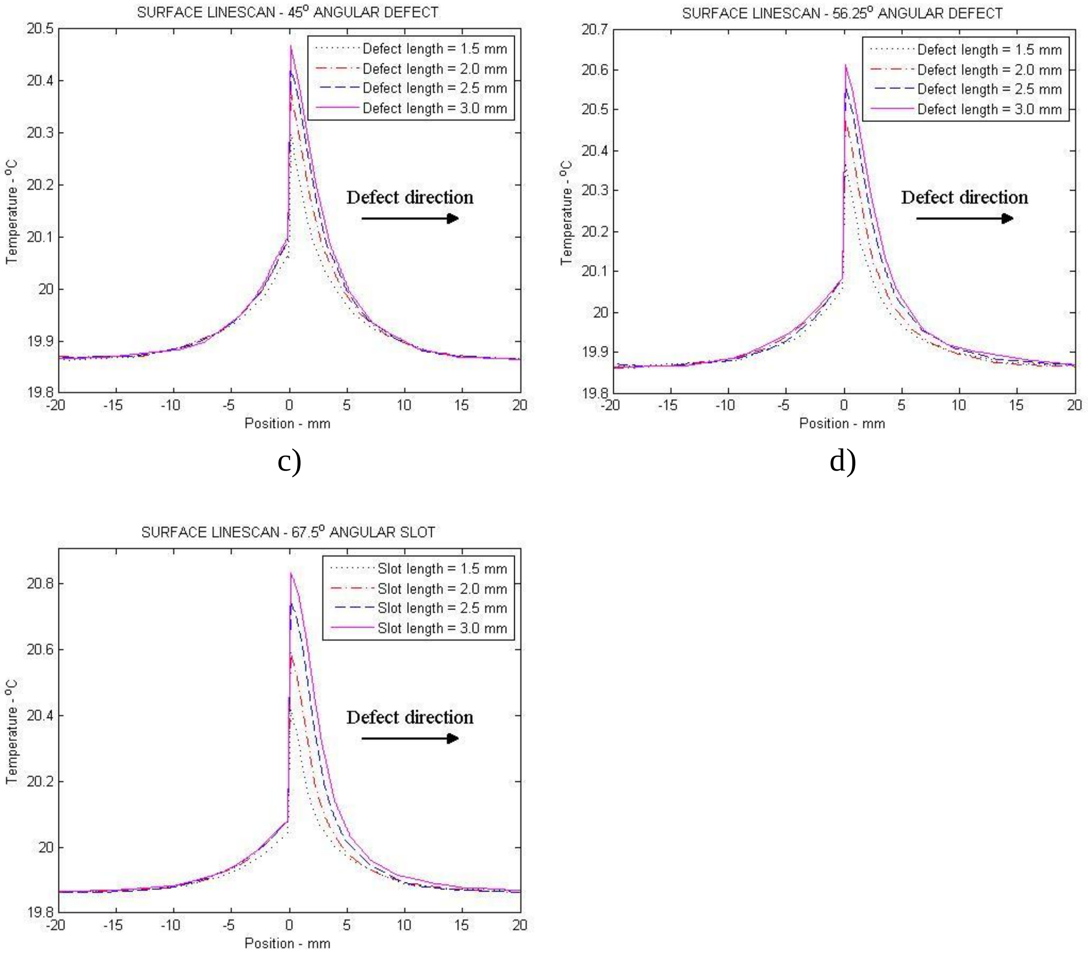

c)

d)

e)

Figure 6.10: Temperature linescan for angular defects having different length at 100ms of heating; a) 22.5 ° angle, b) 45 ° angle and 67.5 ° angle

Figure 6.11 shows the correlation of the $T_{\max}$ feature with the geometrical parameters of the defect, i.e. angle, length and depth. The temperature amplitude is taken after 100ms of heating and the relationship between this feature and the geometrical parameters is then analysed.

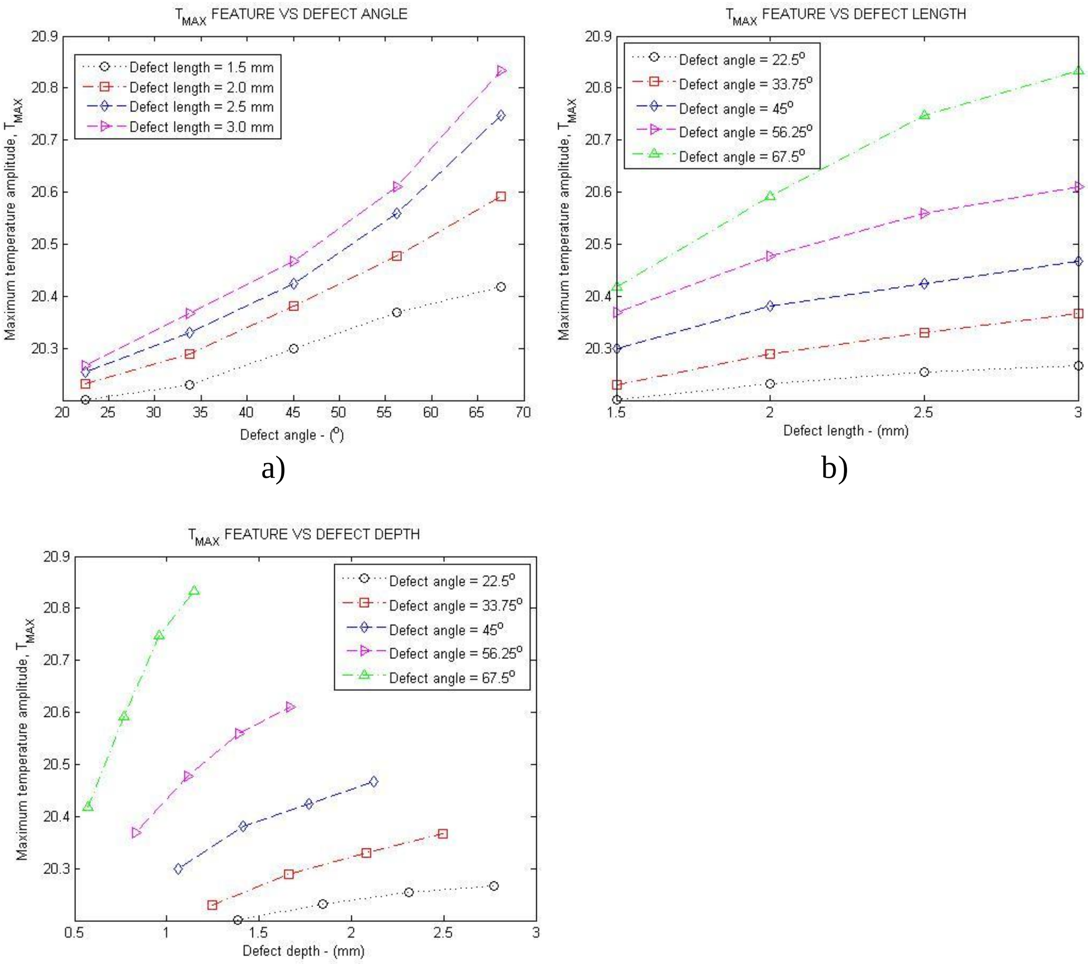

a) b)

c)

Figure 6.11: Correlation of $T_{\max}$ feature with a) defect angle, b) defect length and c) defect depth

Based on Figure 6.11, it can be seen that the maximum amplitude of the surface linescan is affected by these three parameters; angle, defect length and defect depth. A wider angle defect exhibits a higher temperature amplitude at any given defect length compared to a smaller angle defect (Figure 6.11 a). But in terms of depth, the relationship shown is different. For example, at any given defect length, the depths of different angular defects exhibit an inverse relationship towards the temperature amplitude. A 22.5° angular defect, which has a deeper depth at any length compared to a wider angle defect, shows lower temperature amplitude (Figure 6.11c), which is contrary behaviour to that observed in a straight defect, when a deeper defect shows a higher temperature amplitude. These observations show that the identification of the defect angle holds vital information needed for the quantitative evaluation of a defect.

6.3 Experimental verification

The experimental system used in the tests is constructed around a FLIR SC7500 infrared camera system and the EasyHeat induction heating system. A similar PEC thermography system setup to that introduced in Chapter 5 is used for the investigation, consisting of an induction heating control box, a function generator, the work head and the excitation coil (as in Figure 5.6). The square coil is positioned normally to the aluminium sample, with the edge of the coil orthogonal to the defect under inspection, simulating the line inductor or coil configuration in the local area.

A current of 312A RMS is applied to the coil for a maximum of 100ms to replicate the heating period used in the simulations. The excitation frequency is determined by the resonant frequency of the circuit formed by the coil, the sample and passive components contained in the work head of the EasyHeat system. In these tests the frequency settled at 263 kHz. Images are acquired at a sampling frame rate of 383fps and the acquired image sequences are processed in Matlab.

As in the simulations, the experimental work uses an aluminium sample having several artificial angular defects. Three different angular defects, at 22.5º, 45º and 67.5º, having the same depth of d = 5mm, are investigated and analysed. Figure 6.12 shows the grey scale images of the thermographic distribution after 100ms of heating for the different angular defects.

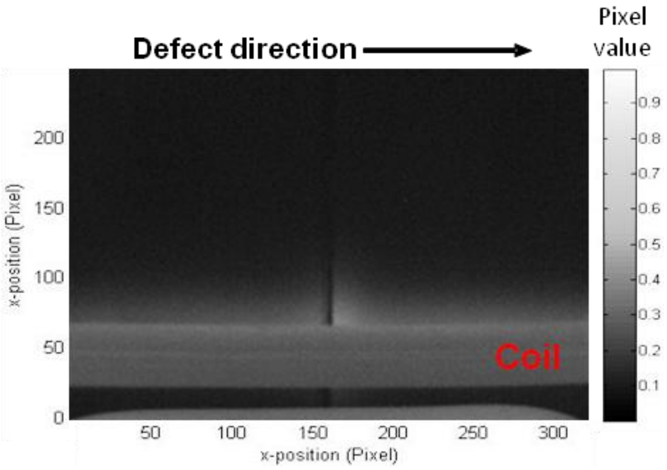

a)

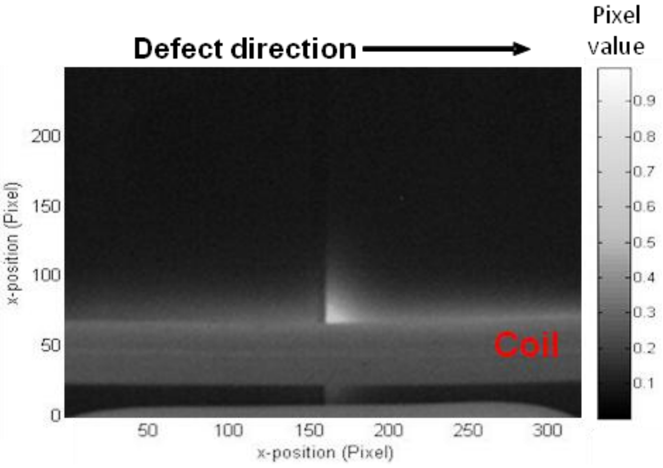

b)

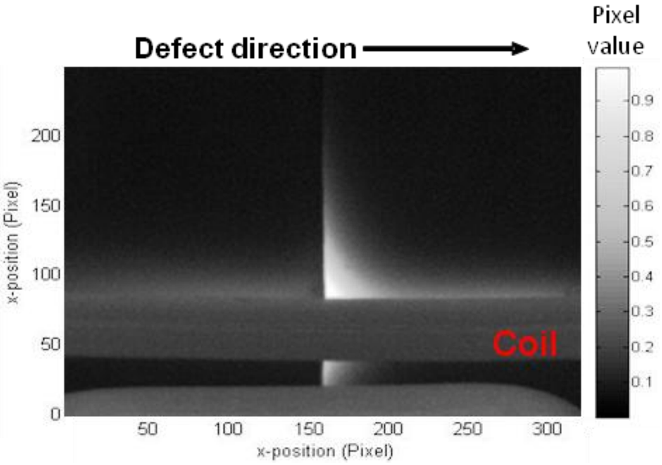

c)

Figure 6.12: Grey scale images of the thermographic distribution after 100ms of heating for a) 22.5° angular defect, b) 45° angular defect and c) 67.5° angular defect

In order to examine the temperature profiles for these angular defects and to compare them with the simulation results, a temperature linescan at the sample surface near the induction coil is acquired for every angular defect after 100ms of heating (Figure 6.13). As mentioned in section 6.2.1, angular defects exhibit an asymmetrical distribution, which gives an early indication of the nature of a defect inside the sample.

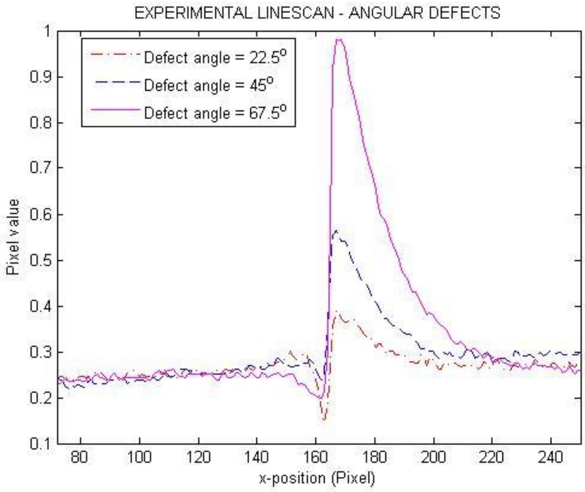

Figure 6.13: Temperature linescan from the experimeny after 100ms of heating for different angular defects

The slope, SL, and maximum temperature amplitude, $T_{\max}$, are obtained from experimental investigations for each of the angular defects. Figure 6.14 shows the experimental results for SL and $T_{\max}$ features based on the geometrical parameters of the investigated angular defects in the experiment. Good agreement can be observed between simulation (Figure 6.8a and Figure 6.11a) and experimental results for the evaluation of defect geometries using the introduced features.

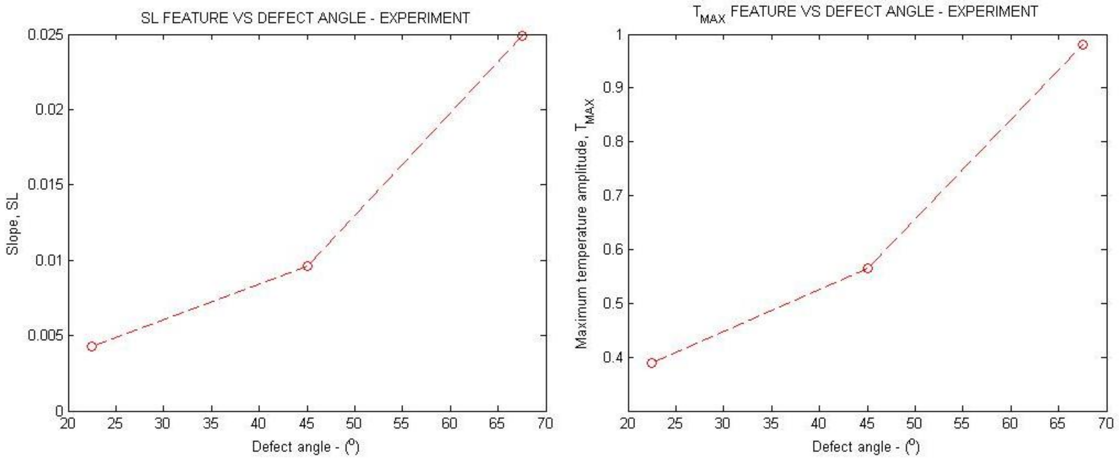

a) b)

Figure 6.14: Experimental results; a) SL for the angular defects and b) $T_{\max}$ for the angular defects

As with the simulation results in the previous section, it can be observed that defects having a wider angle exhibits a steeper inclination of the slope in its linescan distribution (Figure 6.14a). This SL feature can be analysed for estimating the angle of the defect, independent of the defect depth and length inside the sample. Since the maximum temperature amplitude acquired from the thermographic linescan of a defect is affected by three geometrical parameters; angle, length and depth, prior knowledge about whether the defect is propagating heat within a certain area inside the inspected sample is the key to acquiring quantitative information regarding the defect length and depth.

As indicated in Figure 6.14b, angular defects having a wider angle exhibit higher temperature amplitude compared to a narrow angle defect. The maximum temperature amplitude of these defects which have the same depth, d = 5 mm, proves that the angle of the defect has a dominant effect on the overall thermographic distribution and that false evaluation of defect depth/length will occur if investigation of these parameters is made without knowing the angle of the defects. Having determined the angle of a defect, the $T_{\max}$ feature can then be used to quantify the length/depth by comparison of amplitudes between defects having the same angle.

6.4 Summary

This chapter presents modelling and experimental results of PEC thermography investigations on angular defects. FEM numerical modelling is applied to investigate the thermal behaviour associated with angular defects as a result of the interaction between the induced eddy currents and the angular defects inside an aluminium sample. Through the simulations, we have obtained a basic understanding of the temperature distribution caused by the interaction of the eddy current with an angular defect. Based on the analysis of the temperature distribution obtained from the simulation results, features have been extracted for defect characterisation and for thermographic discrimination of angular defects from the thermal responses.

The two features which have been extracted, (1) the SL feature, and (2) the $T_{\max}$ feature, provide: (1) a relationship between the mapped temperature profile from a defect and the angle of the defect and (2) a means to quantify its length and depth inside the sample. It has been shown through the analysis of the results, that the angular characteristic of a defect influenced the overall temperature distribution. Thus, the investigation of defect length and depth inside the inspected sample has to first take into consideration the angular characteristic of the defect, before any other quantitative measurements from the acquired responses are made.

Verification of the simulation results and analysis has been performed through experimental investigations with a lab sample having man-made angular defects, presented in section 6.3. Comparisons of the experimental and simulation results show good agreement, confirming the feasibility of PEC thermography: its extracted features can be used in acquiring information of angular defects through the visualisation and mapping technique. Further investigations using the extracted features from PEC thermography on in-service samples will be presented in the following chapter in order to verify the effectiveness of this technique for the characterisation of angular defects.

Chapter 7

PEC thermography investigations of angular defects in rail heads

In Chapter 6, investigations using numerical simulation and experimental work were made into the thermal behaviour of specimens containing angular defects; the resultant temperature distribution was analysed for the QNDE of angular defects. From these investigations, the influence of an angular defect's shape and inclination on the thermographic information gathered by the PEC technique was discussed.

In this chapter, experimental investigations using the PEC thermography technique are made on industrial components containing real angular defects. These particular types of defect are often found in rail track components and they could become the cause of rail track failure if they are not discovered early enough. One of the growing concerns in the transportation industry is the increase in problems caused by rolling contact fatigue (RCF) in high speed and mixed heavy load rail use, which leads to crack formation in rail heads [141]. RCF is a significant cause of rail failure and it occurs on or very close to the rail head surface. Cracks caused by RCF develop from the surface and usually propagate at their early stage at a shallow angle, but these can sometimes grow from a shallow to a steeper angle [142]. An ability to estimate the angles at which the crack is growing and subsequently measuring the length to which it extends inside the component is useful in assessing the structural integrity of the investigated component. In rail tracks, it is believed that cracks which grow parallel to the surface are generally safe to be left, whereas those that develop in a direction normal to the surface must be investigated further.

Identifying the orientation of cracks in rail heads in order to predict the future usefulness of a component is an important element of its NDE assessment. Using the capabilities of the PEC thermography technique and the understanding of how heat distributes with different type of defects exhibits in Chapter 5 and Chapter 6, the experimental technique will now be applied to look at angular types of defect in a rail head sample which has been used in-service.

7.1 Rail head inspection in NDE

Rail head inspections for detecting surface and subsurface defects are systematically performed using various NDE techniques. RCF cracks which occur on the rail heads, typically near the gauge corner, are increasing due to higher train speeds and increased loads [143]. These RCF cracks often occur in clusters and propagate into the rail at a certain angle to the surface [143]. They are formed by the rolling contact between the wheels and the rail head and are oriented in the wheel travel direction [144].

Several NDE techniques based on ultrasound and electromagnetic principles have been utilised for inspecting RCF cracks on the rail heads. Conventional ultrasonic wheel probes contain a number of transducers sending bulk waves at different angles into the railhead, covering a localised inspection area underneath the probe. Commonly-used ultrasonic inspection devices (vehicle mounted and hand-pushed trolley) employ systems with multiple probes; a typical configuration would be a 70^{o} probe to detect head cracks, a 37^{o} probe for bolt hole cracks and internal oblique cracks, and a 0^{o} probe to detect horizontal cracks and to monitor the coupling status of the device, all working at 2.5MHz - 5MHz [145]. In order to inspect a long section of rail, the probe has to be moved along the rail with good coupling conditions at the probe/rail interface [146].

Although ultrasonic probes have proved an excellent tool in the detection of cracks in the interior of a rail cross-section, initiated for example by small manufacturing defects, they do suffer from a number of drawbacks:

- As always with conventional ultrasonic testing, acoustic coupling between the probe and the rail must be optimised for the technique to work well. This means that an acoustic couplant must be introduced but even then, problems can be encountered where the surface of the rail is damaged or where substances such as leaf mould, sandite or lubricant are present on the surface of the rail [147].
- There is a lack of sensitivity to shallow, surface breaking defects.
- Surface defects (such as those commonly caused by RCF) can cause shadowing or blocking of the ultrasonic wave corresponding to deeper, more serious defects [148].

Clearly the increase in RCF-initiated cracks in recent years makes the third issue a very important one. This problem is so serious that in some instances rail surface grinding or re-profiling has been used as preparation for ultrasonic inspection to detect deeper, more serious defects.

In the last decade many new rail inspection techniques have been introduced. Ultrasonic techniques have been extended to provide systems with non-contact deployment and better sensitivity to surface defects. Low frequency surface wave techniques have been developed by a number of institutions, including the University of Warwick [149] and Imperial College [146] in the UK and Pennsylvania State University in USA [150]. The length and depth of RCF- initiated cracks can reach 25 mm and 10mm respectively. In order to detect and measure that defect depth range, surface waves in the 200 kHz - 400 kHz frequency range are required [145, 146]. A study using a local immersion probe containing an 8 element transducer array (65 mm wide, centre frequency 250 kHz) proved to be successful in the detection of both vertical and angled defects of different depths and showed some improvement in the detection of shadowed defects through the detection of deep notches in clusters of shallow defects [146]. A non-contact version of the surface wave approach has been developed at the University of Warwick [149], using electro-magnetic acoustic transducers (EMATs) working at a small standoff distance. These two approaches have their strengths and weaknesses; the former contact probe exhibits high sensitivity but slow detection speed, the latter non-contact technique has low sensitivity and is prone to lift-off effects, but has the potential for a fast detection speed. Although these innovations in ultrasonic testing have the potential to improve defect detection and characterisation capabilities, there is still further scope for improvement.

In the field of electromagnetic inspection methods, a non-contact eddy current device has been developed by the Federal Institute for Materials Research and Testing (BAM) in Germany for Die Bahn AG (a German railroad carrier) [151]. The eddy current probe has a high resolution when head check distance is within the range of a few millimetres but, typically with electromagnetic methods, sensitivity decreases with depth. The system was deployed on a train at a speed of 76 km/h, with favourable comparison to readings taken with a hand-held device. The probe has two potential applications: firstly, as a complementary technique to be deployed alongside ultrasonic testing in order to detect surface defects that are problematic for the ultrasonic system and secondly, to assess the quality of regrinding work by checking whether the reprofiling operations have indeed been successful in removing all the head checks.

Another electromagnetic method deploys the ACFM technique to rail inspection; this was developed by TSC Inspection Systems in conjunction with the University of Birmingham [152, 153]. A sensor probe is placed on the surface to be inspected and an alternating current is induced into the surface. When no defects are presence, the alternating current produces a uniform magnetic field above the surface. Any defect present will perturb the current, forcing it to flow around and underneath the defect; this causes the magnetic field to become non-uniform and sensors in the ACFM probe measure these field variations. As with the eddy current system, ACFM is optimally sensitive to surface breaking, shallow defects of the type initiated by RCF but, as the ACFM signal strength diminishes with the square of lift-off, not with its cube (as is the case for eddy current sensors), it will operate with a much greater lift-off [151]. ACFM has been deployed commercially by TSC as a push-along trolley device in the form of the ACFM walking stick [153], and tests at Birmingham have successfully detected artificial defects (notches) in a disc sample at speeds of over 120 km/h [152, 154].

Clearly the area of rail defect detection has received much attention in the last decade, especially with regard to RCF-initiated cracks, but no single inspection technique has come to the fore. Currently, combinations of techniques are needed for a full assessment of the status of the rail; a typical combination using ultrasonics to detect and characterise subsurface defects and eddy currents to detect surface breaking defects.

7.2 Rail heads investigations via PEC thermography technique

Figure 7.1a shows a section of a rail head sample used for the investigation. The rail head sample has fine cracks at its edges and, caused by RCF, these cracks propagate at a certain angle inside the sample. The PEC thermography technique is employed to investigate angular types of defect in a rail head sample which has been used in-service. The investigation demonstrates the capability of the PEC thermography technique to characterise real defects in industrial components, based on the visualisation and the mapping of thermal distribution. With this information, the integrity of the rail as a whole can be evaluated in terms of whether it should be replaced or whether it is safe for further use in-service.

One advantage of the PEC thermography technique compared to ultrasonic techniques in inspecting RCF cracks is that it can easily segregate the cracks, even if they are in a cluster. That is a challenge for ultrasonic inspection, when bigger cracks can be masked by nearby smaller cracks, and therefore serious defects could be missed [142]. Although the focus of NDE inspection on RCF cracks is mainly for the detection of the cracks, the angular characterisation of the RCF cracks using the features extracted from the PEC thermographic signal is an important aspect that needs to be addressed before any quantitative depth measurement is done. If quantitative estimation of the crack depth is required, the angle of the crack should be initially acquired since the angular characteristic of the cracks masks the actual depth/length of the crack inside the sample, as discussed in the previous chapter.

The steel rail head sample used in this study is 65mm in length and 70mm wide and this type of rail head is the standard type for existing rail networks in the UK. Both edges of the rail head have curved geometry and RCF-originated cracks tend to form at these locations, leading to the failure of the rail track section. Figure 7.1b shows the schematic drawing of the investigated rail head sample and also highlights one of the edge areas of the rail head which is investigated using the PEC thermography technique. The defects found at the edge area of the rail head are formed by the rolling contact between the rail head surface and the passing train wheels.

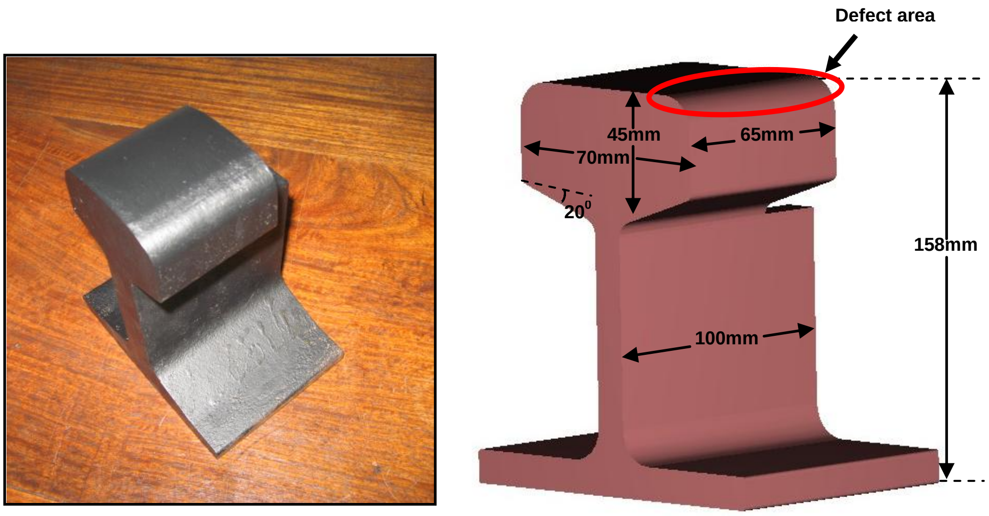

a) b)

Figure 7.1: a) Rail head sample having cracks at the edges caused by RCF; and b) Schematic drawing of the rail head sample (drawing is not to scale)

A similar PEC thermography experimental system setup to that introduced in Chapter 6 is used in the investigation, where a FLIR SC7500 IR camera is utilised to capture the resultant thermal images. The square coil is again used to simulate a line inductor configuration for the local heating of the investigated area of the rail head sample. A current of 380A RMS is applied to the coil for a maximum of 100ms of heating, images being acquired at the maximum full frame data acquisition rate of an IR camera. In these tests the frequency settled at 259 kHz. Prior to testing, the steel rail head sample is painted with a black acrylic paint to increase and even out the thermal emissivity at the sample surface. Such black paint of uniform and high emissivity in the infrared band has a low reflectivity, thus if it is applied on low emissivity surfaces, interferences caused by neighbouring warm bodies are reduced.

7.3 Experimental results

7.3.1 Thermal visualisation and analysis

Visualisation of the thermal distribution via the PEC thermography technique has the ability to reveal the presence of a defect in an investigated sample by the interaction between the induced eddy currents and a defect itself. Through the analysis of the resulting temperature distribution, a characterisation of the defect inside the sample can be made.

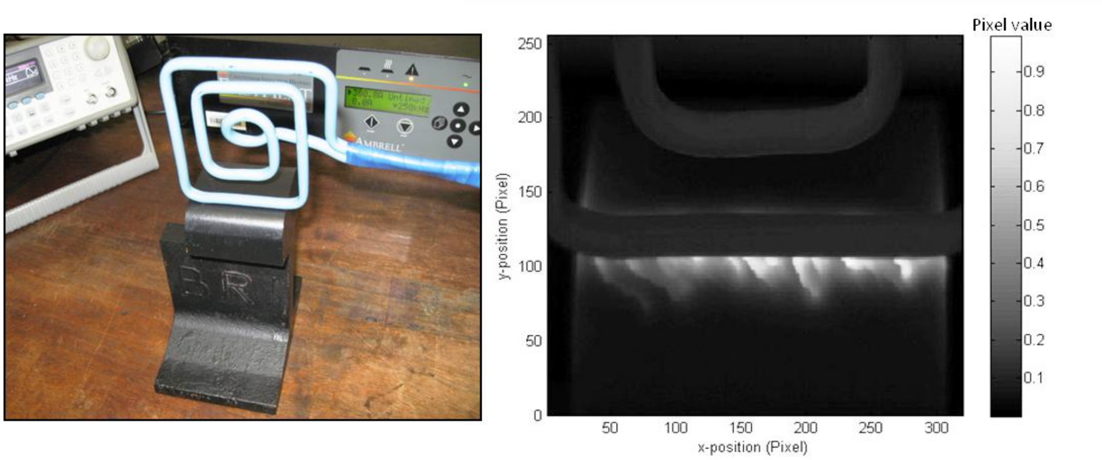

a) b)

Figure 7.2: a) Coil positioned for the detection of RCF cracks at the edge of the rail head sample and b) Thermal image after 100ms of heating at the rail head edge

In the experiment, the square coil is positioned normal to the sample surface, near the edge of the rail head (Figure 7.2a), where RCF-induced cracking is known to concentrate. This configuration simulates a line inductor, with localised heating in the area under the coil. Figure 7.2b shows the thermal image captured by the IR camera after 100ms of heating, which discloses the presence of defects at the edge of the rail head. The presence of the cracks is made visible by an increase in the temperature distribution at the cracks' edges, resulting from the diversion of the induced eddy current as it conforms to the shape of a crack to complete its path.

To analyse the captured thermal image in Figure 7.2b, a temperature linescan is taken at the area along the coil edge and is shown in Figure 7.3. The linescan shows the variation in surface temperature measured by the respective pixel value taken across the sample length. From the temperature distribution shown in this figure, the presence of the cracks at the rail head can be clearly observed. The peaks of the distribution correspond to the presence of a crack or a cluster of cracks at close vicinity to each other. The location of the cracks is identified by referencing back the position of the peaks with the corresponding pixel position. In normal cases, the characterisation of a defect is based on the amplitude of the acquired thermographic signal, higher amplitude indicating higher severity in terms of size and length inside the sample. However, this is not the case if the defect has an angular orientation inside the sample. The angular characteristic of the defect affects the overall temperature distribution, and should be taken in account as discussed in the previous chapter.

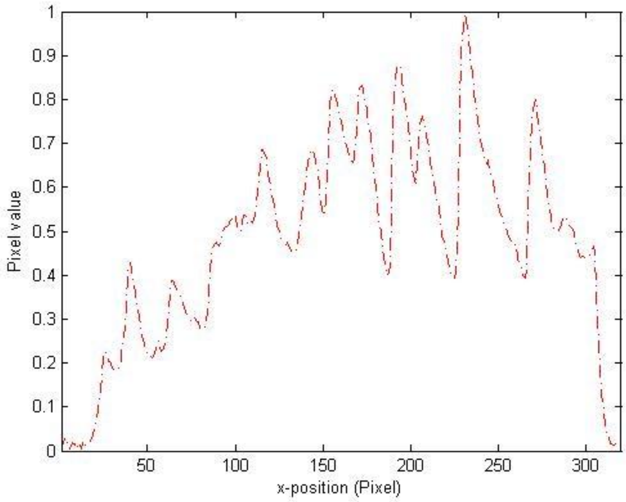

Figure 7.3: Linescan of the temperature distribution for the rail head sample taken at the edge of the coil

Prior to testing, the geometrical orientation of any cracks which may be present is unknown. One of the major factors influencing the temperature distribution due to the interaction between the induced eddy current and the defect inside an investigated sample is the orientation of the defect to the coil position. In practice, the coil's configuration should be adjusted to obtain the largest detection sensitivity [155]. Since the captured thermal image shown in Figure 7.2b indicates that the cracks are orientated in a certain direction at the surface, the orientation of the coil has to be adjusted before any analysis of the temperature distribution linescan is performed. With the PEC thermography technique, the signal contrast from cracks is optimal if the coil is positioned perpendicular to the crack orientation [129]. However, due to the surface at the edge of the rail head being curved, the coil's lift-off from the surface has to be managed carefully. During the experiment, the coil is positioned as close as possible to the surface area of interest to avoid lift-off effect, and in order to get reliable and consistent results.

Based on the discussion on the coil's orientation above, the arrangement of the coil and the rail head sample should be adjusted so that the coil orientation is approximately perpendicular to the direction of the cracks, as shown in Figure 7.4a. The resultant thermal visualisation captured by the IR camera of the cracks at the rail head is shown in Figure 7.4b. It can be seen from the figure that the coil orientation is now well adjusted to be approximately perpendicular to the orientation of the cracks. With this new arrangement, the detection of the presence of cracks is increased as the cracks are optimally disturbed by the eddy current flow. However, as mentioned before, the heat intensity or amplitude coming from a particular crack does not directly indicate the geometrical information in terms of size and depth of the crack. Therefore, analysis of the acquired thermal signal from the crack in terms of its profile should be performed.

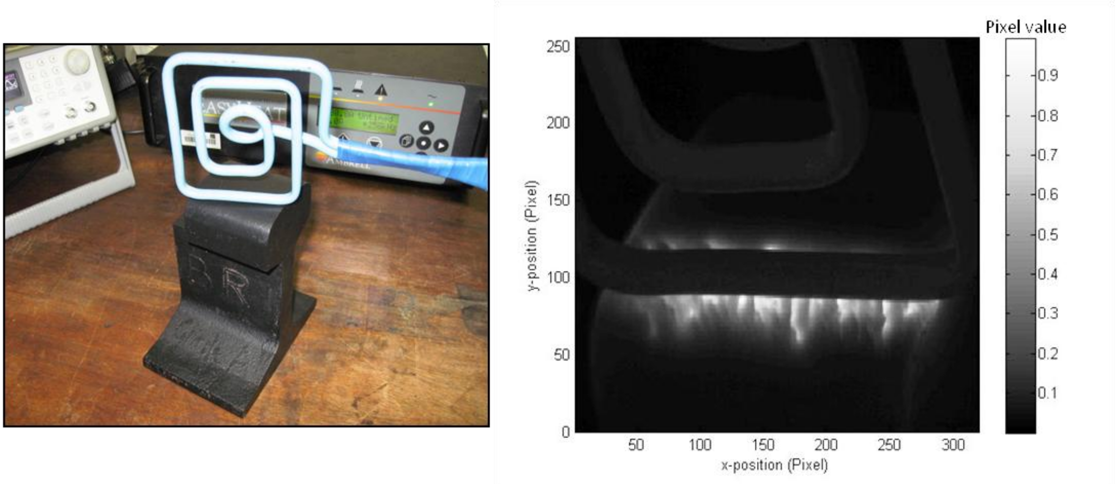

a) b)

Figure 7.4: a) New coil and sample arrangement; and b) The resultant thermal distribution

7.3.2 *Multiple defect mapping*

Figure 7.5 illustrates changes in the type of defect that becomes evident at different times in the heating cycle. It can be seen from the figure that the change in the heat distribution with time follows this pattern:

- Early stage heating: Fine network of cracks visible, with similar amplitude for shallow and deep cracks. This is evident in Figure 7.5a), where all the cracks cause a similar increase in heating at 18ms.
- Later stage heating: Deeper (and more acute angle) cracks result in greater heating at the surface. The result is that the deeper cracks now dominate the heat distribution, though the heat generated from shallower cracks is still evident and

is superimposed on the larger heating gradients caused by deeper cracks. See Figure 7.5b).

- Cooling stage: Only very deep/acute cracks evident, as is shown in Figure 7.5c), at 157ms.

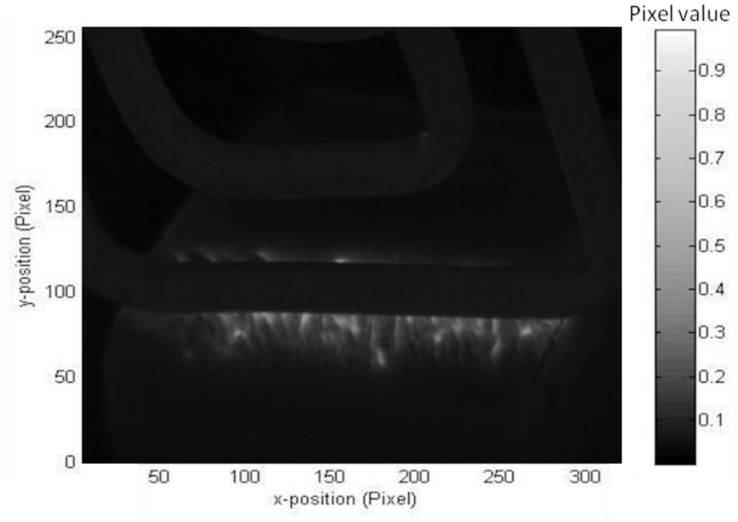

a)

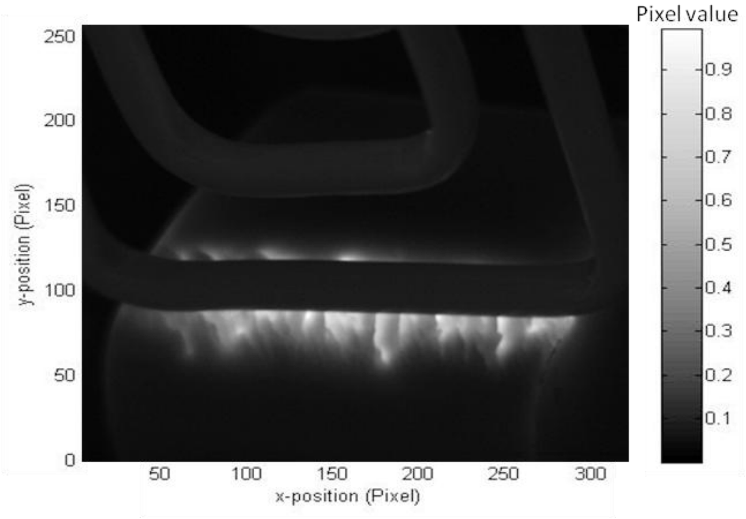

b)

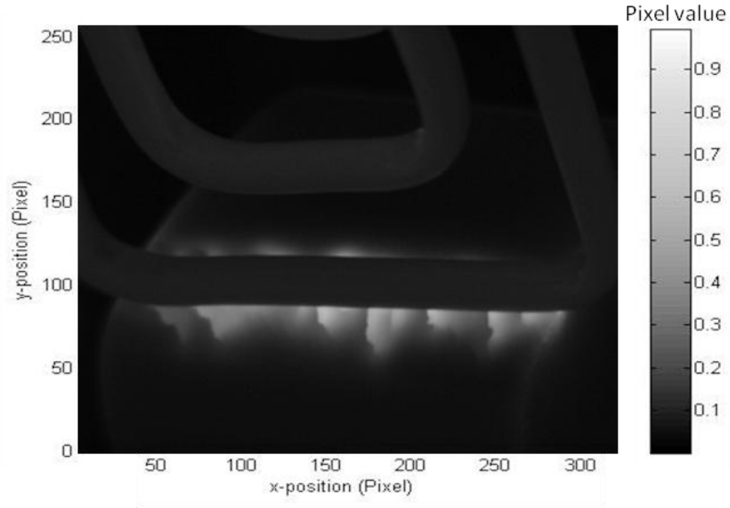

c)

Figure 7.5: Change in heat distribution with time; a) Early stage heating - 18ms, b) Later stage heating - 100ms, c) Cooling - 157ms

As discussed in Chapter 6, measurement of the length and depth of the cracks must take into consideration the angular characteristics of the cracks. Since the maximum temperature amplitude acquired from the temperature linescan of cracks is affected by three geometrical parameters, angle, length and depth, prior knowledge about the crack's angle inside the inspected sample is the key to acquiring quantitative information regarding the defect length and depth. However, the two PEC thermography features; SL and $T_{\max}$, still need the comparative measurement from a reference sample having known defect geometry before values of the measured features are quantified for characterisation of the investigated defect.

7.3.3 Transient analysis

In Chapter 5, transient analysis of the thermographic distribution at several distinctive points was described. It has been shown that defects exhibit behaviour which is equivalent to that of either a defect or notch, or a combination of both, depending on the positional relationship between the coil inductor and the defect, with the surface transient heating pattern playing a crucial role for defect characterisation. In order to provide a better description of cracks found in the rail head, transient analysis for the temperature profile should be conducted by taking the temperature history at several positions in the vicinity of the investigated crack. The analysis provides information regarding the length of the crack as measured at the sample surface.

To analyse the transient temperature change, two data averaging positions are chosen to represent the development of heating around the crack. These are shown in Figure 7.6 as #1 (the tip of the crack) and #2 (at the side of the crack). The mean pixel value is chosen to quantify the heating at these positions and analysis of the change in heating over time is achieved by the extraction of pixel values from the image sequence. Each pixel value represents the change in temperature over time of the corresponding point on the sample surface.

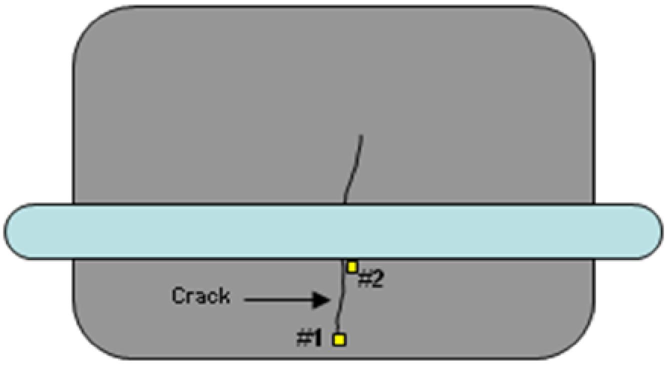

Figure 7.6: Data acquisition positions #1 and #2 for analysis of transient temperature

Figures 7.7a show the temperature distribution after 100 ms of heating for the rail head sample, and Figure 7.7b shows the corresponding transient temperature profiles at positions #1 and #2 for the crack highlighted by the green circle in Figure 7.7a).

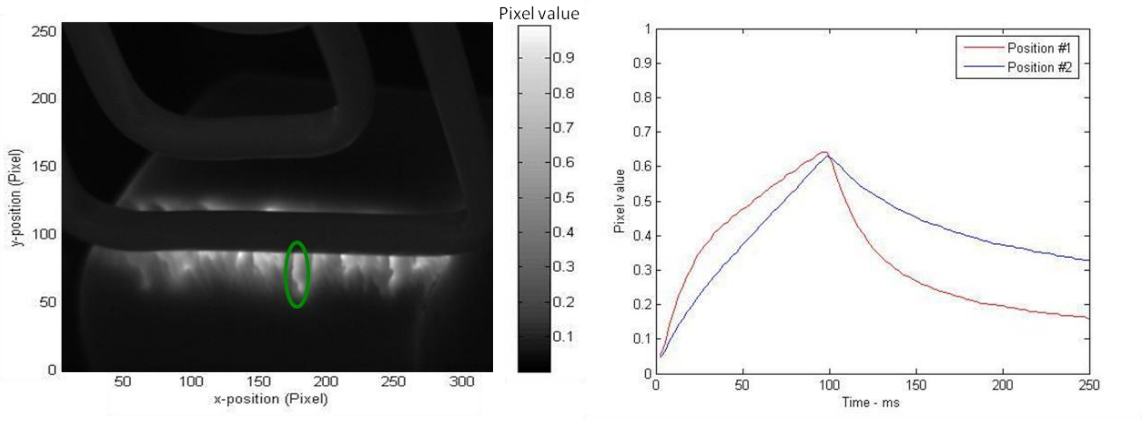

a) b)

Figure 7.7: a) Temperature distribution after 100ms of heating for the rail head sample; and b) Transient temperature profile at position #1 and #2 after 100 ms of heating of the highlighted crack

Throughout the 100ms heating period, it can be observed from Figure 7.7b) that position #1 exhibits higher temperature readout from the start of the heating until 100ms as compared to position #2. The fundamental behaviour of eddy current heating was discussed in Chapter 5. The diversion of eddy currents around the tip of the crack results in a hot spot at its tip, coupled with a relatively cooler area at the centre of the crack, where eddy current density is decreased. After the heat is switched off at 100ms, the temperature values at positions #1 and #2 exhibit different profiles. Position #2 cools at a slower rate than position #1, indicating the contribution of the surrounding area towards the diffusion of heat in the cooling period. At position #1, heat diffuses faster due to a wider area for the heat to disperse into, while at position #2, the diffusion area is limited to only one side of the crack edges.

From the results, it is observed that the temperatures at position #1 and position #2 (which are the distinctive points for describing the crack) during the heating and cooling period depend on the geometrical characteristics of the crack. The tip or the end of the crack always exhibits a higher transient temperature throughout the heating period compared to the side of the crack. This observation gives information regarding the end (or tip) position of the crack, which are both useful in measuring the length of the crack and also for condition-monitoring of the propagation of the crack at the sample surface.

7.4 Summary

Experimental investigations on rail heads having RCF cracks have been performed via PEC thermography in relation to angular defects, and the results and analysis are presented. The work shows that PEC thermography is a viable system for the imaging of multiple defects in components such as rail heads. Because the IR camera used with the PEC thermography system is capable of capturing images over relatively large areas, the technique is an efficient one for the effective detection and measurement of multiple, natural cracks inside in-service components.

Further investigation of the cracks through the transient analysis has been presented. This provides additional information regarding the surface length, or the size of the crack measured at the sample surface, useful for condition-monitoring and QNDE of real defects within in-service parts or components.

Overall, the investigations of this chapter have demonstrated the capacity of PEC thermography to map multiple defects simultaneously, with an ability to discriminate between some of the closely-spaced defects. The different characteristics of the temperature distribution and the transient temperature changes clearly have the potential to allow defect geometry to be determined to some extent.

Chapter 8

Conclusions and further work

In this final chapter, the research work is summarised and conclusions are drawn about its capacity to provide QNDE for angular types of defect. Finally, potential future directions of research are outlined for both the numerical simulations and the experimental technique for defect characterisation.

8.1 Conclusions

The focus of this work has been on quantifying angular defect geometries by the visualisation and mapping of magnetic field distribution using pulsed eddy currents (the PEC technique), or of temperature distribution (the PEC thermography technique). Particular features of the distributions have been extracted from numerical simulations, which provide information on the geometry of defects within a sample. Experimental investigations were then performed to verify the simulation results and to test the feasibility of the proposed techniques and extracted features for practical use in acquiring information about an angular type of defect. It is hoped that results gathered through this work will benefit industry's requirements for the quantification of real-life defects with complex geometries.

Chapter 2 presented an extensive literature survey on defect detection and characterisation by NDE techniques and the particular techniques of defect imaging through magnetic field mapping via PEC, and temperature mapping via PEC thermography. The modelling approach using numerical (simulation) studies was outlined in section 2.2.1 and the experimental approach in section 2.2.2. In Chapter 4, the work examined the use of PEC for defect characterisation and in Chapters 5 and Chapter 6, PEC thermography investigations on samples containing angular defects were presented. Chapter 7 then described the application of PEC thermography in the detection of multiple defects related to angular defects in rail heads.

A number of crucial aims informed the work undertaken for this thesis : (1) To avoid misinterpretation of the response signal when applying a QNDE approach for defect quantification, by taking into consideration the angular characteristic of defects in the inspection results; (2) To understand the underlying phenomena surrounding a particular defect and to provide guidelines for experimental designs, 3-D FEM numerical simulations were performed for helpful feature extraction from the acquired distribution responses when applying a QNDE approach to the investigated defect; (3) To demonstrate means for identifying the angular characteristics of a defect from the extracted features and to provide a transient analysis of magnetic field distribution and temperature distribution; (4) To construct links between the acquired information, i.e. magnetic field and temperature distributions, and the 3-D shape, size and location of defects (5) To arrive at a forward approach in defect characterisation, via the mapping of resultant distributions and pattern recognition from the interaction of eddy currents with geometrically complex defects.

The conclusions and the contributions can be summarised in details as follows:

8.1.1 *3-D FEM modelling of PEC and PEC thermography investigations on angular defects*

A 3-D FEM numerical approach was taken in this work because of its significant advantages over analytical modelling for the study of angular types of defect. In this research, the simulations are performed to predict the outcomes of the interaction between the induced eddy currents with defects in conductive samples, mapping the form of a magnetic field distribution (PEC) and a temperature distribution (PEC thermography). Analysing the simulation results helps to construct the link between the acquired information, i.e. magnetic field and thermal distribution, and the 3-D shape, size and location of an interacting defect. This not only facilitates the forward problem but also the inverse process that involves experimental system specification and configuration, pattern recognition, defect quantification and reconstruction of 3-D defects for PEC and PEC thermography technique. Details are as follows:

- The simulations provided an understanding of the underlying phenomena of magnetic field distribution and temperature distribution due to the presence of a defect inside the investigated sample, observed through graphically simulated visualisation of the phenomena. Through the mapping, features are extracted based on the profile change with different defect geometries. These feature are then used to obtained information about the angle of the defect and its length/depth inside the sample.

- Features have been identified from numerical investigations of magnetic field distribution when eddy currents interact with angular defects. From the magnetic field mapping, a correlation between the peak distribution shift and changing angles of defect inclination helped to predict the angle of the defects. In a temporal analysis of the magnetic field, the width of the peak of the mapped distribution shift provides information in terms of the depth/length of the angular defects inside the investigated sample. Although the features provide geometrical information about angular defects, it was realised from the simulation results that the PEC technique has limitations in performing the mapping and visualisation task. The main factors that limit its capability and practicality are 1) spatial resolution; 2) high cost in construction; 3) rigidness of the array configuration; 4) interference; and 5) inspection efficiency.

- Multiphysics FEM simulation investigations have provided an understanding of the fundamental behaviour of eddy current heating and heat diffusion in the presence of two fundamental defects, a slot and a notch. From the simulations, the heating mechanism around a particular defect is visualised and the resulting thermographic responses in the presence of a defect are explained. The resultant heat distribution in the presence of natural defects can be understood by considering the contributions from the two fundamental defect modes: heating at the tips of defects due to lateral diversion of eddy currents (slot) and heating at the edges and a slight increase of temperature at the bottom of the notch below the defect due to medial diversion of eddy currents (notch). The simulations also help to develop system design for a PEC thermography experimental set-up, particularly the IR camera speed required to obtain the information for the necessary transient analysis.

- Simulations on angular defects show that the angular characteristic of a defect affects the eddy current distribution and hence the acquired temperature responses. Due to its angular (or sloping) nature, more heat is trapped in the slanted area above a defect, so higher temperatures are observed above a defect with a larger angle compared to those above a smaller angled defect. The simulations provided mapped thermal data on how the temperature distribution profile changes with different defect angles and length, from which two features were extracted (see Chapter 6, section 6.2.2). Analysis of these features, (1) temperature slope, SL and (2) maximum temperature amplitude, $T_{\max}$ established relationships between the mapped temperature distribution profile and (1) the angle of the defect and (2) its length and depth inside the sample, i.e. the vital information needed for QNDE of a defect.

Overall, the 3-D FEM simulations provided necessary information and guidance throughout the study of angular defects. From an initial study of the interaction of eddy currents with defects and the resulting temperature distribution to the extraction of the above-mentioned features, the FEM simulations have assisted the research in achieving its aims and objectives. 3-D FEM simulations can provide the basis for further work in the field of QNDE for defect detection and characterisation.

8.1.2 *QNDE approach using extracted features from numerical investigations for complex defect quantification*

Defects or cracks rarely have a simple geometrical shape, so the influence of defect shape and orientation on the information gathered by the utilised technique must be assessed carefully in order to avoid misinterpretation of the response signals. It has been shown through numerical investigations that the angular characteristic of a defect will influence the overall magnetic field distribution and the temperature distribution resulting from interaction between eddy currents and defects. Thus, the investigation of defect length and depth inside the inspected sample must take into consideration the angle of the defect before making any quantitative measurements based on the acquired responses.

From the simulation work on PEC thermography, two features were extracted to be used in gaining geometrical information about the defect. These features; 1) the SL feature and 2) the $T_{\max}$ feature, provided quantitative measures of angle, length and depth of the angular defects inside the investigated sample.

The initial investigation concerns the angle of a defect (see Section 6.2.2). Since the temperature gradient, ∇T , is directly proportional to the heat source induced by the eddy current, defects having the same angle (thus the same heat source density, Q) but different lengths, always display the same ∇T in the area enclosed between the defect and the sample surface. Through the analysis of simulation results for angular defects via PEC thermography, this feature has proved to be independent of defect length and depth. Therefore defect angles can be measured by this feature.

Following the determination of the defect angle, its length and depth were obtained via the $T_{\max}$ feature, acquired from the temperature distribution. This is done through comparing the maximum temperature amplitude for defects having the same angle, since the difference in heat intensity due to different length and depth manifests itself as a difference in the acquired temperature amplitude. Using this approach, the length and depth of defects can be quantified.

8.1.3 Experimental verification and visualisation of eddy current imaging and distribution from defect interaction

Experimental results from PEC thermography show a good agreement with the simulation results in terms of angle identification and its depth/length inside the sample. The extracted features acquired from the simulation studies have been tested with a lab sample having man-made angular defects. The two features from temperature mapping in the vicinity of the angular defects have been examined and comparisons with the simulations results were made.

In Chapter 7, PEC thermography was conducted on rail head samples containing RCF cracks (which are known for their angular character). The results demonstrated the effectiveness of the PEC thermography technique when mapping multiple defects simultaneously, showing an ability to discriminate between some of the closely-spaced defects within an in-service sample. However, as is usuall in NDT inspection, comparative measurements from a reference sample having known defect geometry are needed before the measured features can be quantified for characterisation of the investigated defect.

8.2 Further work

Following the research outcomes achieved in this research, the directions of future work are given in terms of expanding the scope of the research with current experience for guidance.

8.2.1 Expand the simulation approach for defect characterisation

Simulation models for PEC thermography, which couples two different fields of physics; electromagnetics and heat transfer, require high values of computational memory in order to obtain accurate results, due to the required mesh density at the selected areas of interest. This results in longer computational time and reduces the efficiency of the simulation. This could be resolved in expanding the simulation approach by combining analytical and numerical methods to solve the problem in both two and three dimensions.

For example, the problem could be segregated in accordance with the capability of the methods. Symmetric problems in the model could be solved using the analytical method, either in two dimensions or expanded to a 3-D environment. The rest of the model relating to complex geometries could then be solved by numerical methods. Combining both these methods will result in a faster solution and increase the efficiency of the simulation work.

8.2.2 Feature extraction techniques and integration

Features extracted from PEC thermography were acquired from a linescan at the sample surface showing the profile of the temperature distribution in the vicinity of a defect.

Although the features provided geometrical assessments of defects, the temperature data gathered is limited to single dimensional information.

An area scan instead of a single linescan could provide 2-D information about the heat diffusion at the defect area, which could provide more information about the defect geometry and faster defect identification through the analysed data. Knowledge of how the heat is interacting with defects and the resulting direction of heat diffusion might provide additional features which are related to defect geometry and which could be used for 3-D defect reconstruction.

This can be accomplished through a Digital Image Correlation technique (DIC), which has been widely used to track the pixel changes through a sequence of image frames. The diffusion of heat and its interaction with a defect can be visualised by the DIC technique which gives an early indication of the nature of the defect inside the investigated sample. Since heat diffusion in the vicinity of a defect can be tracked by changes in the pixel values, the direction in which heat propagates within the sample could indicate defect dimension and orientation through an analysis of the area scan. This could then be expanded to 3-D information with the addition of temperature changes measured over time at the area of interest.

The two features extracted from the temperature distribution, i.e. the SL and the $T_{\max}$ features, can provide a complete geometrical assessment of a given defect. Since the features give us information on different geometrical aspects of the investigated defect, integration of these features gave the overall information needed for a complete defect characterisation. With additional variation of defect geometries, i.e. different defect angles, lengths and depths, a plot formed by the integration of the SL and $T_{\max}$ features could be the reference for developing an inverse model for a 3-D characterisation of an unknown defect inside an investigated sample.

8.2.3 Application of PEC thermography on industrial components

Since PEC thermography has shown its effectiveness in the detection of multiple defects in rail heads, the utilisation of this technique should be expanded towards other components. However, there is the need for a comparative measurement from a reference sample having known defect geometry before the measured features can be quantified for characterisation of the unknown defect under investigation.

The evaluation of defects in industrial components can be assisted by the use of an artificial crack produced inside a ready-made sample. For example, the use of a Trueflaw sample which has a crack produced by the thermal fatigue cracking mechanism can provide a more realistic test defect. Work on the investigation of a crack inside a Trueflaw sample has been conducted using the PEC thermography technique. The Trueflaw sample and crack parameters used in the investigation are presented in Table 8.1. These true parameters of the crack can be used to assess the technique's performance for defect characterisation. Figure 8.1 shows an example of PEC thermography results on the Trueflaw sample. From the figure, it can be seen that the crack in the sample can be detected and a good definition of the crack shape can be observed from the thermal image.

Table 8.1: Trueflaw sample and crack parameters

Cracking mechanism	Thermal fatigue
Material grade	AISI304
Material group	Austenitic stainless steel
Material thickness	10.0 mm
Crack length	15.9 mm
Crack depth	2.3 mm

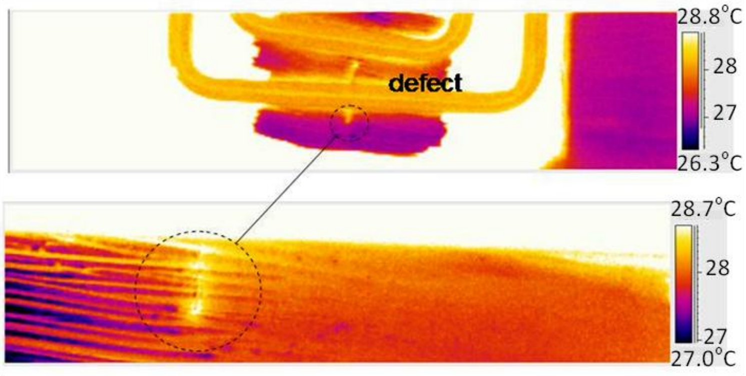

Figure 8.1: Thermal image showing the crack in the Trueflaw sample obtained by PEC thermography

The Trueflaw sample investigation results can provide the reference for defect quantification applied to other industrial components, e.g. turbine blades. Preventive maintenance on turbine blades, which are critical components in power generation industries, is an important factor in cost and safety issues within those industries.

Recently, the use of thermal barrier coating (TBC) on turbine blades has been common practise in the industry to allow higher operating temperature and to extend the life of the blade by reducing oxidation and thermal fatigue. However, since it would be costly to remove the coating before investigating them, inspection of the turbine blades becomes more complicated. Standard inspection technique for turbine blades would be the use of dye penetrant, but with the utilisation of TBC, this technique becomes inapplicable.

PEC thermography could provide the solution for inspecting turbine blades treated with TBC, where eddy currents could be induced inside the blades even with the presence of the coating. The induced heat in the TBC layer is uniform (as in a defect free area), whereas the presence of an interior defect will result in a relatively large amount of heat accumulated around the defect, which would be detected by the IR camera of the PEC thermography system. Comparative measurements with the Trueflaw sample could provide the guidelines for defect quantification. The induction of eddy currents at the TBC layer also provides a potential means for evaluating the condition of TBC layers, which would be an added advantage for inspecting the overall condition of the turbine blades.

8.2.4 Expansion of work to other research field

It has been shown that the mapping of the temperature distribution via the PEC thermography technique is an effective technique for defect characterisation. This method of mapping can be further applied to the medical field, where Transcranial Magnetic Stimulation (TMS) has been used for the study of the human brain. The stimulation with TMS is achieved from the outside of the human head using pulses of electromagnetic field that induce an electric field in the brain. The TMS allows for non-invasive stimulation of neurons through the induction of electrical fields in the brain, thereby effecting neuron-stimulated muscle movement.

Numerical simulation of PEC thermography could provide a platform for the study of coil configurations which could improve the TMS penetration into deep brain regions and provide concentrated stimulus at specific areas of the human brain. From the simulation results, knowledge could be gained of the strength of fields needed in order to develop TMS devices with improved capabilities.

A feasibility study has been performed to investigate the practicality of PEC thermography applied to TMS. The aim of the study is to assess whether any change in the temperature of the subject body can be discerned during TMS stimulation. Simulation investigations in COMSOL have been performed and some of the simulation results for this feasibility study are presented in Appendix C.

References

[1] Electromagnetic Testing, Nondestructive Testing Handbook, 3rd Edition, Vol. 5. ASNT Press, ISBN 1-57117-116-9, 2004.

[2] M. Tanaka and H. Tsuboi, 'Finite element model of natural crack in eddy current testing problem', IEEE Transactions on Magnetics, Vol. 37, No. 5, 2001, pp. 3125-3128.

[3] N. Ida and W. Lord, 'A finite element model for three-dimensional eddy current NDT phenomena', IEEE Transactions on Magnetics, Vol. 21, No. 6, 1985, pp. 2635-2643.

[4] N. Ida, 'Development of a 3D eddy current model for nondestructive testing phenomena, Review of Progress in Quantitative Nondestructive Evaluation, D. O. Thompson and D. E. Chimenti, Plenum Press, New York, Vol. 6A, 1987, pp.201-209.

[5] R. Clark, 'Rail flaw detection: overview and needs for future developments', NDT & E International, Vol. 37, 2004, pp. 111-118.

[6] D.G. Harlow and R.P. Wei, 'Probabilities of occurrence and detection of damage in airframe materials', Fatigue Fracture Engineering Material Structure, Vol. 22, 1999, pp. 427-436.

[7] A. Mandelis, 'Diffusion-wave laser radiometric diagnostic quality-control technologies for materials NDE/NDT', NDT & E International, Vol. 34, 2001, pp. 277-287.

[8] B. Raj and T. Jayakumar, 'NDE methodologies for characterisation of defects, stresses and microstructures in pressure vessels and pipes', International Journal of Pressure Vessel & Piping, Vol. 73, 1997, pp. 133-146.

[9] D.U. Gubser, 'Superconductivity research and development: department of defense perspective', Applied Superconductivity, Vol. 3, No. 1-3, 1995, pp. 157-161.

[10] M. Simsir and A. Ankara, 'Comparison of two non-destructive inspection techniques on the basis of sensitivity and reliability', Materials and Design, Vol. 28, No.5, 2007, pp. 1433-1439.

[11] A.J. McEvily, 'Failures in inspection procedures: case studies', Engineering failure analysis, Vol. 11, No. 2, 2004, pp. 167-176.

[12] Z. Zheng, L. Xuan, L. Udpa and S. Udpa, 'Modeling of current excitation waveforms for magnetic particle inspection', Review of Quantitative Nondestructive Evaluation, Vol. 21, 2002, pp. 1984-1990.

[13] http://www.mfrc.ameslab.gov/R-D_Reports/Magnetic_particle_Final-2.pdf, Accessed April 2010.

[14] J.Y. Lee, S.J. Lee, D.C. Jiles, M. Garton, R. Lopez and L. Brasche, ‘Sensitivity analysis of simulations for magnetic particle inspection using the finite-element method’, IEEE Transactions on Magnetics, Vol. 39, No. 6, 2003, pp. 3604-3606.

[15] H. Charles, ‘The ABC's of Nondestructive weld examination’, The Welding Journal of American Welding Society, Vol.3, May 1997.

[16] F. Larry, ‘Welding: Principles and Applications, 5th Edition’, Thomson Delmar Learning, 2002.

[17] B.P.C. Rao, ‘Visual techniques in Non-destructive testing’, Encyclopedia of Materials: Science and Technology, Elsevier Science Ltd, September 2001, pp 6043-6046.

[18] Digital Industrial Radiography Unit, NDT Group, Malaysian Nuclear Agency, Accessed January 2011.

[19] B. Blakeley, and K. Spartiotis, ‘Digital radiograph for the inspection of small defects’, Insight, Vol.48, Issue.2, 2006, pp.109-112.

[20] S.M. Ahonen, ‘Radiography – A conceptual approach’, Radiography, Vol.14, Issue.4, Nov 2008, pp.288-293.

[21] M.S. Rapaport and A. Gayer, ‘Application of gamma ray computed tomography to nondestructive testing’, NDT & E International, Vol. 24, No.3, 1991, pp. 141-144.

[22] H. E. Martz, S.G. Azevedo, J.M. Brase, K. E. Waltjen and D. J. Schneberk, ‘Computed tomography systems and their industrial application’, Int. J. Radiat. Appl. Instrum. Part A, Vol. 41, No. 10/11, 1990, pp. 943-961.

[23] N. Nafaa, M. Zelmat, S.S. Belaifa and M. Tridi, ‘Weld defect detection in industrial radiography based digital image processing’, 3rd IEEE International conference on Sciences Of Electronic, Technologies Of Information And Telecommunications, Mar 2005, pp.1-10.

[24] D.K. Hsu, ‘Nondestructive testing using air-borne ultrasound’, Ultrasonics, Vol. 44, No. 1, 2006, pp. e1019-e1024.

[25] M. Arone, D. Cerniglia and V. Nigrelli, ‘Defect characterisation in Al welded joints by non-contact lamb wave technique’, Journal of Materials Processing Technology, Vol. 176, No. 1-3, 2006, pp. 95-101.

[26] R.S. Edwards, A. Sophian, S. Dixon, G.Y. Tian and X. Jian, ‘Dual EMAT and PEC non-contact probe: applications to defect testing’, NDT & E International, Vol. 39, No. 1, 2006, pp. 45-52.

[27] R.S. Edwards, A. Sophian, S. Dixon and G.Y. Tian, ‘Data fusion for defect characterisation using dual probe system’, Sensors and Actuators A: Physical, Vol. 144, No. 1, 2008, pp. 222-228.

[28] P. Calmon, A. Lhemery, I. Taibi, R. Raillon and L. Paradis, ‘Models for the computation of ultrasonic fields and their interaction with defects in realistic NDT configurations’, Nuclear Engineering and Design, Vol. 180, 1998, pp. 271-283.

[29] L. Parrini, ‘New technology for the design of advanced ultrasonic transducers for high power applications’, Ultrasonics, Vol. 41, 2003, pp. 261-269.

[30] C. Fortunko, R.B. King and M. Tan, ‘Nondestructive evaluation of planar defects in plates using low-frequency shear horizontal waves’, Journal of Applied Physics, Vol. 53, No. 5, 1982, pp. 3450-3458.

[31] M.I. Green, ‘Search coils’, Lawrence Berkeley National Laboratory, University of California, pp. 143-173.

[31] Y. Li, G.Y. Tian, and S. Ward, ‘Numerical simulation on magnetic flux leakage evaluation at high speed’ NDT & E International, Vol. 39, 2006, pp. 367-373.

[32] D. Jinfeng, K. Yihua and W. Xinjun, ‘Tubing thread inspection by magnetic flux leakage’, NDT & E International, Vol. 39, No. 1, 2006, pp. 53-56.

[33] Y. Wang, Y. Xu, S. Ding, G. Dai, Y. Liu, Z. Yang and F. Liu, ‘Numerical simulation and experiment on magnetic flux leakage inspection of cracks in steels’ 17th World Conference on Nondestructive Testing, China, 2008.

[34] Y. Zhang, Z. Ye and X. Xu, ‘An Adaptive method for channel equalization in MFL inspection’, NDT & E International, Vol. 40, No. 2, pp. 127-139.

[35] X-B. Li, X. Li, L. Chen, P-F. Feng, H-D. Wang and Z-Y. Huang, ‘Numerical simulation and experiments of magnetic flux leakage inspection in pipeline steel’, Journal of Mechanical Science and Technology, Vol. 23, 2009, pp. 109-113.

[36] A.A. Carvalho, J.M.A Rebello, L.V.S Sagrilo, C.S. Camerini and I.V.J Miranda, ‘MFL signals and artificial neural networks applied to detection and classification of pipe weld defects’, NDT & E International, Vol. 39, No. 8, 2006, pp. 661-667.

[37] W. Han and P. Que, ‘A modified wavelet transform domain adaptive FIR filtering algorithm for removing the SPN in the MFL data’, Measurement, Vol. 39, No. 7, 2006, pp. 621-627.

[38] Battelle, ‘Dual field MFL pig may provide best of both world’, Pipeline & Gas Journal, 2005.

[39] Z. Chen, G. Preda, O. Mihalache and K. Miya, ‘Reconstruction of crack shapes from the MFLT signals by using a rapid solver and an optimization approach’, IEEE Transactions on Magnetics, Vol. 38, No. 2, 2002, pp. 1025-1028.

[40] G. Riegert, K. Pfleiderer, H. Gerhard, I. Solodov and G. Busse, ‘Modern Methods of NDT for Inspection of Aerospace Structures’, ECNDT, Berlin, Germany, 2006.

[41] X. Maldague, ‘Introduction to NDT by Active Infrared Thermography’, Material Evaluation, Vol. 6, pp 1060–1073, 2002.

[42] J. M. Milne, and W. N. Reynolds, ‘The non-destructive evaluation of composites and other materials by thermal pulse video thermography’, SPIE, Vol 520, pp 119-122, 1984.

[43] W. N. Reynolds and G. M. Wells, ‘Video-compatible thermography’, British journal of NDT, Vol 26, pp 40-44, 1984.

[44] M. Morbidini, P. Cawley, M.J.S. Lowe, T. Barden, and D.P. Almond, ‘A Investigation of Thermosonics’, WCNDT, Montreal, Canada, 2004.

[45] G. Riegert, T. Zweschper and G. Busse, ‘Lock-in thermography with eddy-current excitation’, Quantitative Infra Red Thermography Journal, Vol. 1. 2004, pp. 21-32.

[46] G. Zenzinger, J. Bamberg, M. Dumm and P. Nutz, ‘Crack detection using eddytherm’, Review of Progress in QNDE, Vol. 24, 2005, pp. 1646-1653.

[47] U. Netzelmann and G. Walle, ‘Induction thermography as a tool for reliable detection of surface defects’, 17th World Conference on Nondestructive Testing, Shanghai, China, 2008.

[48] B. Oswald-Tranta, ‘Thermo-inductive crack detection’, Nondestructive Testing and Evaluation, Vol. 22, 2007, pp. 137-153.

[49] S. Pickering and D.P. Almond, ‘Matched excitation energy comparison of the pulse and lock-in thermography NDE techniques’, NDT & E International, Vol. 41, pp 501-509, 2008.

[50] Canadian General Standard Board, Advanced Manual for Eddy Current Test Method, CAN/CGSB-48.14-M86.

[51] G.Y. Tian and A. Sophian, ‘Study of magnetic sensors for pulsed eddy current techniques’, Insight, Vol. 47, No. 5, 2005, pp. 277-279.

[52] F. Thollon, B. Lebraun and N. Burais, ‘Numerical and experimental study of eddy current probes in NDT of structures with deep flaws’, NDT International, Vol. 28, No. 2, 1995, pp. 97-102.

[53] G.Y. Tian and A. Sophian, ‘Pulsed eddy current sensor’, Encyclopedia of Sensors, Vol. 8, 2006, pp. 347-366.

[54] L. Shu, H. Songling and Z. Wei, ‘Development of differential probes in pulsed eddy current testing for noise suppression’, Sensors and Actuators A, Vol. 135, No. 2, 2007, pp. 675-679.

[55] K. Tsukada and T. Kiwa, ‘Magnetic property mapping system for analyzing three-dimensional magnetic components’, Review of Scientific Instruments, Vol. 77, 2006, pp. 1-5.

[56] T. Dogaru and S. Smith, ‘Giant magnetorsistance-based eddy current sensor’, IEEE Transactions on Magnetics, Vol. 37, No.5, 2001, pp. 3831-3838.

[57] M.V. Kreutzbruck and K. Allweins, ‘High field resolution for nondestructive testing using sensitivity magnetometers’, Sensors and Actuators A, Vol. 101, 2002, pp. 85-91.

[58] A. Sophian, G.Y. Tian, D. Taylor and J. Rudlin, ‘A feature extraction technique based on principle component analysis for pulsed eddy current NDT’, NDT & E International, Vol. 36, 2003, pp. 37-41.

[59] J.T. Jeng, H.E. Horng and H.C. Yang, ‘Detection of small cracks using high-Tc SQUIDSs in an unshielded environment’, Superconductor Science and Technology, Vol. 15, 2002, pp. 416-420.

[60] A. Sophian, G.Y. Tian, D. Taylor and J. Rudlin, ‘A feature extraction technique based on principle component analysis for pulsed eddy current NDT’, NDT & E International, Vol. 36, 2003, pp. 37-41.

[61] G.Y. Tian and A. Sophian, ‘Reduction of lift-off effect for pulsed eddy current NDT’, NDT & E International, Vol. 38, No. 4, 2005, pp. 319-324.

[62] H. Huang, N. Sakurai, T. Tagaki and T. Uchimoto, 'Design of an eddy current array probe for crack sizing in steam generator tubes', NDT & E International, Vol. 36, No. 7, 2003, pp. 515-522.

[63] R. Grimberg, L. Udpa, A. Savin, R. Steigman, V. Palihovici and S. Udpa, '2D eddy current sensor array', NDT & E International, Vol. 39, No.4, 2006, pp. 264-271.

[64] G. Panaitov, H.J. Krause and Y. Zhang, 'Pulsed eddy current transient technique with HTS SQUID magnetometer for nondestructive evaluation', Physica C, Vol. 372-376, Part 1, 2002, pp. 278-281.

[65] C.V. Dodd and W.E. Deeds, 'Analytical solutions to eddy current probe-coil problems', Journal of Applied Physics, Vol. 39, No. 6, 1968, pp. 2829-2838.

[66] J.W. Luquire, W.E. Deeds and C.V. Dodd, 'Alternating current distribution between planar conductors', Journal of Applied Physics, Vol. 41, No. 10, 1970, pp. 3983-3993.

[67] N. Harfield and J.R. Bowler, 'Theory of thin-skin eddy current interaction with surface cracks', Journal of Applied Physics, Vol. 82, No. 9, 1997, pp. 4590-4603.

[68] J.R. Bowler and N. Harfield, 'Evaluation of probe impedance due to thin-skin eddy current interaction with surface cracks', IEEE Transactions on Magnetics, Vol. 34, No. 2, 1998, pp. 515-523.

[69] T.P. Theodoulidis and J. Bowler, 'Eddy-current interaction of a long coil with a slot in a conductive plate', IEEE Transactions on Magnetics, Vol. 41, No. 4, 2005, pp. 1238-1247.

[70] S. Paillard, G. Pichenot, M. Lambert, H. Voillaume and N. Dominguez, 'Modelling of flawed riveted structures for EC inspection in aeronautics', Review of Quantitative Nondestructive Evaluation, Vol. 27, 2008, pp. 579-586.

[71] D. Premel, G. Pichenot T. Sollier, 'Development of a 3D electromagnetic model for eddy current tubing inspection: application to the simulation of probe eccentric, International Journal of Applied Electromagnetic and Mechanics, Vol. 18, 2003, pp. 1-5.

[72] G. Pichenot, D. Premel and G. Cattiaux, 'Eddy current modelling for the nuclear industry: an overview of the CIVA simulation software features', Proceedings of the 5th International Conference on NDE in Relation to Structural Integrity for Nuclear and Pressurized Components, 2006.

[73] S.K. Burke, T.P. Theodoulidis, 'Impedance of a horizontal coil in a borehole: a model for eddy current bolthole probes', Journal of Physics D: Applied Physics, Vol. 37, No. 3, 2004, pp. 485-494.

[74] J.M. Jin, 'The finite element method in Electromagnetics', Wiley-IEEE Press, ISBN 0471438189, 2002.

[75] G.D. Smith, 'Numerical solution of partial differential equations', Oxford University Press, ISBN 0198596111, 1969.

[76] D.Z. Chen, K. R. Shao, J. D. Lavers, 'A very fast numerical analysis of benchmark models of eddy current testing for steam generator tube', IEEE Transactions on Magnetics, Vol. 38, No. 5, 2002, pp. 2355-2362.

[77] B. Klimpke, ‘A hybrid magnetic field solver using combined finite element/boundary element field solver’, presented at the UK Magnetics Society Conference, 2003, pp. 1-8.

[78] R.V. Sabariego, J. Gyselinck, P. Dular, W. Legros, ‘Application of the fast multipole method to hybrid finite element-boundary element models’, Journal of Computational and Applied Mathematics, Vol. 168, No. 1-2, 2004, pp. 403-412.

[79] L. Xuan, Z.W. Zeng, B. Shanker and L. Udpa, ‘Meshless method for numerical modelling of pulsed eddy currents’, IEEE Transactions on Magnetics, Vol. 40, No. 6, 2004, pp. 3457-3462.

[80] L. Xuan, W. Zheng, B. Shanker and L. Udpa, ‘Element-Free Galerkin Method for static and quasi-static electromagnetic field computation’, IEEE Transactions on Magnetics, Vol. 40, No. 1, 2004, pp. 12-20.

[81] B.A. Auld and J.C. Moulder, ‘Review of advances in quantitative eddy current non-destructive evaluation’, Journal of Nondestructive Evaluation, Vol. 18, No. 1, 1999, pp. 3-36.

[82] X.W. Dai, R. Ludwig and R. Palanisamy, ‘Numerical simulation of pulsed eddy-current non-destructive testing phenomena’, IEEE Transactions on Magnetics, Vol. 26, No.6, 1990, pp. 3089-3096.

[83] G. Katragadda, Y.S. Sun, W. Lord, Y.S. Sun, S. Udpa and L. Udpa, ‘Velocity effects and their minimisation in MFL inspection of pipelines – a numerical study’, Review of Progress in QNDE, Vol. 14, 1995, pp. 499-505.

[84] Y. Tian, Y. Li, Z. Zeng, L. Udpa and S. Udpa, ‘Simulation of the world federation’s first eddy current benchmark problem, 30th Annual review of Progress in Quantitative Nondestructive Evaluation (QNDE 2003), 2003, pp. 1560-1566.

[85] Y. Tian, Y. Li, Z. Zeng, L. Udpa and S. Udpa, ‘Simulation of the world federation’s first eddy current benchmark problem, 30th Annual review of Progress in Quantitative Nondestructive Evaluation(QNDE 2002, 2002, pp. 1816-1823.

[86] C.F. Ma, ‘A finite-element approximation of quasi-magnetostatic 3D eddy current model by fractional-step’, Mathematical and Computer Modelling, Vol. 39, No. 4-5, 2004, pp. 567-580.

[87] H. Tsuboi, N. Seshima, I. Sebestyen, J. Pavo, S. Gyimothy and A. Gasparics, ‘Transient eddy current analysis of pulsed eddy current by finite element method’, IEEE Transactions on Magnetics, Vol. 40, No.2, 2004, pp. 1330-1333.

[88] COMSOL, http://www.comsol.com/, Accessed February 2010.

[89] Infolytica Corporation, http://www.infolytica.com/en/products/magnet/, Accessed February 2010.

[90] L. R. Turner, ‘3-D field computation: The near-triumph of commercial codes’, IEEE Transactions on Magnetics, Vol. 32, No. 4, 1996, pp. 2945-2949.

[91] F. Al-naemi, ‘Magnetic FEM and NDT: Benefits, pitfalls and applications’, Proceedings of Magnetics in Non-Destructive Testing, 2005, pp. 8-14.

[92] F. Luo, Y. He and B. Yang, 'Array pulsed eddy current imaging technique for nondestructive testing of aging aircraft', 17th World Conference on Nondestructive Testing, China, 2008.

[93] R. Smith and D. Edgar, 'Advances in transient eddy-current imaging for aerospace applications', World Conference on NDT, Montreal, Canada, 2004.

[94] A. Jeremic and A. Nehorai, 'Design of chemical sensor arrays for monitoring disposal sites on the ocean floor', IEEE Journal of Oceanic Engineering, Vol. 23, No. 4, 1998 pp. 334-343.

[95] R. Grimberg, L. Udpa, A. Savin, R. Steigmann, V. Palihovici, and S. Udpa, '2D eddy current sensor array', NDT & E International, Vol. 39, No. 4, 2006, pp. 264-271.

[96] N. Goldfine, V. Zilberstein, A. Washabaugh, D. Schlicker, I. Shay and D. Grundy, 'Eddy current sensor networks for aircraft fatigue monitoring', Materials Evaluation, Vol. 61, No. 7, 2003, pp. 852-859.

[97] V. Zilberstein, D. Grundy, V. Weiss, N. Goldfine, E. Abramovici, J. Newman, and T. Yentzer, 'Early detection and monitoring of fatigue in high strength steels with MWM-Arrays', International Journal of Fatigue Damage of Structural Materials V, Vol. 27, No. 10-12, 2005, pp. 1644-1652.

[98] C.H. Smith, R.W. Schneider, T. Dogaru and S.T Smith, 'Eddy-current testing with GMR magnetic sensor arrays', Review of Progress in Quantitative Nondestructive Evaluation, Vol. 23, No. 2, 2003, pp. 406-413.

[99] R. A. Smith and G. R. Hugo, 'Transient eddy current NDE for ageing aircraft - capabilities and limitations', Insight, Vol. 43, No. 1, 2001, pp. 14-25.

[100] S. Yamasa, K. Chomsuwan, T. Hagino, 'Conductive microbead array detection by high-frequency eddy-current testing technique with SV-GMR sensor', IEEE Transactions on Magnetics, Vol. 41, 205, pp. 3622-3624.

[101] NVE Corporation, GMR sensors data book, http://www.cs.cmu.edu/~sensing-sensors/readings/GMR_magnetic_sensor_databook.pdf, Accessed December 2009.

[102] Y. Li, G.Y. Tian and T. Theodoulidis, 'Fast analytical method for pulsed eddy current evaluation', Proceedings of the 45th annual British conference on NDT, 2006, pp. 1-12.

[103] G. Yang, A. Tamburrino, L. Udpa, S.S. Udpa, Z. Zheng, Y. Deng and P. Que, 'Pulsed eddy-current based giant magnetoresistive system for the inspection of aircraft structures' IEEE Transactions on Magnetics, Vol. 46, No. 3, 2010, pp. 910-917.

[104] K. Thiyagarajan, B. Maxfield, K. Balasubramaniam and C.V. Krishnamurthy, 'Pulsed eddy current digital imaging of corrosion pits', Journal of Nondestructive Testing & Evaluation, Vol. 7, No. 2, 2008, pp. 32-36.

[105] R.S. Edwards, A. Sophian, S. Dixon, G.Y. Tian and X. Jian, 'Dual EMAT and PEC non-contact probe: applications to defect testing', NDT & E International, Vol. 39, 2006, pp. 45-52.

[106] S. Mandayam, R. Polikar and J.C. Chen, 'A data fusion system for the nondestructive evaluation of non-piggable pipes', retrieved August 2008,

National Energy Technology Laboratory website, http://www.netl.doe.gov/technologies/oil-gas/publications/td/NT41648_Final.pdf.

[107] J.W. Wilson, G.Y. Tian, V. Moorthy and B. A. Shaw, ‘Magneto-acoustic emission and magnetic barkhausen emission for case depth measurement in En36 gear steel’, IEEE Transactions on Magnetics, Vol. 45, No. 1, 2009, pp. 177-183.

[108] A. Sophian, G.Y. Tian and S. Zairi, ‘Pulsed magnetic flux leakage techniques for crack detection and characterisation’, Sensors and Actuators A, Vol. 125, 2006, pp. 186-191.

[109] J.W. Wilson and G.Y. Tian, ‘Pulsed electromagnetic methods for defect detection and characterisation’, NDT & E International, Vol. 40, 2007, pp. 275-283.

[110] C. Meola, ‘Nondestructive Evaluation of Materials With Rear Heating Lock-In Thermography’, Sensors Journal, IEEE, Vol. 7, No. 10, 2007, pp. 1388 – 1389.

[111] S. Pickering and D. Almond, ‘Matched excitation energy comparison of the pulse and lock-in thermography NDE techniques’, NDT & E International, Vol. 41, No. 7, 2008, pp. 501-509.

[112] T.J. Ahmed, D. Stavrov, H.E.N. Bersee and A. Beukers, ‘Induction welding of thermoplastic composites—an overview’, Composites Part A: Applied Science and Manufacturing, Vol. 37, No. 10, 2006, pp. 1638-1651.

[113] C. Meola, G. M. Carlomagno, L. Giorleo, ‘The use of infrared thermography for materials characterization’, Journal of Materials Processing Technology, Vol. 155-156, No. 30, 2004, pp. 1132-1137.

[114] B. Oswald-Tranta, ‘Thermoinductive investigations of magnetic materials for surface cracks’, Quantitative Infra Red Thermography Journal, Vol. 1, 2004, pp. 33-47.

[115] G. Riegert, Th. Zweschper, and G. Busse, ‘Lock-in thermography with eddy-current excitation’, Quantitative Infra Red Thermography Journal, Vol. 1, 2004, pp. 21-32.

[116] G. Zenzinger, J. Bamberg, W. Satzger and V. Carl, ‘Thermographic cracks detection by eddy current excitation’, Nondestructive Testing and Evaluation, Vol. 22, No. 2-3, 2007, pp. 101-111.

[117] N. Tsopelas, N.J. Siakavellas, ‘The effect of the angle of inclination of the exciting coil in electromagnetic-thermal non-destructive inspection’, HSNDT 2007.

[118] J. Rantala, D. Wu, G. Busse, ‘Amplitude Modulated Lock-In Vibrothermography for NDE of Polymers and Composites’, Research in Nondestructive Evaluation, Vol. 7, 1996, pp. 215-218.

[119] T. Zweschper, A. Dillenz, G. Riegert, D. Scherling, G. Busse, ‘Ultrasound excited thermography using frequency modulated elastic waves’, Insight, Vol. 45, 2003, pp. 178-182.

[120] J. Rantala, D. Wu, G. Busse, ‘NDT of polymer materials using lock-in thermography with water-coupled ultrasonic excitation’, NDT & E International, Vol. 31, No. 1, 1998, pp. 43-49.

[121] D. Wu, Th. Zweschper, A. Salerno, and G. Busse, ‘Lock-in Thermography for Nondestructive Evaluation of Aerospace Structures’, ECNDT, Copenhagen, Denmark, 1998.

[122] N.P. Avdelidis, D.P. Almond, ‘Transient thermography as a through skin imaging technique for aircraft assembly: modelling and experimental results’, Infrared Physics & Technology, Vol. 45, Issue 2, 2004, pp. 103-114.

[123] N.P. Avdelidis, D.P. Almond, A. Dobbinson, B.C. Hawtin, C. Ibarra-Castanedo, X. Maldague, ‘Aircraft composites assessment by means of transient thermal NDT’, Progress in Aerospace Sciences, Vol. 40, Issue 3, 2004, pp. 143-162.

[124] N.P. Avdelidis, D.P. Almond, ‘Through skin sensing assessment of aircraft structures using pulsed thermography’, NDT & E International, Vol. 37, Issue 5, 2004, pp. 353-359.

[125] M. Genest, M. Martinez, N. Mrad, G. Renaud, A. Fahr, ‘Pulsed thermography for non-destructive evaluation and damage growth monitoring of bonded repairs, Composite Structures’, In Press, Available online 19 February 2008.

[126] S.M. Shepard and M. Yamada, ‘Recent advances in pulsed thermography’, Proceedings of JSNDI Conference, Vol. 2004, 2004, pp. 151-152.

[127] T. J. Barden, D. P. Almond, M. Morbidini, P. Duffour and P. Cawley, ‘A quantitative investigation of Thermosonics’, WCNDT, Montreal, Canada, 2004.

[128] X. Han, L.D. Favro, Z. Ouyang, and R.L. Thomas, ‘Thermosonics: Detecting cracks and adhesion defects using ultrasonic excitation and infrared imaging’, The Journal of adhesion, Vol. 76, No. 2, 2001, pp. 151-183.

[129] G. Walle and U. Netzelmann, ‘Thermographic crack detection in ferritic steel components using inductive heating’, ECNDT, Berlin, Germany, 2006.

[130] G. Zenzinger, J. Bamberg, M. Dumm, P. Nutz, ‘Crack detection using EddyTherm’, Review of Progress in Quantitative Nondestructive Evaluation, AIP Conference Proceedings, Vol. 760, 2005, pp. 1646-1653.

[131] J. Bamberg, W. Satzger, and G. Zenzinger, ‘Optimized image processing for eddy current thermography’, Review of Progress in QNDE, Vol. 25A, 2005, pp.708-712.

[132] Y Li, T. Theodoulidis, G. Y. Tian, ‘Magnetic field based multi-frequency eddy current for multilayered specimen characterisation’, IEEE Transactions on Magnetics, Vol. 43, No. 11, 2007, pp. 4010-4015.

[133] Honeywell International, 1- and 2- axis magnetic sensors, http://www.honeywell.com/sites/servlet/com.merx.npoint.servlets.DocumentServlet?docid=D5169116C-67A8-D99E-0995-FAD409AFC81D , Accessed December 2009.

[134] J. Wang, G.Y.Tian, A. Simm and G.P. Lucas, ‘Simulation of magnetic field distribution of excitation coil for EM flow meter and its validation using magnetic camera’, 17th World Conference on Nondestructive Testing, Shanghai, China, 2008.

[135] J. Vrana, M. Goldammer, J. Baumann, M. Rothenfusser and W. Arnold, ‘Mechanisms and models for crack detection with induction thermography’, Review of Quantitative Nondestructive Evaluation, Vol. 27, 2008, pp. 475-482.

[136] C.N. Kumar, C.V. Krishnamurthy, B.W. Maxfield and K. Balasubramaniam, ‘Tone burst eddy-current thermography (TBET)’, Review of Quantitative Nondestructive Evaluation, Vol. 27, 2008, pp. 544-551.

[137] B. Owald-Tranta, ‘Thermo-inductive crack detection’, Nondestructive Testing and Evaluation, Vol. 22, 2007, pp. 137-153.

[138] A.M. Lewis, D.H. Michael, M.C. Lugg and R. Collins, 'Thin-skin electromagnetic fields around surface-breaking cracks in metals', J. Appl. Phys. Vol. 64, No. 8, 1988, pp. 3777-3784.

[139] G. Wally and B. Oswald-Tranta, ‘The influence of crack shapes and geometries on the results of the thermo-inductive crack detection’, Thermosense XXIX, Proceedings of the SPIE, Vol. 6541, 2007, pp. 11-19.

[140] J.G. Sun, ‘Analysis of pulsed thermography methods for defect depth prediction’, Journal of Heat Transfer, Vol. 28, 2006, pp 329-338.

[141] D.F. Cannon and H. Pradier, ‘Rail rolling contact fatigue research by the European Rail Research Institute’, Wear, Vol. 191, 1996, pp 1-13.

[142] Y. Fan, S. Dixon, R.S. Edwards and X. Jian, ‘Ultrasonic surface wave propagation and interaction with surface defects on rail track head’, NDT&E International, Vol. 40, Feb 2007, pp. 471-477.

[143] R.S. Edwards, Y. Fan, M. Papaelias, S. Dixon, C.L. Davis and C. Roberts, ‘Ultrasonic detection of surface-breaking railhead defects’, Review of Quantitative Nondestructive Evaluation, Vol. 27, 2008, pp. 602-609.

[144] M.C. Dubourg, V. Lamacq, ‘A predictive rolling contact fatigue crack growth model: onset of branching, direction and growth-role of dry and lubricated conditions on crack patterns’, ASME Journal of Tribology, Vol. 124, 2002, pp. 680-688.

[145] L.U. Chao, T.U. Zhan-Kuan, C. Jian-Jun and L. Lian-Xiu, ‘RCF damage characteristics of high-speed railway rail and research development of NDT techniques’, Failure Analysis and Prevention, Vol. 1, 2009.

[146] D. Hesse and P. Cawley, ‘Excitation of surface waves modes in rails and their application for defect detection’, AIP Conference Proceedings, Vol. 820, 2006, pp. 1593-1600.

[147] Innotrack, ‘Report on rail inspection technologies, http://www.innotrack.net/IMG/pdf/d441.pdf, 2008, Accessed October 2010.

[148] D.F. Cannon, K.O. Edel, S.L. Grassie and K. Sawley, ‘Rail defects: an overview’, Fatigue & Fracture of Engineering Materials & Structures, Vol. 26, 2003, pp. 865-886.

[149] R.S. Edwards, S. Dixon and X. Jian, ‘Characterisation of defects in the railhead using ultrasonic surface waves’, NDT & E International, Vol. 39, Issue 6, 2006, pp. 468-475.

[150] C.M. Lee, J.L. Rose and Y. Cho, ‘A guided wave approach to defect detection under shelling in rail’, NDT & E International, Vol. 42, Issue 3, 2009, pp. 174-180.

[151] R. Pohl, A. Erhard, H.J. Montag, H.M. Thomas and H. Wustenberg, ‘NDT techniques for railroad wheel and gauge corner inspection’, NDT & E International, Vol. 37, Issue 2, 2004, pp. 89-94.

[152] M.P. Papelias, M.C. Lugg, C. Roberts and C.L. Davis, ‘High-speed inspection of rails using ACFM techniques’, NDT & E International, Vol. 42, Issue 4, 2009, pp. 328-335.

[153] TSC Inspection Systems, ‘The ACFM walking stick information pack’, http://www.tscinspectionsystems.co.uk/pdfdocs/ACFMWalkingStickInformationPack.pdf

[154] S.M. Dixon, R.S. Edwards and X. Jian, ‘New instrumentation for the scientific study of rail defects: Final report summary’, EPSRC grant number EP/C534808/1.

[155] S. Yang, G.Y. Tian, I.Z. Abidin and J. Wilson, ‘Simulation of edge cracks using pulsed eddy current stimulated thermography’, Journal of Dynamic Systems, Measurement and Control, Vol. 133, 2011, pp. 011008-1 - 011008-6.

List of publications

Journal papers

1. I.Z. Abidin, G.Y. Tian, J. Wilson, S. Yang and Darryl Almond, ‘Quantitative evaluation of angular defects by pulsed eddy current thermography’, accepted for publication in NDT&E International.
2. S. Yang, G.Y. Tian, I.Z. Abidin and J. Wilson, ‘Simulation of edge cracks using pulsed eddy current stimulated thermography’, submitted to be published in Measurement Science and Technology.
3. J. Wilson, G.Y. Tian, I.Z. Abidin, S. Yang and D.P. Almond, ‘Modelling and evaluation of eddy current stimulated thermography’, Nondestructive Testing and Evaluation, 2010.
4. J. Wilson, G. Y. Tian, I. Z. Abidin, S. Yang and D. Almond, ‘Pulsed eddy current thermography: system development and evaluation’, Insight, Vol. 52, No., 2010, pp. 87-90.
5. I.Z. Abidin, C. Mandache, G.Y. Tian and M. Morozov, ‘Pulsed eddy current testing with variable duty cycle on rivets joints’, NDT & E International, Vol. 42, No. 7, 2009, pp. 599-605.
6. I.Z. Abidin, C. Mandache, G.Y. Tian and Y. Li, ‘Defect depth estimation using pulsed eddy current with varied pulsed width excitation’ Insight, Vol. 51, No. 2, 2009, pp. 69-72.
7. I. Z. Abidin, G. Y. Tian and Y. Li, ‘3D transient magnetic field mapping for angular slots in aluminium’, Insight, Vol. 51, No.1, 2009, pp. 21-24.

Conference papers

1. I.Z. Abidin, G.Y.Tian, J. Wilson, S. Yang and D. Almond, ‘Quantiative evaluation of angular defects by pulsed eddy current thermography’, presented at the 48th Annual Conference of the British Institute for Non-Destructive Testing, Blackpool, UK, 2009.
2. I.Z. Abidin, G.Y. Tian and Y. Li, ‘Magnetic field mapping for complex geometry defect – 3D transient problem’, presented at the 17th World Conference on Non-Destrictive Testing, Shanghai, China, 2008.
3. I.Z. Abidin, C. Mandache, G.Y. Tian and Y. Li, ‘Defect depth estimation using pulsed eddy current with varied pulse width excitation’, presented at the 47th Annual Conference of the British Institute for Non-Destructive Testing, Cheshire, UK, 2008.
4. I.Z. Abidin, G.Y. Tian and Y. Li, ‘Simulation of complex geometry defect characterisation by using PEC sensor array’, presented at the 46th Annual Conference of the British Institute for Non-Destructive Testing, Galsgow, Scotland, 2007.

Appendices

Appendix A: Modelling of PEC via MagNet

Appendix A provides the details and descriptions of the modelling and simulations for PEC conducted in MagNet.

MagNet is a numerical simulation software for static or time-varying electromagnetic fields analysis. MagNet implements FEM for an accurate and quick solution to Maxwell's equations. Each module in MagNet is tailored to simulate different types of electromagnetic fields for applications such as machines, sensors and transformers either in time-harmonic or transient solver. The following will provide the procedures and steps taken for the modelling and simulation of PEC by MagNet. These procedures and steps are based on the instruction manual provided by MagNet.

A.1 Geometry modelling

Taking into consideration the symmetrical geometry of the problem, the domains are modelled as a half model. The *Cartesian* coordinate system is used to specify the coordinates for the drawing of the domains. The 3D geometries for the model are created by modelling 2D cross sections in the drawing plane and the components are then extruded to 3D objects. Figure A1 shows the geometries of a square coil and sample having angular defects created in the 2D work planes which are then extruded to 3D objects.

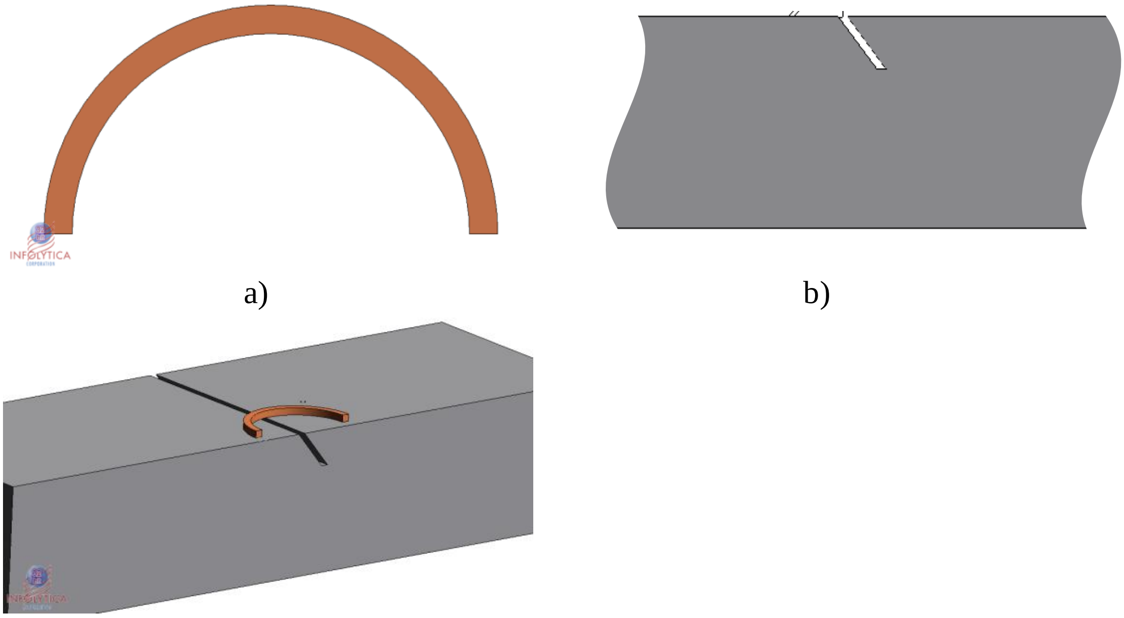

a) b)

c)

Figure A1: Drawing of the half models for a) coil in 2D, b) sample in 2D, and c) extrusion to 3D objects

It is necessary to specify a finite volume to mesh and solve for since it is not affordable to mesh and infinite volume due to the computation limitation in terms of memory. Therefore, the model is truncated into a finite region by defining an external boundary model which limits the solutions to be calculated inside the assigned region. Figure A2 shows the boundary region assigned to the model.

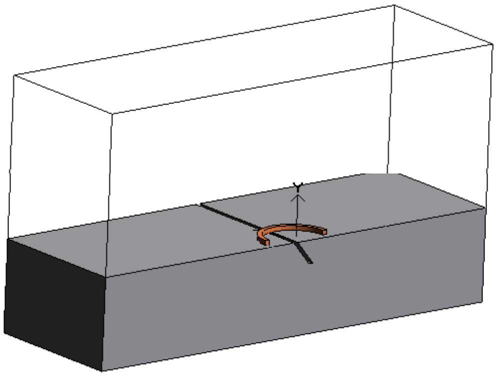

Figure A2: External boundary region for the model

A2. Component settings

The descriptions and settings for the components in the model are defined in this step. The component to be defined i.e. sample, coil and external boundary; is selected and the material for the component is assigned in the *Material* menu. This will assigned the electrical constants parameters of the material to the selected component. The properties to be assigned for the coil are defined at the *Coil Properties* page. Here the current or voltage amplitude, coil number of turns and the waveform for the excitation are defined to be used in the simulation.

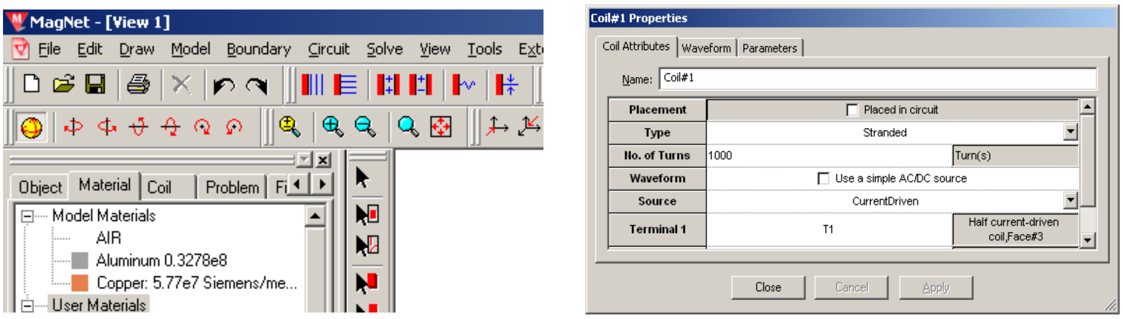

Name: Coil#1

Placement	☐ Placed in circuit	
Type	Stranded	
No. of Turns	1000	Turn(s)
Waveform	☐ Use a simple AC/DC source	
Source	CurrentDriven	
Terminal 1	T1	Half current-driven coil,Face#3

a) b)

Figure A3: Components settings for a) Domains in the model, and b) Coil properties

The boundary conditions for the domains of the model are assigned by selecting the *Boundary* menu. Since the domains are modelled as a half model, the *Odd Periodic* boundary condition is applied at the median plane to define the symmetry condition. The external boundary is assigned the *Field Normal* boundary condition which limits the extent of the field to be solved inside the assigned boundaries. The *Flux Tangential* boundary condition is applied to the rest of the domains to allow continuous magnetic field flow at the domains boundaries.

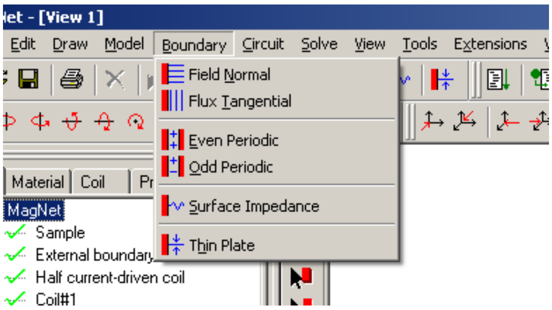

Figure A4: Assigning boundary conditions for the domains in the model in the Boundary menu

A3. Mesh generation

The mesh of each domain can be assigned at the *Object Properties* in the *Mesh* submenu as shown in Figure A5a. The model is divided into mesh of tetrahedral-shaped elements. In order to get good accuracy from the 3D simulation, a fine mesh is generated within the region of interest. The sample which is the important domain where the interaction of magnetic fields occurs is set at a more refine mesh. This will enhanced the mesh quality around the defect area and the region where the direction or the magnitude of the magnetic field is changing rapidly. Figure A5b illustrate the mesh conditions applied to the model. The figure shows the refinement of the mesh quality at the area of interest; which is directly beneath the induction coil and around the defect area.

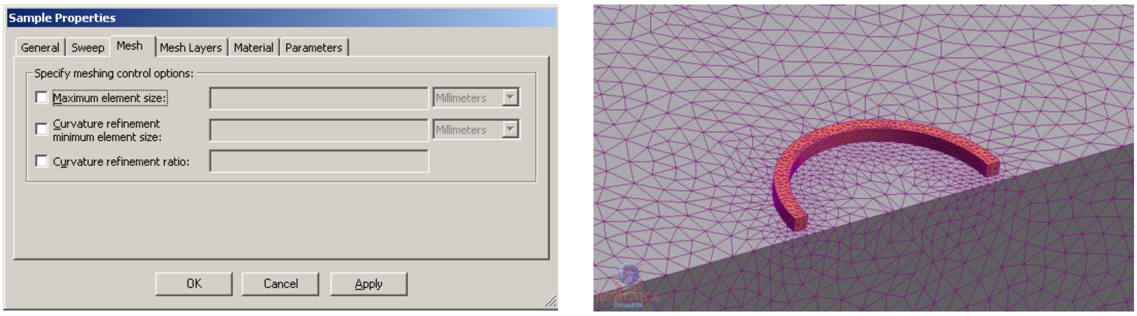

Specify meshing control options:
☐ Maximum element size: Millimeters
☐ Curvature refinement minimum element size: Millimeters
☐ Curvature refinement ratio:

a) b)

Figure A5: Mesh generation for the domains; a) Mesh submenu for assigning the mesh to the domains, and b) Mesh generation of the 3D model

A4. Computing the solution

The time stepping method must be set before the transient solution is initiated. The time steps for the output are set at the *Transient Options* in the *Solve* menu as shown in Figure A6a. This is where the time interval for the solution is assigned, in which the solution will be given for every time steps assigned. After these settings and values have been assigned, the simulation can begin to start by clicking the *Transient 3D* (see Figure A6b) in the *Solve* menu.

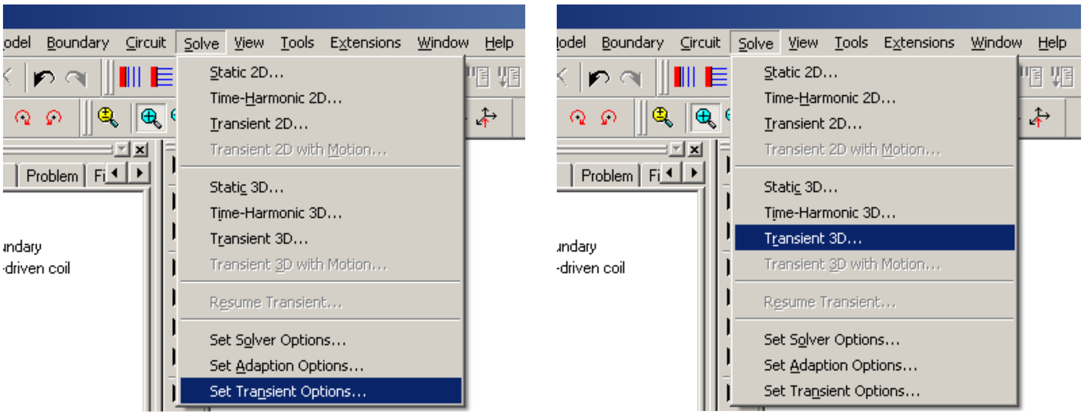

a) b)

Figure A6: a) Setting the time steps in the Transient Options submenu, b) Computing the solution in Transient 3D mode

A5. Viewing the solution results

After the simulation has been solved, the display of the solution can be obtained by selecting the *Field* menu as shown in Figure A7a. The field is chosen by specifying the field name and the Problem ID. The solutions can also be displayed in the form of a graph by using the *Field Sampler* in *the Extensions* menu (see Figure A7b). This will provide numerical data for further post processing for analysis.

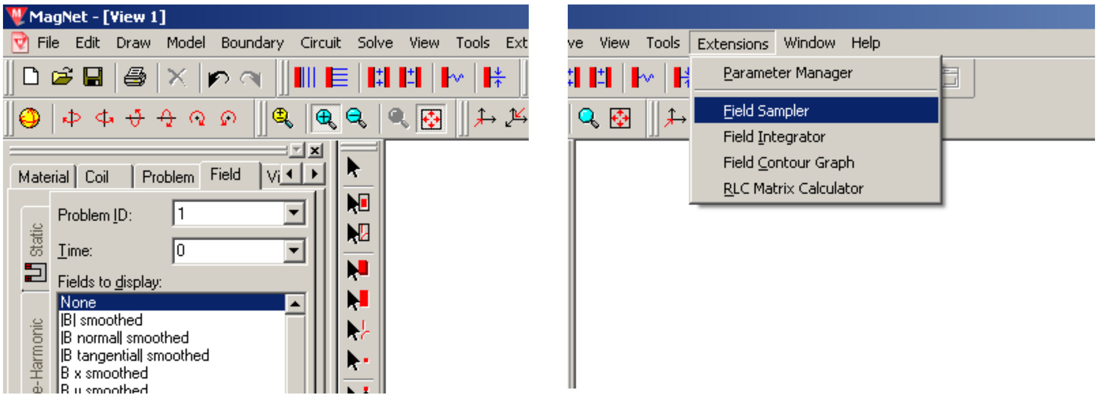

Problem ID: 1
Time: 0

a) b)

Figure A7: Viewing the solution results using a) The Field menu, and b) Field Sampler menu

Appendix B: Modelling of PEC thermography via COMSOL multiphysics

Appendix B provides the details and descriptions of the modelling and simulations for PEC conducted in COMSOL.

COMSOL Multiphysics is a multiphysics modelling package for numerical simulation of the physical process, which can be described using partial differential equations (PDEs). State-of-the-art solvers are embedded in the package for the user to choose, to address complicated problems quickly and accurately. It contains specific modules for different applications, which involve Chemical Engineering, Earth Science, Heat Transfer, Micro-electromechanical system (MEMS), Structural Mechanics and Electromagnetics. The following will provide the procedures and steps taken for the modelling and simulation of PEC thermography by COMSOL. These procedures and steps are based on the instruction manual provided by COMSOL.

B1. Model navigator

The modelling of PEC thermography is conducted in 3D environment. Therefore 3D is selected in the space dimension of the model navigator. For PEC thermography, multiphysics capability is required to solve induction current and heat transfer simultaneously. Hence, *AC/DC Module* > *Electro-Thermal Interaction* > *Induction Heating* > *Transient analysis* multiphysiscs mode is chosen as shown in figure B1. This module will specify the simulation for the induction heating phenomena which PEC thermography is based on.

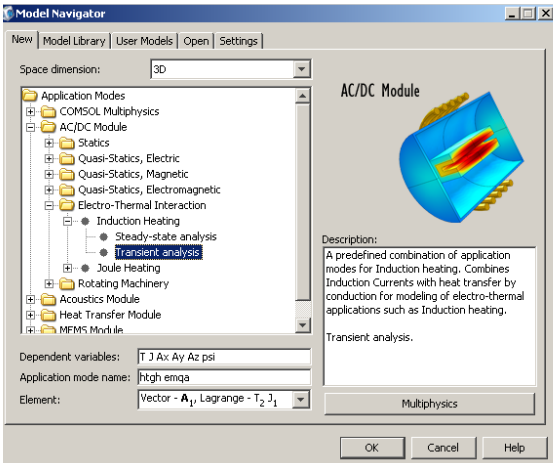

Space dimension: 3D

Dependent variables: T J Ax Ay Az psi

Application mode name: htgh emqa

Element: Vector - $\mathbf{A}_1$, Lagrange - T_2 J_1

Description:

A predefined combination of application modes for Induction heating. Combines Induction Currents with heat transfer by conduction for modeling of electro-thermal applications such as Induction heating.

Transient analysis.

Figure B1: Module selected for PEC thermography simulations

B2. Options and settings

The constants used in the simulation describing the parameters of the main components in the model are assigned in the constants dialog box from the *Options* > *Constants*, menu as shown in Figure B2. Table B1 provides the descriptions and value of the constants to be used with the model for a PEC thermography simulation. These values will be assigned later to the respective domains in the physics modelling.

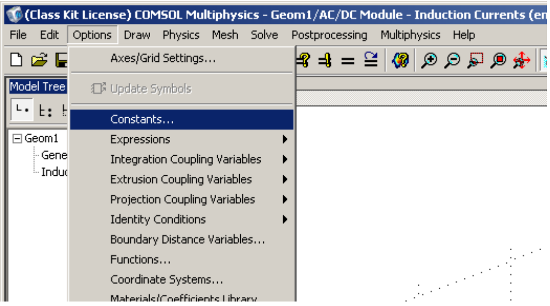

Figure B2: Defining the constants used in the simulation in the Option menu

Table B1: Constants dialog box

Name	Expression	Description
I0	350[A]	Current
diam	12.7e-3[m]	Diameter
circ	pi*diam	Circumference
Js0	I0/circ	Surface current density
T0	293[K]	Reference temperature
r0	2.65e-8[ohm*m]	Resistivity at T = T0

alpha	2.31e-5[1/K]	Temperature coefficient
rho1	2700[kg/m^3	Density of aluminium
rho2	1.2051[kg/m^3]	Density of air
rho3	8700[kg/m^3]	Density of copper
Cp1	897[J/(kg*K)]	Heat capacity of aluminium
Cp2	1.005e3[J/(kg*K)]	Heat capacity of air
Cp3	385[J/(kg*K)]	Heat capacity of copper
k1	237[W/(m*K)]	Thermal conductivity of aluminium
k2	0.0257[W/(m*K)]	Thermal conductivity of air
k3	400[W/(m*K)]	Thermal conductivity of copper

B3. Geometry modelling

The 3D geometries for the model is created by modelling 2D cross sections using the CAD tools built into COMSOL and extrude it to a 3D objects. The 2D cross sections are created in local 2D coordinate systems called *work planes*, which can be positioned anywhere in 3D space. A work plane is created in the *Work Plane Settings* dialog box as shown in Figure B3 from the *Draw* menu, and defined in the *Quick* tab page. The *Quick* tab creates work planes that are parallel to the *xy*-, *yz*-, and *zx*-planes, with an optional offset in the *z*-, *x*-, and *y*-direction, respectively.

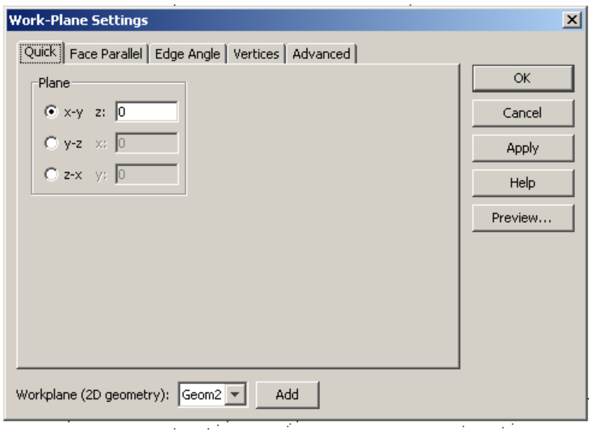

Plane
● x-y z: 0
○ y-z x: 0
○ z-x y: 0

Workplane (2D geometry): Geom2

Figure B3: Work Plane Settings dialog box for the geometry modelling

Figure B4 shows the geometries of a square coil and sample having angular defects created in the 2D work planes which are then extruded to 3D objects. The extruded objects can be positioned anywhere in a 3D space. An advantage with this approach is that different geometric parts can be connected together to form a more complex geometries.

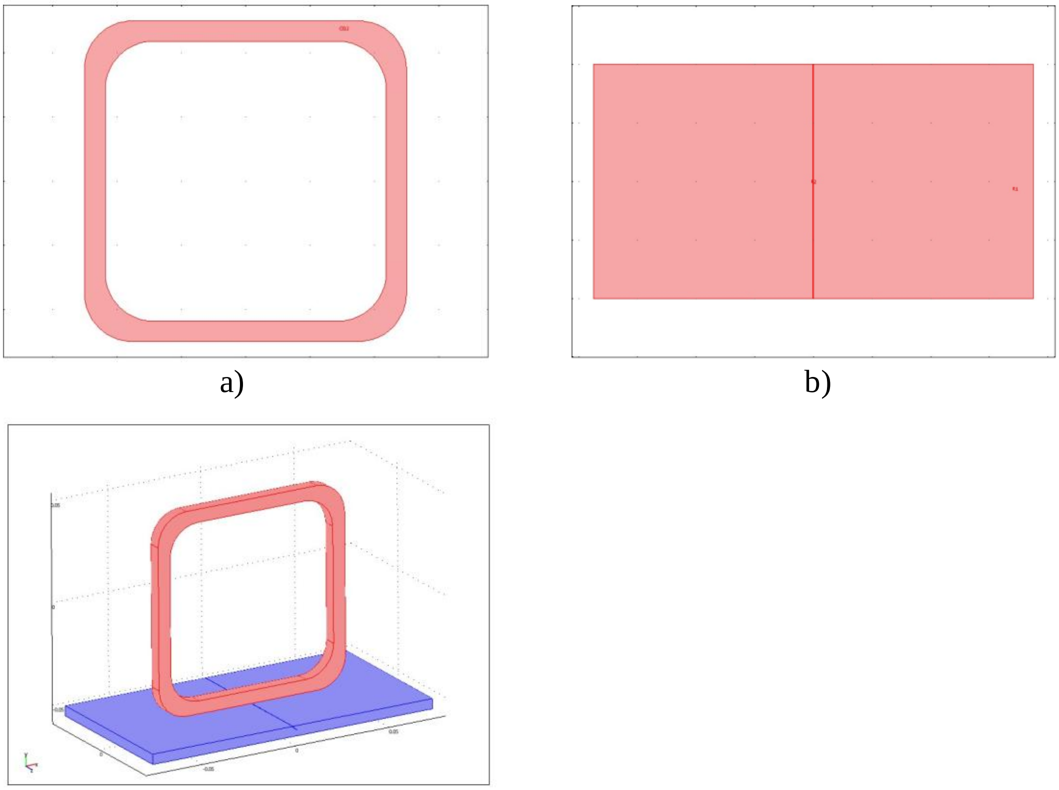

a) b)

c)

Figure B4: Drawing of the models for a) coil in 2D, b) sample in 2D, and c) extrusion to 3D objects

As it is not affordable to mesh an infinite volume, it is necessary to specify a finite volume to mesh and solve for. The model is truncated into a finite region by defining an external boundary model which limits the solutions to be calculated inside the assigned region. Figure B5 shows the boundary region used with the model.

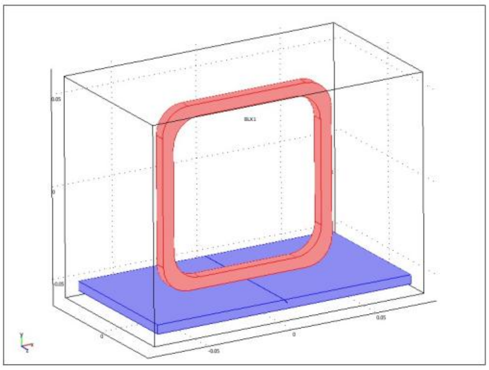

Figure B5: External boundary region for the model

B4. Physics settings

The descriptions and settings for the physics and equations in the model are defined in this step. Since this model involve multiphysics environment, the physics setting has to be assign in both the general heat transfer and induction current phenomena.

The physics setting for the general heat transfer is assigned by selecting General Heat Transfer application mode from the *Multiphysics* menu as shown in Figure B6a. The excitation frequency for the induction coil is set in the *Application Scalar Variables* dialog box (Figure B6b).

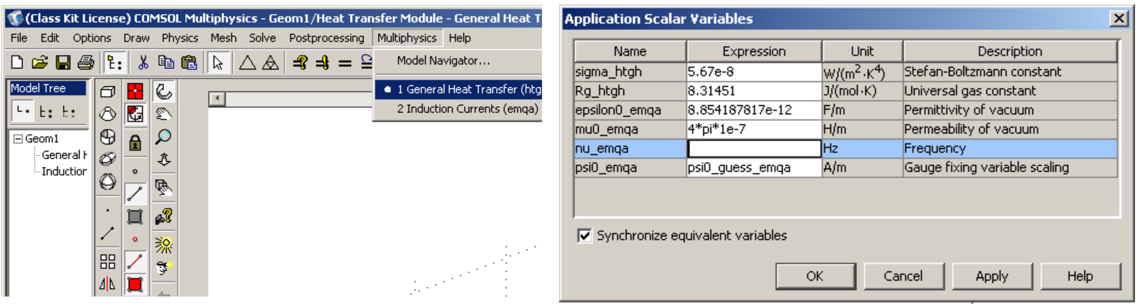

Name	Expression	Unit	Description
sigma_htgh	5.67e-8	W/(m²·K⁴)	Stefan-Boltzmann constant
Rg_htgh	8.31451	J/(mol·K)	Universal gas constant
epsilon0_emqa	8.854187817e-12	F/m	Permittivity of vacuum
mu0_emqa	4*pi*1e-7	H/m	Permeability of vacuum
nu_emqa		Hz	Frequency
psi0_emqa	psi0_guess_emqa	A/m	Gauge fixing variable scaling

☑ Synchronize equivalent variables

a) b)

Figure B6: a) Selecting the mode in multiphysics menu, b) Assigning the excitation frequency for the induction coil

The boundary conditions in the general heat transfer mode for the model are set next in the *Boundary Setting* dialog box as shown in Figure B7a. The external boundaries of the model are set as *Temperature* with T_0 is set as T0. This will define the external boundary to a constant temperature value. The boundary coefficients for the rest of the geometries in the model are set to *Continuity*, to which the flow of magnetic field will be continuous over the boundaries. The constants for the model assigned earlier in the *Constants* menu are assigned to the respective domains in the *Subdomain* menu shown by Figure B7b. In the *Init* tab of the *Subdomain* menu all domains in the model are set to the initial temperature of T0. This will set the initial temperature of all the domains before the heating starts.

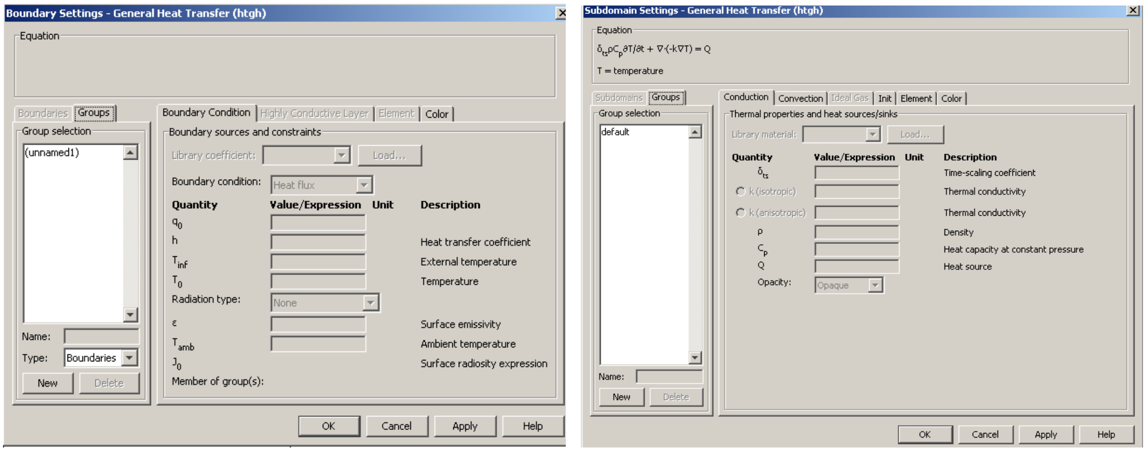

a) b)

Figure B7: Setting the physics and boundary conditions of the domains in the model; a) Boundary settings, and b) Physics settings

The physics setting for the induction currents is assigned next by selecting the induction currents application mode from the *Multiphysics* menu. The external boundaries of the model are set as *Magnetic Insulation* which limits the solutions to be calculated inside the assigned boundaries. For the induction coil, the *Surface Current* boundaries are set at its geometry walls so that the current will flow at the skin of the coil surface. The sample geometries are set to *Continuity* boundary conditions to allow continuous magnetic field flow at its boundaries. The temperature dependant conductivity equation is assigned to the sample in the *Subdomain* menu which gives the dependency of conductivity on temperature change.

B5. Mesh generation

The mesh of each domain can be assigned at the *Free Mesh Parameters* menu as shown in Figure B8a. The model is divided into mesh of tetrahedral-shaped elements. The global mesh for the model are set as coarse. In order to get good accuracy from the 3D simulation, a fine mesh is generated within the region of interest. The sample which is the important domain to visualise the temperature distribution is set at a more refine mesh. This will enhanced the mesh quality around the defect area and the region where the direction or the magnitude of the magnetic field is changing rapidly. The domain for the sample is selected, and it is refined by clicking the refine mesh button. Figure B8b illustrates the mesh conditions applied to the model. The figure shows the refinement of the mesh quality at the area of interest; which is around the defect area and underneath the induction coil.

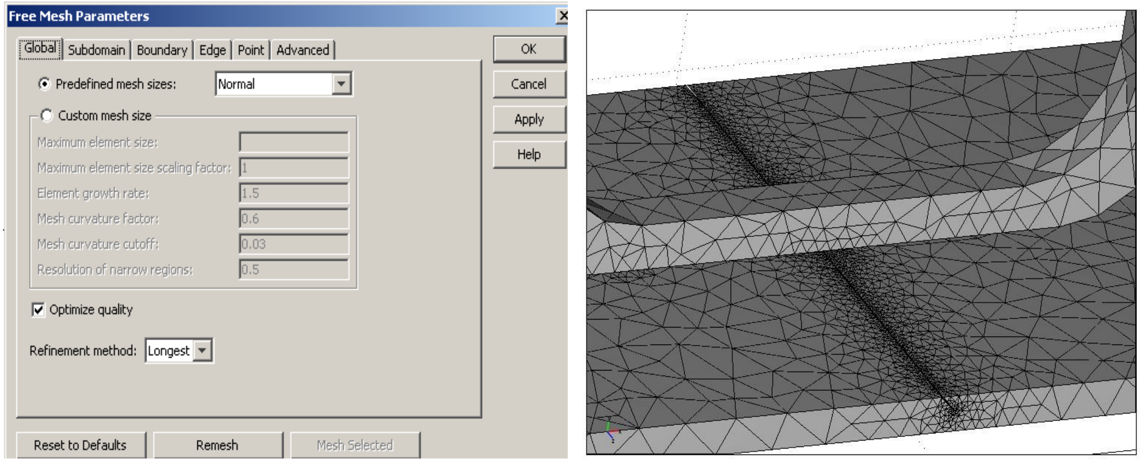

● Predefined mesh sizes: Normal
○ Custom mesh size
Maximum element size:
Maximum element size scaling factor: 1
Element growth rate: 1.5
Mesh curvature factor: 0.6
Mesh curvature cutoff: 0.03
Resolution of narrow regions: 0.5
☑ Optimize quality
Refinement method: Longest

Figure B8: a) Free Mesh Parameters menu, and b) Mesh generation of the 3D model

B6. Computing the solution

The time steps for the output is set at the *Times* edit field of the *Solver Parameters* in the *Solve* menu as shown in Figure B9. This is where the heating period to be assigned in the simulation is defined along with the time interval for the time steps. The solution will be calculated within the set period of every time steps. The *Time Dependant Solver* is assigned in the *Transient* analysis and after these settings and values have been assigned, the simulation can begin to start by clicking the solve button.

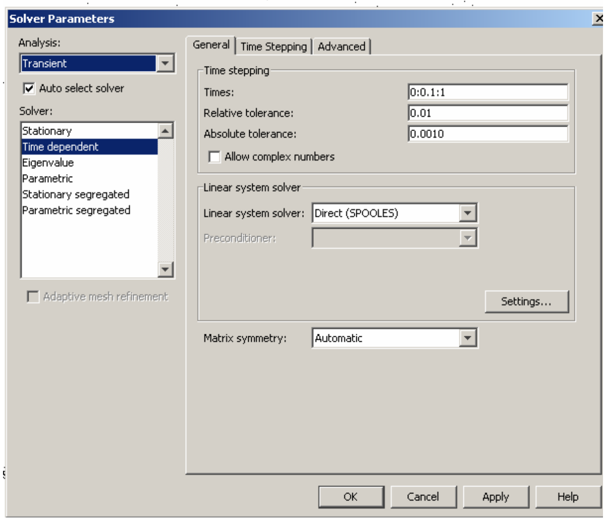

Analysis: Transient

☑ Auto select solver

Solver: Time dependent

Times: 0:0.1:1

Relative tolerance: 0.01

Absolute tolerance: 0.0010

Linear system solver: Direct (SPOOLES)

Matrix symmetry: Automatic

Figure B9: Setting the time steps for the 3D Transient solver

B7. Postprocessing and visualisation

After the simulation has been solved, the software automatically displays a surface plot for the dependant variable, in this case the temperature. Other types of solutions plots e.g. induced current; can be generated using the *Plot Parameters* in the *Postprocessing* menu as shown in Figure B10. Data from the plots can be extracted to form numerical data which can be used for further analysis.

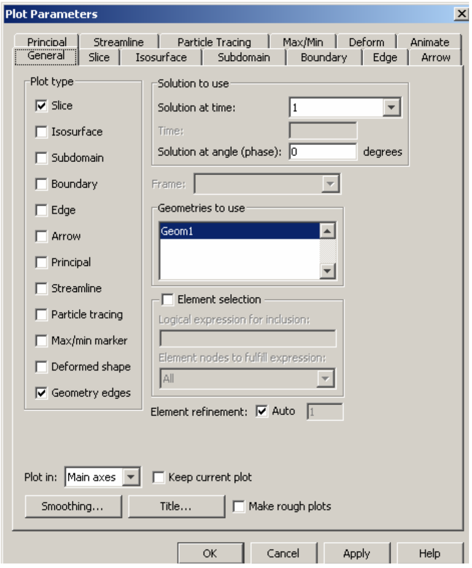

☑ Slice

☑ Geometry edges

Solution at time: 1

Solution at angle (phase): 0 degrees

Geometries to use: Geom1

Element refinement: ☑ Auto

Plot in: Main axes

Figure B10: Generating the solution plots from the Postprocessing menu

Appendix C: Feasibility study of the practicality of PEC thermography for TMS application

TMS simulations on human brain are performed to observe the practicality of the TMS to be mapped using the IR camera. In the simulation performed in COMSOL, the TMS coil is placed over a spherical model of a human brain as shown in Figure C1. This arrangement is to model the brain mapping technique by TMS. Results of the magnetic field and temperature change having different current input are acquired for comparison with different heating duration.

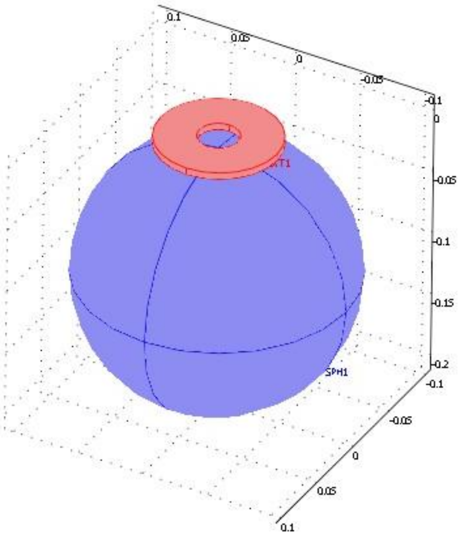

Figure C1: Coil and sphere model in 3D in COMSOL

A circular TMS coil having and outer diameter (OD) of 90mm and inner diameter (ID) of 30mm is used in the simulation with different current input of 50A, 100A, 200A, 500A, 800A and 1000A. These parameters are to match the TMS coil used in the medical field. The lift-off of the coil was set to be 5mm. The applied excitation waveform for the coil are set to be according to the ones used by the Magstim TMS system, where the rising time is set at 100μs with maximum duration of 5ms and 10ms. The initial temperature was set at 19.85 ^{o}C for every case of the simulation. The sphere used in the model has a diameter of 200mm and the electrical and thermal parameters for human brain used in the simulations are shown in Table C1.

Table C1: Electrical and thermal parameters for human brain

Parameters	Human brain
Conductivity, δ $\left[S/m\right]$	0.1
Temperature coefficient $\left[K^{-1}\right]$	0.012
Density, d $\left[kg/m^3\right]$	1041
Heat capacity, C_p $\left[J/kg.K\right]$	3680
Thermal conductivity, k $\left[W/m.k\right]$	0.527
Thermal Diffusivity, α $\left(= k/dC_p\right)$ $\left[m^2/s\right]$	1.3757E-07

The reading for the net magnetic field produce by the coil with the presence of the human brain is taken at the centre of the coil. The temperature change is taken at the sphere surface directly under the coil windings. Figure C2 and C3 show the results for 5ms and 10ms heating duration. The figures show the effect of heating duration towards the measured magnetic field intensity and temperature.

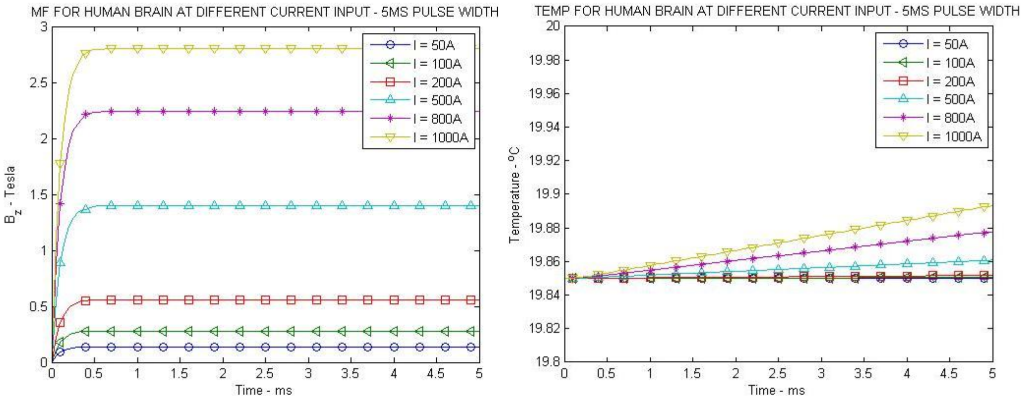

a) b)

Figure C2: a) Net magnetic field for 5ms excitation; and b) Temperature change for 5ms excitation

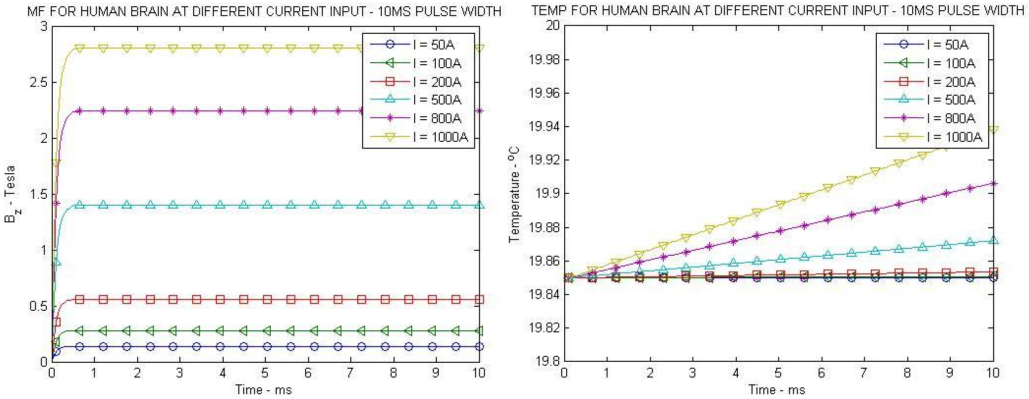

a) b)

Figure C3: a) Net magnetic field for 10ms excitation; and b) Temperature change for 10ms excitation

As it can be seen from Figure C2 and Figure C3, with the increase in heating duration, the maximum net magnetic field strength still remains the same with the associated current input. However, the maximum temperature rise shows an increase with the increase in heating duration. For example, for 5ms and 10ms pulse width and 1000A current input the largest temperature change observed is approximately 0.05°C and 0.10°C respectively. These show that with appropriate heating duration selection, the desired temperature change can be achieved and if it is within the range of the temperature change resolution that can be captured using IR camera, then the temperature change mapping is achievable.